Abundance Variation of Dense Gas Tracers in the Gould Belt

by

Maria Monica Pettyjohn

A thesis submitted in partial fulfillment of the requirements for the degree of

Master of Science

Department of Physics
University of Alberta

Abstract

Molecular abundance ratios have been proposed to trace the chemical and evolutionary state of star forming molecular clouds because the formation and destruction of such molecules is dependent on the local environmental conditions, like the density and radiation field that both evolve with time. In this thesis, we use the Green Bank Ammonia Survey (K-Band) ammonia (NH_3) and rare-carbon chain (C_2S and HC_5N) emission maps to make controlled measurements of how the abundances of key molecular tracers vary across different star forming regions. We extend prior work on molecular abundance ratios by applying it across a range of density and temperature regimes in NGC 1333 and Orion A by spectrally stacking NH_3, C_2S, and HC_5N emission in spatially relevant bins determined by Voronoi tessellation of the underlying H_2 density. The resultant molecular abundances are used to test the NH_3/C_2S abundance ratio that has been previously shown to be enhanced in star forming gas. Using the VISION YSO catalogue, we classify the evolutionary stage of the regions in Orion A and find that NH_3/C_2S abundance ratio is indeed enhanced in the star forming regions of Orion A. In addition to this analysis, we compare molecular abundances to the strength of the radiation fields in NGC 1333 and Orion A and find that C_2S and HC_5N abundances are higher where the radiation field is stronger. We also find that NH_3 abundances increase with decreasing radiation field strength, suggesting that the chemical conditions for NH_3 formation are different than C_2S and HC_5N.

Preface

This thesis is an original work by Maria Monica Pettyjohn in collaboration with Professor Erik Rosolowsky at the University of Alberta. It is based on the Green Bank Ammonia Survey by Friesen et al. (2017) and it substantially based off the work of Suzuki et al. (1992).

The work described in this thesis is in preparation to be submitted to MNRAS with Erik Rosolowsky and the GAS collaboration (Pettyjohn et al., 2021). In Chapter 2, I was responsible for constructing the velocity fields and spatial region for binning the rare-carbon chains and ammonia emission using code developed by Erik Rosolowsky and Cappellari and Copin (2003), respectively. I was also responsible for stacking and fitting the rare-carbon chain emission using the `pyspeckit` code package and code developed by Erik Rosolowsky, and calculating the molecular column densities according to Mangum and Shirley (2015). Erik Rosolowsky was responsible for developing the non-LTE fitting procedure for ammonia emission, described in Pettyjohn et al. (2021). In Chapter 3, I was responsible for performing analysis of the resultant molecular abundances.

The GAS collaboration, including Rachel Friesen, Jaime Pineda, Erik Rosolowsky, Stella Offner, James Di Franceso, Spandan Choudhury, Yancy Shirley, Paola Caselli, Adam Ginsburg, and Mike Chen, in addition to creating the data set underlying this thesis, helped with the direction for the data analysis of Chapter 3.

"There is coffee in that nebula."

- *Captain Kathryn Janeway,* Star Trek: Voyager

Acknowledgements

First and foremost, I would like to thank my supervisor Erik Rosolowsky for his patience, guidance, and understanding during my Master's degree. Without his mentorship, this thesis would not be possible. I would also like to thank fellow group members Soumen Deb and Eric Koch for their constant support and helpful conversations. I am also thankful to my committee members Professor Gregory R. Sivakoff and Professor Craig O. Heinke for their support and advice.

Finally, I would also like to thank the GAS collaboration for helping me understand the data and providing directions for data analysis.

Table of Contents

List of Tables

List of Figures

Abbreviations

BIC Bayesian Information Criterion.

C carbon.

CARMA Combined Array for Research in Millimeter Astronomy.

CNM Cold Neutral Medium.

DEC Declination.

FCRAO Five College Radio Astronomy Observatory.

FFT Fast Fourier Transform.

GAS Green Bank Ammonia Survey.

GBT Green Bank Telescope.

GMC Giant Molecular Cloud.

H hydrogen.

He helium.

ISM Interstellar Medium.

KEYSTONE KFPA Examinations of Young STellar Object Natal Environments.

KFPA K-band Focal Plane Arra.

LSR Local Standard of Rest.

LTE Local Thermodynamic Equilibrium.

MC Molecular Cloud.

MW Milky Way.

N nitrogen.

NRO Nobeyama Radio Observatory.

O oxygen.

PDR Photo-disassociation Region.

R.A. Right Ascension.

RCC Rare Carbon Chain.

ROI Region-of-Interest.

S/N Signal-to-Noise.

SESNA Spitzer Extended Solar Neighborhood Archive.

SNR Signal-to-Noise Ratio.

UV Ultraviolet.

VEGAS VErsatile GBT Astronomical Spectrometer.

VISION Vienna survey in Orion.

WCCC Warm Carbon Chain Chemsitry.

WNM Warm Neutral Medium.

YSO Young Stellar Object.

Chapter 1

Introduction

The first molecule to be discovered in space was the methlidyne radical in 1937 by Swings and Rosenfeld (1937); Dunham (1937); McKellar (1940). Ever since, molecules have proven to be useful tools in examining environmental condition and evolutionary state of interstellar gas. At the moment, relative abundances of different molecular species have been tentatively put forth as diagnostics of molecular cloud time evolution but have not been proven to be broadly applicable as clocks. In this thesis, we will apply the chemical clock hypothesis and compare molecular abundances to gas conditions in low- and high-mass star forming regions in the Gould Belt, which includes all of the major star forming regions to Earth, to shed light on the connection between chemistry, environmental conditions, and evolutionary state using rare-carbon chain (RCC) and ammonia (NH_3) emission from the Green Bank Ammonia Survey described in Section 1.6 (Friesen et al., 2017).

We will begin by briefly explaining the composition of the interstellar medium and the star forming process in Section 1.1. Next, we describe chemical processes specific to the conditions of space, including how rare-carbon chains and ammonia molecules are formed and our current understanding of environmental impacts on chemistry in space Section 1.2. In Sections 1.3 to 1.5, we describe the theoretical and observational methods required to make the molecular line observations from Friesen et al. (2017) used in this thesis. In Chapter 2, we will describe the data processing

methods used to obtain the rare-carbon chain and ammonia molecular abundances. Finally, Chapter 3 discusses the molecular abundances in the context of chemistry, environment, and evolutionary stage as described in Chapter 1.

1.1 Interstellar Medium and Star Formation

Our galaxy, the Milky Way (MW), is composed of stars, gas, and dust. The gas and dust filling the space between the stars is called the interstellar medium (ISM). This thesis focuses on the molecular phase of the ISM that consists of molecular clouds (MCs) named for the enclosing presence and formation of molecules. Star formation occurs in MCs, which are composed of cold ($\sim$ 10 K) and dense ($50 - 10^5$ cm^{-3}) gas and dust (Bergin and Tafalla, 2007; Chevance et al., 2020).

MCs are formed in a multi-step process, starting in the warm neutral medium (WNM) with temperature $T \sim 8000$ K and density $n \sim 1$ cm^{-3} in which a part of the ISM cools and collapses due to thermal and gravitational instabilities. Collisionally excited atoms in the WNM emit radiation that escapes and cools the gas. Gas cooling depends on the square of the density of the gas, while heating of the gas is directly proportional to the density. The difference in density dependence between heating and cooling of the gas leads to a thermal instability. A thermally unstable region proceeds to collapse until it reaches the cold neutral medium (CNM) regime that is 100 times denser and cooler than the WNM. Gravity is important in the second phase of collapse of the CNM. The Jeans length represents the scale on which density perturbations in the cloud are amplified fastest, leading to gravitational instability and further collapse into an MC. Gravitational instabilities are generated by a variety of mechanisms, including cloud-cloud collisions, stellar feedback (supernovae, etc.), and compression due to the passing of a spiral arm that lead to cloud collapse on the scale of the Jeans length. In all stages of collapse, a smaller volume of gas within the parent cloud participates, leading to the hierarchical structure of the ISM (Girichidis et al., 2020; Ballesteros-Paredes et al., 2020).

MCs, like Orion A and Perseus, are objects at the largest size scale that decouple from MW dynamics and become self-gravitating objects. MCs are not uniform across the MW, spanning a range of mass and size scales. MCs, like Perseus in which NGC 1333 is embedded, form low-mass stars in isolated clusters and have average gas temperatures of $\sim 10 - 20$ K. Giant molecular clouds (GMCs), like Orion A, form high-mass stars that heat the local gas to temperatures > 20 K. MCs and GMCs represent the lower and higher ends of the mass and size ranges, ranging from $10^3 - 10^5$ $M_\odot$ and $2 - 15$ pc. MCs and GMCs have average densities of $50 - 500$ cm^{-3} and are embedded in the diffuse WNM at ~ 8000 K. MCs contain $0.3 - 3$ pc clumps of gas and dust, like NGC 1333, which have masses of $50 - 500$ $M_\odot$ and average densities of $10^3 - 10^4$ cm^{-3} that form due to further localized gravitational collapse within the MC. Clumps contain $0.03 - 0.2$ pc cores with masses of $0.5 - 5$ $M_\odot$ and average densities of $10^4 - 10^5$ cm^{-3} that may or may not be star forming, making up a tiny fraction of the total volume of the multi-phase MC (Bergin and Tafalla, 2007; Chevance et al., 2020).

MCs become star forming regions when their pre-stellar cores start to gravitationally collapse and form stars. During collapse, the internal temperature of the core increases and its material becomes optically thick. The newly formed protostar at the centre accretes matter from the surrounding core envelope. The natal envelope dissipates and flattens into an accretion disk as the protostar evolves. The protostar exits the star forming stage to become a pre-main-sequence star when it is hot enough to perform fusion. The remaining accretion disk is the material out of which planets and comets form (Kennicutt and Evans, 2012; Chevance et al., 2020). Each stage of star formation has unique density, temperature, and radiation characteristics that lead to different types of chemistry (Öberg and Bergin, 2021). The local chemistry, dynamics, and mean lifetime for collapse of an MC all influence the composition, number, mass, and distribution of the stars and planets born from its material.

The composition of stars and planets is dependent on the early chemistry of the

originating MC (Öberg and Bergin, 2021). The majority of matter making up MCs is hydrogen (H), with a small amount of helium (He) and heavier elements. The most common heavier elements include, carbon (C), nitrogen (N), and oxygen (O). H_2 molecules make up a large fraction of available H in MCs, which do not emit detectable radiation at the temperatures and densities of cores. As a result, dense star forming gas is traced by other molecules, like carbon monoxide (CO), rare-carbon chains (RCCs), and ammonia (NH_3).

Dense gas goes through several phases of chemical changes during the star formation process. Enhancements or decreases in chemical abundances of reactive molecules, like RCCs, over time serve as chemical clocks for the evolution of star forming clouds. The supply of reactive molecules to terrestrial planets, like our own, is believed to be facilitated by the transport of those species on conglomerations of dust and ice, called comets from the outer asteroid belt during planet formation. Understanding the distribution of reactive species in the outer regions of young stellar objects (YSOs) is important for connecting the natal MC composition to the dynamic supply of reactive C-bearing species to the inner solar system (van Dishoeck and Blake, 1998; Bergin and Tafalla, 2007; Sakai et al., 2008; Öberg and Bergin, 2021).

1.2 Chemistry in the Interstellar Medium

In this section, we will go over chemical processes happening across the different environments in MCs. To begin, the basic chemical formation pathways for H_2, CO, and RCCs in the MCs will be described in Sections 1.2.1 and 1.2.2. Because dust grains serve as reservoirs for reactive molecules, like RCCs, and are built into comets, the build-up ice mantles on dust grains by molecular freeze-out will be described in Section 1.2.3 using the chemical pathways explained in the prior sections. Lastly, our current understanding of MC molecular chemistry over time and space, according to the molecular pathways for formation in Sections 1.2.1 and 1.2.2 and dust grain

surface chemistry in Section 1.2.3, will be described in Section 1.2.4, starting on MC scales and ending at clumps and cores. The concept of the chemical clock for tracing chemical change and star forming evolutionary stage will also be described in Section 1.2.4.

1.2.1 H_2 Formation

Gas-phase formation of H_2 from atomic H occurs via radiative association. Because H atoms do not have an electric dipole, two H atoms will only bond together directly very rarely. The main gas-phase pathway for forming molecular H is via the radiative association of a neutral H atom and an electron,

$$\mathrm{H} + \mathrm{e}^- \longrightarrow \mathrm{H}^- + h\nu,$$

in which a photon with energy $h\nu$ is emitted, where h is the Planck's constant and ν is the photon's frequency. The negative H ion then undergoes exothermic associative detachment with ambient H atoms,

$$\mathrm{H}^- + \mathrm{H} \longrightarrow \mathrm{H}_2 + \mathrm{e}^- + \mathrm{KE},$$

to produce molecular H. However, the rate of H_2 production by radiative association is rendered less effective due to the destruction of H^- by interstellar photons. In the dense ISM, making up MCs, dust catalysis is the primary formation pathway for H_2 gas (Draine, 2011; Girichidis et al., 2020).

When an H atom encounters a dust grain, it performs a random walks along the crystalline surface. Dust grain surface chemistry will be further described in Section 1.2.3. Eventually the H atom becomes trapped in a location on the surface where the local thermal fluctuations of the grain cannot input enough energy to free the thermalized atom. As the surface of a dust grain becomes saturated with newly arriving H atoms, the atoms either start to encounter other bound H atoms or diffuse into other binding sites by quantum tunnelling or thermal hopping. When

two H atoms are present in one binding site, they react to form H_2. The reaction is exothermic, producing enough energy to de-absorb the molecule from the grain surface. The formation rate of H_2 in the dense ISM is given by

$$R_{H_2} \sim 3 \times 10^{-17} n\, n_H \text{ s}^{-1} \text{ cm}^{-3}, \tag{1.1}$$

where n is the total number density of gas-phase particles and n_H is the number density of gas-phase atomic H, both expressed in units of particles per cm^{-3} (Wakelam et al., 2017; Girichidis et al., 2020).

1.2.2 Molecule Formation Pathways

Beyond the ubiquitous H_2 molecule, CO, NH_3, and HC_5N are also formed in the ISM by reactions with other molecules. These molecules and molecules like them are the major carriers for the reactive species O, C, and N in MCs. The reactions forming molecules containing reactive species follow a balance of production and destruction that depends on the density, temperature, and local radiation field. A majority of O, C, and N is locked in H_2O, CO, and N_2, which is present in the gas-phase and on ices (Oberg). The reservoirs for O, C, N, and other volatile species, like sulfur (S), are established as MCs form and evolve. Ammonia and RCCs are the building blocks towards more complex chemistry in the ISM. In this section, we present the dominant reaction pathways for CO, RCC, and NH_3 formation. The astrophysical conditions that lead to CO, RCC, and NH_3 formation and the implications of this chemistry will be described in Sections 1.2.3 and 1.2.4.

In the diffuse edges of MCs with $n_H = 100$ cm^{-3} and $T_K = 100$ K, a majority of C is in the form of C^+ and undergoes complicated hydrogen-carbon chemistry to form CO (Kwok, 2007). First, OH if formed in a series of reactions starting with O^+ and involving H_2 in the first three steps. The following reactions with resultant OH and

ambient C^+ generate CO with the greatest efficiency in diffuse gas

$$C^+ + OH \longrightarrow CO^+ + H,$$
$$CO^+ + H_2 \longrightarrow HCO^+ + H,$$
$$HCO^+ + e^- \longrightarrow CO + H,$$

which are all assumed to take place in the gas-phase. The reaction pathway describes the evolution of C in the form of C^+ to CO as interstellar matter contracts and becomes dense and more opaque to UV radiation. As the gas approaches densities of $n_H = 1000$ cm^{-3}, disassociation by UV photons becomes negligible and the chemical pathways above are replaced with a set starting with $H_3{}^+$. Eventually, a majority of C is locked up in CO in MCs because it has only a few slow chemical destruction processes (Kwok, 2007).

Similarly, the interstellar synthesis pathway for NH_3 involves reactions with H_2, as follows

$$N^+ + H_2 \longrightarrow NH^+ + H,$$
$$NH^+ + H_2 \longrightarrow NH_2{}^+ + H,$$
$$NH_2{}^+ + H_2 \longrightarrow NH_3{}^+ + H,$$
$$NH_3{}^+ + H_2 \longrightarrow NH_4{}^+ + H,$$
$$NH_4{}^+ + e^- \longrightarrow NH_3 + H,$$

where N^+ is formed in dissociative ionization of N_2 with He^+ at 10 K (Scott et al., 1997; Rednyk et al., 2019). On the surface of dust grains, NH_3 is formed in the ion-neutral reaction pathway

$$N^+ + H \longrightarrow NH^+,$$
$$NH^+ + H \longrightarrow NH_2{}^+,$$
$$NH_2{}^+ + H \longrightarrow NH_3.$$

The sulfur (S) containing RCC C_2S is formed in a more complicated pathway in the gas-phase, as follows

$$S^+ + C_2H \longrightarrow C_2S^+ + H,$$
$$C_2S^+ + H_2 \longrightarrow HC_2S^+ + H,$$
$$HC_2S^+ + e^- \longrightarrow C_2S + H$$

in which H_2 is again a vital participant in the reaction. On grain surfaces, C_2S is formed in the neutral-neutral reaction (Laas and Caselli, 2019)

$$CH + CS \longrightarrow H + C_2S.$$

The N containing RCC HC_5N undergo different chemistry, in which H_2 is not important. Three main schemes for HC_5N formation exist. First, a reaction between the radical CN and a hydrocarbon:

$$C_4H_2 + CN \longrightarrow HC_5N + H.$$

Second, a reaction between a hydrocarbon and the second smallest RCC:

$$C_2H + HC_3N \longrightarrow HC_5N + H.$$

Third, a reaction between a hydrocarbon and N atom:

$$C_5H_3{}^+ + N \longrightarrow H_2C_5N^+ + H,$$
$$H_2C_5N^+ + e^- \longrightarrow HC_5N + H.$$

In gas with $T > 25$ K, the first reaction is the main production mechanism for HC_5N (Taniguchi et al., 2016; Burkhardt et al., 2018; Taniguchi et al., 2019). In the cold, dense parts of MCs Burkhardt et al. (2018) found that the most efficient formation pathway is the third reaction between hydrocarbons and N atoms. To generate the hydrocarbons present in the reactions of HC_5N, C is first photo disassociated out of CO with secondary UV photons from the excitement of H_2 (Tielens, 2005).

1.2.3 Dust Grain Freeze-Out and Ice Mantles

Compared to solar abundances, the interstellar abundances of C, O, and N are $20-30\%$ lower in the interstellar medium. The difference in observed abundances is attributed to the depletion of atomic species into gas-phase molecules, like RCCs, solids, and onto the surfaces of dust grains (van Dishoeck and Blake, 1998). The chemistry at the surface of a dense MC is dependent on photo dissociation, gas-phase, and dust-surface chemical processes. The interior of cores and clumps are shielded from photons and evolve according to an exchange between gas-phase production of molecules and their subsequent freeze-out onto grain surfaces. Because the depletion and sublimation of molecular species on dust grain surfaces is dependent on the local environment, the process of dust grain freeze-out in the production of ice mantles is important for describing the relative abundances of volatile molecular species (van Dishoeck and Blake, 1998; Öberg and Bergin, 2021).

Dust grains are rare in MCs in comparison to gas-phase species, but are important in many chemical processes and the formation of new, more complex molecules, as discussed previously. Dust grains are cold carbonaceous crystalline structures of atoms that are present in the cold cores and clumps of MCs. Atoms and molecules that collide with a dust grain will be absorbed onto its surface, like H atoms in the formation of H_2 that dominates the early-stages of ice mantle build-up.

The build-up of ice mantles on dust grains is sequential, with water-ice being the first to form when heavier O atoms react with trapped H atoms. Because water-ice is formed early and readily in the life cycle of an MC, it is found across the cloud (van Dishoeck and Blake, 1998). Once CO becomes the dominant form of gas-phase C and begins to freeze-out on grain surfaces, it reacts to forms CO_2 ices on the dust grain surface. The process of CO dust grain freeze-out leads to the depletion of reactive C and O volatiles in the gas-phase and allows for nitrogen-based chemistry to take place. Because hydrocarbons are mainly built by C^+ insertion, the depletion of atomic C

also leads to the halt of more complex hydrocarbon formation. With hydrocarbons taking an essential role in RCC formation, CO formation is anti-correlated with HC_5N and C_2S formation.

In atomic-C depleted gas in MCs, NH_3 is formed in the gas-phase and on dust grain surfaces. On dust grain surfaces, mobile H atoms react like atomic N^+ in a series of interactions to form NH_3. As the gas further contracts and cools, the atomic N reservoir is depleted in the formation of N_2 gas in a series of slow gas-phase neutral-neutral reactions. As a result, ice mantles on dust grains are the main reservoirs for volatile molecular species in pre-stellar clumps and cores.

Molecules are deabsorbed by thermal evaporation at high temperatures as a star is born, or cosmic-ray heating and explosive heating due to exothermic reactions on the grain-surface in cold gas. The likelihood of a molecule being released by one of these processes is dependent on its polarity. Highly polar H_2O is hard to remove in cold gas, while H_2 is readily released with the input of kinetic energy during formation (van Dishoeck and Blake, 1998). H_2O sublimated from ice mantles at ~ 90 K and CO_2 is sublimated at ~ 45 K, leading to a separation between H_2O and CO_2 ices at higher temperatures. At the edge of MCs and in locations of active star formation, cosmic-ray heating leads to new formation pathways of volatile species like OH that can subsequently react to form CO_2 (van Dishoeck and Blake, 1998; Boogert et al., 2015; Öberg and Bergin, 2021). Before star formation starts, gas-phase processing, dust grain freeze-out and energetic processing of H, C, N, O, and S atoms is responsible for the generation of the initial chemical supply for star and planet formation.

1.2.4 Spatial and Temporal Molecular Abundance Evolution

Because of the sequential nature of ice mantle build up on dust grain surfaces and their subsequent energetic processing due to thermal heating and cosmic-ray bombardment, dust grain ice mantle and gas molecular abundances have spatial and temporal dependence on the local environment of the parent MC. RCCs make up a

small fraction of the chemical species at the beginning of star formation, but have importance in the later formation of life-bearing molecules like DNA and proteins. The following section describes the dominant chemical processes and resulting general relative chemical abundances of H-, O-, C-, and N-bearing species at different positions and times inside MCs.

Molecular Cloud Chemical Differentiation

The outer, less dense edges of an MC are affected by ionizing UV radiation. Photons with energies higher than 13.6 eV ionize neutral H, leading to a combined ionized/neutral medium. The ionization ratio is exaggerated if the exterior of the cloud is exposed to massive star with high levels of UV radiation in regions called photo disassociation regions (PDRs Öberg and Bergin, 2021). Moving inside the cloud, dust grains begin to shield the cloud from the UV radiation and allow neutral-neutral grain-surface reactions to out pace the ionization of atomic H. As H_2 is formed, it additionally self-shields against ionizing UV radiation. Coinciding with atomic and molecular H is atomic C, N, and O gas (Ehrenfreund and Charnley, 2000; Öberg and Bergin, 2021).

C^+ gas slowly transitions to neutral C when shielded from the UV absorption by dust and H_2. Gas-phase reactions with C lead to the production of the hydrocarbon C_2H, which is important in the formation of C_2S and abundant in the outer regions of the cloud. C_2H is also readily destroyed by UV radiation and serves as a boundary between neutral and ionized regions in MCs. Competing with the slow reaction transition of C^+ to neutral C is the complicated set of reactions involving C^+ and O^+ ions to form CO. With increasing density and depth into the cloud, progressively more C is locked up in CO and must be freed to participate in further reactions (Tielens, 2005; Kwok, 2007; Öberg and Bergin, 2021). The formation of CO in the gas-phase across a range of densities reiterates its usefulness in tracing a variety of cloud densities.

In the same layer of gas in which C^+ is efficiently converted into CO, H_2O is being formed on the surface of dust grains. The parallel formation of H_2O and CO leads

to the depletion of atomic O in the outer regions of the cloud that is divided roughly equally between both species in ice-phase and gas-phase, respectively. Grain-surface chemistry and subsequent build up of ices is attenuated by photo disassociation with decreasing cloud depth, linking the ratio of C^+/CO to the mantle thickness of ices on grain-surfaces (Öberg and Bergin, 2021).

RCCs are abundant in the early stages of star formation before C is locked up in CO. The efficient production of RCCs before C depletion is offset by their destruction by reactions with H^+, He^+, and O. RCCs are also depleted on ice-grain surfaces, contributing to the build up of unsaturated reactive species in ice mantles. The attenuation of RCC formation by C depletion, destruction, and freeze-out occurs at a faster pace than the dynamical timescale of molecular clouds, leading to gas-phase RCC abundance peaks in the early stages of star formation (Sakai et al., 2008; Öberg and Bergin, 2021). The subsequent grain-surface freeze-out of NH_3 and RCCs leads to a reservoir of reactive species in ice mantles in cores and clumps, as will be described next (Sakai et al., 2008; Öberg and Bergin, 2021).

Clump and Core Chemical Differentiation

In the absence of C and O in dense clumps and cores, nitrogen-based chemistry becomes more important in the conversion of atomic N into N_2 and species like NH_3. As a result, nitrogen-bearing species become more abundant in the later stages of MC evolution. The N supply is depleted by the slow formation of N_2 in neutral-neutral reactions. N_2, like H_2, does not emit detectable radiation in the dense, cold regions in which it is formed, so only a small portion of the N reservoir in MCs is observed in the form of NH_3.

Eventually, N-bearing species freeze-out onto dust grain ice mantles, forming a portion of the top layer. Because ice mantles are formed in the pre-stellar environments of MCs and their cores, they serve as the main reservoir for reactive molecular species that go on to form more complex organic molecules. The likelihood of survival for the C-, O-, and N-bearing species through core-collapse and star formation increases

with freeze-out onto ice mantles (Öberg and Bergin, 2021). Therefore, pre-stellar MC, clump, and core chemical evolution provides the ingredients for star and planet formation in the form of chemical reservoirs in dust grain ice mantles.

Ammonia and Rare Carbon Chains as Chemical Clocks

The spatial and temporal diversity of NH_3 and RCCs in MCs have led to the proposal of using the relative molecular abundances as indicators of evolutionary stage, called chemical clocks. Suzuki et al. (1992) represents the first systematic survey of RCCs in a variety of MCs, including the low-mass star forming cores in the Taurus Molecular Cloud and the high-mass Orion KL star forming region. Using the dense gas tracers, C_2S, HC_5N, and NH_3, Suzuki et al. (1992) found that RCC molecular abundances are spatially correlated, but not with NH_3. C_2S emission toward pre-stellar cores was found to be intense, but absent in the high-mass star forming regions, like the Orion KL. HC_5N emission was detected in all observed cores. Overall, the relative abundances of RCCs to NH_3 are thought to be indicators of chemical evolution, with RCCs appearing in higher abundance at the early stages of core collapse and NH_3 at later stages, according to the chemical reasoning above (Suzuki et al., 1992; Hirahara et al., 1992; Rathborne et al., 2008). Suzuki et al. (1992) compared their results with a chemical model and found that the NH_3/C_2S ratio is correlated with time due to C_2S freeze-out. Regions with $NH_3/C_2S < 10$ are tentatively considered to be carbon chain producing regions (Hirota et al., 2009). While some observations of cores have shown the evolutionary correlation brought forward by Suzuki et al. (1992), some studies have found large scatter in the relationship (Foster et al., 2009; Ohashi et al., 2014). The local physical conditions of the MCs and cores have been suggested to lead to non-evolutionary variations in the NH_3/C_2S ratio, including the presence of a UV field (Foster et al., 2009), temperature variations (Marka et al., 2012), H_2 density (Suzuki et al., 1992; Hirota et al., 2009; Suzuki et al., 2014), initial gas-phase C/O ratio (Seo et al., 2019), magnetic field, and turbulence (Hirota et al., 2009).

The ratio of RCCs C_2S/HC_3N has also been suggested as a chemical clock by

Suzuki et al. (2014) who found that average density variations between cores can lead to differences in chemistry. Bright RCC emission, including HC_5N, has been detected towards protostars and massive YSOs (Sakai and Yamamoto, 2013; Spezzano et al., 2016; Taniguchi et al., 2019), leading to the development of Warm Carbon Chain Chemistry (WCCC). WCCC leads to the regeneration of RCCs in the warm and dense gas around protostars. RCCs HC_5N and C_2S have different spatial correlations around protostars, with C_2S being more abundant toward cores than WCCC sources Sakai and Yamamoto (2013). WCCC sources are star forming cores with favourable conditions for the formation of RCCs around their central protostars.

The conditions leading to the differences in HC_5N and C_2S abundance around protostars versus cold and dense cores has been modelled by Taniguchi et al. (2019). Taniguchi et al. (2019) found that HC_5N abundances peak after their sublimation from the surface of dust grains, while C_2S abundances peak after CH_4 is evaporated into the gas-phase, implying C_2S formation may be triggered by the presence of CH_4 in the gas-phase. However, C_2S is extremely reactive and is quickly destroyed by H_2 and O, leading to the bright HC_5N emission over that of C_2S. Kalvāns (2021) has also suggested that WCCC abundances are enhanced by the presence of the interstellar radiation field in addition to the heating of the gas by the central protostar. Kalvāns (2021) suggested that the WCCC phenomenon contains two peaks in abundance, one at the beginning of star formation and the second during CH_4 evaporation. The peak at the beginning of star formation occurs due to ionization and break-up of gas-phase species like CO. Because WCCC is a gas-phase phenomena, the effect is pronounced in low density gas in which freeze-out is slower and ionization radiation more easily penetrates the cloud.

Like RCCs, the chemistry of NH_3 is also more complicated in reality. Traditionally, NH_3 is treated as a late-stage molecule that forms in the absence of free C and O atoms. von Procházka and Millar (2021) modelled the gas-grain cycling and synthesis of NH_3 and found that early formation of CN can lead to the formation of gas-phase

NH_3. von Procházka and Millar (2021) also found that the impact of dust grain surface production on gas-phase abundances of NH_3 is dependent on cosmic-ray heating. The presence of NH_3 in the gas-phase at early and late times of star formation implies that ratios like NH_3/C_2S may be subject to variation due to RCC and NH_3 chemical complexity.

Overall, the diversity of RCC and NH_3 chemistry in star forming regions leads to more complicated correlations between chemical abundance ratios and evolutionary age in molecular gas. However, the application of chemical clock ratios may be helpful in identifying general evolutionary stages and environmental and chemical influences on the abundances of molecular species. In order to make chemical clock measurements, molecular abundances must be calculated from molecular line observations with radio telescopes, as described in Sections 1.3 to 1.5.

1.3 Principles of Molecular Spectroscopy

Astronomy studies far away objects that cannot be experimented on in a laboratory. Radiation that is emitted and absorbed by the molecules making up these objects is crucial for their study. When radiation emitted from a molecule it transitions from an upper energy state E_u to a lower energy state E_l. Following conservation of energy, the molecule emits a photon with energy $h\nu$, as follows

$$h\nu = E_u - E_l. \tag{1.2}$$

In a spectrum, this transition shows up as a sharply defined peak at frequency ν. Atoms make transitions according to the configuration of their electrons, while molecules have more degrees of freedom defined by the geometrical arrangement of their constituent atoms. The nuclei of molecules are able to vibrate around their equilibrium points and rotate around their centres of mass, contributing to the complexity of the spectra. The molecules studied in this thesis (NH_3, C_2S, HC_5N) undergo purely rotational transitions. NH_3 has a pyramidal shape and undergoes a special

tunnelling transition of the N atom through the plane of its three H atoms within each rotational state. On top of the tunnelling transition, NH_3 undergoes hyperfine transitions arising from the interaction of the nuclei and electron spins. The shape, location, and structure of rotational transitions provide a wealth of information on the temperature, kinematic motion, and density of the emitting gas. In the following section, I will describe the quantum mechanical theory underpinning rotational and hyperfine transitions and how intrinsic and environmental conditions influence spectral line shape (Demtröder, 2005; Kwok, 2007).

1.3.1 The Molecular Hamiltonian

The state of a molecule with energy E is described by the Shrödinger equation

$$\hat{H}\Psi = E\Psi, \tag{1.3}$$

which is an energy conservation equation. Hamiltonian $\hat{H}$ includes the kinetic $\hat{T}$ and potential energy $\hat{V}$ contributions, so that

$$\hat{H} = \hat{T} + \hat{V}. \tag{1.4}$$

The potential energy includes three terms,

$$\hat{V} = \hat{V}_{\mathrm{nuc,nuc}} + \hat{V}_{\mathrm{nuc,el}} + \hat{V}_{\mathrm{el,el}}, \tag{1.5}$$

including the Coulomb mutual repulsion between the nuclei, attraction between the nuclei and the electrons, and the mutual repulsion between the electrons, respectively. Similarly, the kinetic term can be broken into two terms, one for the motion of the electrons and one for the motion of the nuclei,

$$\hat{T} = \hat{T}_{\mathrm{el}} + \hat{T}_{\mathrm{nuc}}, \tag{1.6}$$

which depends on the relative velocities of the nuclei and electrons. For real molecules with more than a few components, the Hamiltonian because very complicated and impossible to compute accurately. As a result, physically motivated approximations are

applied to the Hamiltonian to simplify the computation. The principal simplification is the Born-Oppenheimer approximation that assumes that the nuclear velocities are much slower than the electronic motions. Therefore, the Hamiltonian of the electronic and nuclear parts can be separated. The electronic contribution to the Hamiltonian, in which the nuclei are unmoving, takes the form

$$\hat{H}_{\text{el}} = \hat{T}_{\text{el}} + V_{\text{nuc,nuc}} + \hat{V}_{\text{el,nuc}} + \hat{V}_{\text{el,el}}. \tag{1.7}$$

The nuclear part of the Hamiltonian $\hat{H}_{\text{nuc}}$ is solved for separately and breaks down into the vibrational $\hat{T}_{\text{vib}}$ and rotational $\hat{T}_{\text{nuc}}$ kinetic motions of the nuclei,

$$\hat{H}_{\text{nuc}} = \hat{T}_{\text{nuc}} + V_{\text{nuc}}, \tag{1.8}$$

$$= \hat{T}_{\text{vib}} + \hat{T}_{\text{rot}} + E_{\text{el}}, \tag{1.9}$$

where potential energy V_{nuc} is equal to the total potential and electronic kinetic energy of rigidly bound molecule, E_{el}. As a result, E_{el} is averaged over the electron motions and serves as the potential under which the nuclei move.

The molecules studied in this thesis undergo purely rotational transitions in a certain electronic and vibrational state, called rotational spectroscopy. The rotational Hamiltonian $\hat{T}_{\text{rot}}$ is described by rigid body rotation. The angular momentum L of a rigid body takes into account the geometrical distribution of mass of the molecule. If we fix the coordinate system to the body of the molecule, the angular momenta in each dimension are broken into three parts $L_x = I_x\omega_x$, $L_y = I_y\omega_y$, and $L_z = I_z\omega_z$, where ω is angular velocity and I is the moment of inertia. The energy of a rotational state in a molecule is given by

$$E_r = \frac{L_x^2}{2I_x} + \frac{L_y^2}{2I_y} + \frac{L_z^2}{2I_z}. \tag{1.10}$$

The geometrical axes are fixed to the molecule and then assigned an alphabetical label according to their size. Linear molecules like C_2S, HC_5N, and HC_7N are linear molecules for which $I_b = I_c$ and $I_a = 0$, implying that all of the mass is along the axis

labelled a and contributes no angular momentum. As such, the energy equation for linear molecules reduces to

$$E_r^{\text{linear}} = \frac{J^2}{2I_b}, \tag{1.11}$$

where $J^2 = L_a^2 + L_b^2 + L_c^2$ according to Pythagoras theorem and J represents the total rotational angular momentum of the molecule.

Oblate symmetric top molecules, like NH_3, have circular symmetry in the plane of the two axes, yielding moments of inertia $I_a = I_b < I_c$ for which the a and b axes are in the plane of the 3 H atoms. The molecule is oblate because the moment of inertia appears as the reciprocal in the energy equation (Bernath, 2016). For oblate symmetric tops, the energy equation remains complicated as

$$E_r^{\text{oblate}} = \frac{L_a^2 + L_b^2}{2I_b} + \frac{L_c^2}{2I_c}. \tag{1.12}$$

Translating into the language of quantum mechanics, the rotational Hamiltonians for the linear and oblate symmetric tops are

$$\hat{H}_{\text{rot}}^{\text{linear}} = \frac{\hat{J}^2}{2I_b}, \tag{1.13}$$

and

$$\hat{H}_{\text{rot}}^{\text{oblate}} = \frac{\hat{J}_a^2 + \hat{J}_b^2}{2I_b} + \frac{\hat{J}_c^2}{2I_c}. \tag{1.14}$$

It is standard to set the equal moments of inertia to the label "b". The operator $\hat{J}^2 = \hat{J}_a^2 + \hat{J}_b^2 + \hat{J}_c^2$ operator has eigenvalues $\hbar^2 J(J+1)$, leading to the definition of the rotational constant B,

$$B = \frac{\hbar^2}{2I_b}, \tag{1.15}$$

so

$$E_{\text{nuc}}^{\text{linear}} = BJ(J+1). \tag{1.16}$$

For the case of the oblate symmetric top, we have

$$\hat{H}_{\text{rot}}^{\text{oblate}}\Psi_{\text{nuc}} = \frac{\hat{J}_a^2 + \hat{J}_b^2}{2I_b}\Psi_{\text{nuc}} + \frac{\hat{J}_c^2}{2I_c}\Psi_{\text{nuc}}. \tag{1.17}$$

To derive the $\hat{J}^2$ operator, add and subtract a $\frac{\hat{J}_c^2}{2I_b}\Psi_{\text{nuc}}$ term to the right-hand side of the equation

$$\hat{H}_{\text{rot}}^{\text{oblate}}\Psi_{\text{nuc}} = \frac{\hat{J}_a^2 + \hat{J}_b^2}{2I_b}\Psi_{\text{nuc}} + \frac{\hat{J}_c^2}{2I_c}\Psi_{\text{nuc}} + \frac{\hat{J}_c^2}{2I_b}\Psi_{\text{nuc}} - \frac{\hat{J}_c^2}{2I_b}\Psi_{\text{nuc}}, \tag{1.18}$$

$$= \frac{\hat{J}_a^2 + \hat{J}_b^2 + \hat{J}_c{}^2}{2I_b}\Psi_{\text{nuc}} + \left(\frac{\hat{J}_c^2}{2I_c} - \frac{\hat{J}_c^2}{2I_b}\right)\Psi_{\text{nuc}}, \tag{1.19}$$

$$= \frac{\hat{J}^2}{2I_b}\Psi_{\text{nuc}} + \left(\frac{1}{2I_c} - \frac{1}{2I_b}\right)\hat{J}_c^2\Psi_{\text{nuc}}, \tag{1.20}$$

where

$$C = \frac{h^2}{2I_C}, \tag{1.21}$$

similar to **??**. The $\hat{J}_c^2$ operator has eigenvalues k^2 so

$$E_{\text{nuc}}^{\text{oblate}} = BJ(J+1) + (C-B)k^2. \tag{1.22}$$

J is the total angular momentum quantum number and k quantum number representing the projection of J onto the fixed c-axis.

1.3.2 Degeneracy

Degeneracy implies that there are multiple ways in which a molecule can rotate and gain the same amount of rotational angular momentum because of the relationship between the J and k quantum numbers and how they show up in the energy equations. All molecules follow the degeneracy rule,

$$g_J = 2J + 1, \tag{1.23}$$

in which there are $2J+1$ projections of the total angular momentum onto the fixed axis c. The degeneracy g_J thus corresponds to the number of possible values of the quantum number $k = -J, -J+1, ..., J$.

For symmetric top molecules, the square of the k quantum number arises in the energy equation and contributes a degeneracy g_k of

$$g_k = 2, \tag{1.24}$$

when $k \neq 0$ because $\sqrt{k^2} = +k, -k$. The degeneracy in the k quantum number is $g_k = 1$ in linear molecules because there is no angular momentum contribution along the axis of the molecule and so k does not show up in the energy equation. When $g_k = 1$, there is no additional degeneracy added to the energy level structure of the molecule (Demtröder, 2005; Mangum and Shirley, 2015; Bernath, 2016).

Nuclear degeneracy due to changes in geometry occur through the inversion of the molecular axes. Linear molecules do not have inversion degeneracy because the inversion can be achieved through rotation. If the potential barrier for inversion is overcome in non-linear molecules, a second configuration of the molecule can be achieved. In NH_3, the N atom tunnels through the plane of the 3 H atoms. Because the two configurations have the same rotational energy, all rotational levels in the molecule split in a process called inversion-doubling. Inversion-doubling occurs in $J = k$ rotational states in which electric-dipole transitions are otherwise forbidden because the molecule is spinning about its symmetry axis through the N atom. The inversion degeneracy is given by

$$g_{\text{inv}} = 2. \tag{1.25}$$

The spin of individual nuclei in an atom also contributes to the nuclear degeneracy of a molecule. Each nucleus of an atom has a spin I. Atoms in this thesis have spins $I_{\text{H}} = \frac{1}{2}$, $I_{\text{C}} = 0$, $I_{\text{N}} = 1$, and $I_{\text{S}} = 0$. Like electrons, the spin of nucleus is determined by symmetrically adding together spins of individual protons and neutrons making up the nucleus that each have spins of $\frac{1}{2}$. Like rotational degeneracy g_J, identical nuclei have $2I_i + 1$ possible configurations in a nucleus leading to

$$g_n = \prod_i (2I_i + 1). \tag{1.26}$$

For example, the linear molecule HC_5N has nuclear degeneracy

$$g_n = (2 \times 0 + 1)^5 = 1, \tag{1.27}$$

for each identical nucleus i. In general, all molecules that have no centre of symmetry have $g_n = 1$ because composing atoms cannot be inverted such that the molecule has the same structure. The non-linear molecule NH_3 has nuclear degeneracy

$$g_n = \left(2 \times \frac{1}{2} + 1\right)^3 = 8, \tag{1.28}$$

so there are 8 possible configurations for the 3 H atoms. However, not all corresponding nuclear wavefunctions can exist together with the rotational wavefunctions of a molecule and so the nuclear spin is reduced. The reduced number of nuclear degeneracy states, called the nuclear spin statistical weight, is given by

$$g_I = \frac{g_{\text{nuclear}}}{g_n}, \tag{1.29}$$

where g_{nuclear} represents the total number of nuclear spin wavefunctions available under symmetry considerations. As previously stated, the consideration made for linear molecules with no centre of symmetry translates to the calculation of the nuclear spin statistical weight so that $g_I = 1$. With the symmetry of the rotational wavefunctions, g_{nuclear} takes the form of

$$g_{\text{nuclear}} = \frac{1}{3}(2I_{\text{H}} + 1)(4I_{\text{H}}^2 + 4I_{\text{H}} + 3) = 4 \quad \text{for} \quad k = 3n, \tag{1.30}$$

$$= \frac{1}{3}(2I_{\text{H}} + 1)(4I_{\text{H}}^2 + 4I_{\text{H}}) = 2 \quad \text{for} \quad k \neq 3n, \tag{1.31}$$

where the first equation applies when k is a multiple of 3 and the second equation applies when k is not a multiple of 3 (Mangum and Shirley, 2015). Together, the nuclear spin statistical weights of NH_3 transitions are given by

$$g_I = \frac{4}{8} \quad \text{for} \quad k = 3n, \tag{1.32}$$

$$g_I = \frac{2}{8} \quad \text{for} \quad k \neq 3n. \tag{1.33}$$

The total degeneracy of an energy level is given by

$$g_{\text{tot}} = g_J g_k g_I g_{\text{inv}}. \tag{1.34}$$

Hyperfine Structure in NH_3

Molecules with multiple identical nuclei have spectra that are dependent on nuclear spin. The two states of NH_3 correspond to the two nuclear spin statistical weights in Equations (1.32) and (1.33), where the larger statistical weight is called the ortho state (all H spins are parallel) and the other is called the para state (H spins are anti-parallel) (Ho and Townes, 1983). Effectively, the molecules are split into two species depending on the overall wavefunction symmetry with the rotational symmetry being set by k. In this thesis, I focus on NH_3 transitions between inversion-doubled $J = k = 1, 2$ energy levels that correspond to the para species with nuclear spin statistical weight Equation (1.33) and energy difference $\sim$ 23.694 GHz (Kwok, 2007; Draine, 2011).

The interaction between the electric-quadropole moment of the N nucleus and the electric field generated by the electrons results in splitting of the each energy level into hyperfine energy levels. Furthermore, the weak interaction between the magnetic dipole moment of the 3 H atoms and the magnetic field generated by the electrons results additional magnetic hyperfine lines. For example, the inversion-doubling of the $J = k = 1$ energy levels lead to an overall spectral line emerging with an energy of $\sim$ 23.694 GHz. The hyperfine splitting of the inversion-doubled lines leads to 6 total energy levels and 5 resolvable spectral lines separated by $\sim$ 1 MHz. Each hyperfine energy level is further split to achieve 10 total energy levels and 18 possible spectral lines separated by $\sim$ 40 kHz. Similarly, $J = k = 2$ inversion-doubled lines split into 12 total energy levels and 24 total spectral lines (Kwok, 2007; Wang et al., 2020). When observing $J = k = 1, 2$ NH_3 transitions, not all magnetic hyperfine transitions are resolvable. Often, the 6 hyperfine splittings are observed as 5 spectral lines due to two of the spectral lines having similar frequencies (Wang et al., 2020).

1.4 Radiation and Matter Interaction

1.4.1 Collisional Excitation

Collisional excitation with H_2 is the principal way for molecules in the dense ISM at 10-100 K to become excited so that they can radiate and be detected. The properties of the radiating gas, like the temperature, density, and radiation field, can be inferred through the radiative emission from collisional excitation (Kwok, 2007; Draine, 2011). The relative energy level population is determined by the energy level transition rates. The transition rates depend on contributions from excitation and de-excitation, including spontaneous radiative excitation in the Einstein coefficient A_{ij} (s^{-1}), stimulated radiative excitation and de-excitation induced by the radiation background B (m^3 J^{-1} s^{-2}), and collisional excitation and de-excitation C (s^{-1}), where i and j represent two different energy levels (Rybicki and Lightman, 2004; Draine, 2011). For a two level system in statistical equilibrium, the optically thin limit, and undergoing collisional excitation and radiative de-excitation, the energy levels are populated according to

$$n_1 n_{H_2} C_{12} = n_2 A_{21} + n_2 n_{H_2} C_{21}, \tag{1.35}$$

because the primary route for molecular excitation are collisions with H_2 in the ISM. The relative population between the upper and lower level is given by

$$\frac{n_2}{n_1} = \frac{n_{H_2} C_{12}}{A_{21}} \frac{1}{1 + \frac{n_{H_2} C_{21}}{A_{21}}}, \tag{1.36}$$

The two collisional coefficients are related by

$$C_{12} = \frac{g_2}{g_1} C_{21} e^{-\frac{E_{21}}{kT}}, \tag{1.37}$$

where g are the corresponding degeneracies of each energy level, E_{21} is the energy difference between the two energy levels, and T is the temperature of the emitting gas (Tielens, 2005; Kwok, 2007; Draine, 2011). Using Equation (1.36) to replace C_{12}

yields

$$\frac{n_2}{n_1} = \frac{\frac{g_2}{g_1} e^{-\frac{E_{21}}{kT}}}{1 + \frac{A_{21}}{n_{\mathrm{H_2}} C_{21}}}, \tag{1.38}$$

where

$$n_{\mathrm{crit}} = \frac{A_{21}}{C_{21}}, \tag{1.39}$$

is the critical density of the gas (Tielens, 2005; Draine, 2011).

When the density of the colliders $n_{\mathrm{H_2}}$ is larger than the critical density $\left(\frac{n_{\mathrm{crit}}}{n_{\mathrm{H_2}}} \rightarrow 0\right)$, collisions become important in de-excitation and the equation trends toward the standard Boltzmann equation and thermodynamic equilibrium. Therefore, in high density regions the population of the rotational energy levels are determined collisionally and the excitation temperature is thermalized across all levels to the kinetic temperature of the collider species (Kwok, 2007). When n_{crit} and $n_{\mathrm{H_2}}$ are equal, the rate of de-excitation by collisions and radiation are equal (Tielens, 2005; Kwok, 2007; Draine, 2011). Equation (1.38) holds the key to understanding the conditions under which a population of molecules are absorbing and emitting radiation and will be used to calculate the number of atoms in a unit area later in this thesis (column density).

1.4.2 Rotational Partition Function

In the ISM, the kinetic temperature of the gas is generally low (5-15 K). At low temperatures, only rotational transitions can be excited within the vibrational ground state, leading to purely rotational spectra. Rotational spectra are detected in the microwave range, at the low end of radio spectrum. The strength of microwave lines generated by rotational transitions is used to make measurements of the abundance of gas in a region.

The rotational partition function of a molecule describes the relative spectral line intensities of all transitions (Kwok, 2007; Mangum and Shirley, 2015). Taking Equation (1.38) and replacing the lower level by the ground-level n_0 and g_0, the total

number density of molecule species at temperature T relative to the ground-level is given by

$$\frac{n_i}{n_0} = \frac{\frac{g_i}{g_0} e^{-\frac{E_i}{kT}}}{1 + \frac{n_{\text{crit}}}{n_{\text{H}_2}}}, \tag{1.40}$$

so

$$N_{\text{tot}} = \frac{n_0}{g_0} \frac{1}{1 + \frac{n_{\text{crit}}}{n_{\text{H}_2}}} \sum_{i=0}^{\infty} g_i e^{-\frac{E_i}{kT_{\text{ex}}}}, \tag{1.41}$$

where g_i is the degeneracy of each energy level. The sum is called the partition function $Q(T)$ that describes how a population of N_{tot} molecules of a particular species are split into the available energy levels at temperature T. The ratio of the energy for each level E_i of the level and the excitation temperature T_{ex} sets the distribution of the molecules among the energy levels.

The energy contributing to the states of a molecule are partitioned in increasing order from nuclear, rotational, vibrational, to electronic sources and each appears on top of the other so that electronic energy levels split into vibrational energy levels, and vibrational energy levels into rotational energy levels, and the rotational energy levels into nuclear energy levels. For purely rotational transitions in the vibrational and electronic ground levels, rotational partition function is given by

$$Q_{\text{rotational}} = \sum_{J,K,I} g_J g_K g_I e^{-\frac{E_{JK}}{kT_{\text{ex}}}}, \tag{1.42}$$

$$= \sum_{J,K,I} (2J+1) g_K g_I e^{-\frac{E_{JK}}{kT_{\text{ex}}}}, \tag{1.43}$$

where g_J is described in Equation (1.23), g_K is equal to 1 for linear molecules and 2 for non-linear molecules, g_I is equal to 1 for linear molecules and has non-linear molecule specific values as computed for NH_3 in Equations (1.32) and (1.33), and E_{Jk} is the energy of the rotational level with quantum numbers J and k. More specifically for linear molecules,

$$Q_{\text{rotational}} = \sum_{J} (2J+1) e^{-\frac{BJ(J+1)}{kT_{\text{ex}}}}, \tag{1.44}$$

where $E_{\text{nuc}}^{\text{linear}}$ is given in Equation (1.16). The partition function for linear molecules can be estimated as

$$Q_{\text{rot}} = \frac{kT}{hB_0} e^{\frac{hB_0}{2kT_{\text{ex}}}}, \tag{1.45}$$

as shown in Mangum and Shirley (2015) and references therein, where the Planck constant h is folded into the definition of B in Equation (1.15) for brevity. The oblate symmetric top molecule NH_3 has a rotational partition function of the form

$$Q_{\text{rotational}} = \sum_{J=0}^{\infty} \sum_{k=-J,\ldots,J} (2J+1) g_k g_I e^{-\frac{BJ(J+1)+(C-B)k^2}{kT_{\text{ex}}}}, \tag{1.46}$$

where $E_{\text{nuc}}^{\text{oblate}}$ is given in Equation (1.22).

1.4.3 Dipole Moment

Transitions between energy levels occur as the result of the interaction between the perturbing radiation field in space and the electric or magnetic dipole moment of the rotating molecule (Mangum and Shirley, 2015). Pure rotational transitions only occur in molecules with a permanent dipole moment and electric-dipole transitions only occur between side-by-side rotational states ($\Delta J = \pm 1$ and $\Delta k = 0$). The intensity of rotational transitions is determined by the strength of the electric-dipole moment μ and the relative population of the two energy levels, as discussed previously (Bernath, 2016).

The transition dipole moment of a molecule represents the difference in charge across different states of a molecule (Demtröder, 2005). The expectation value of the transition dipole moment for a transition between states (J, k) and (J', k') is

$$|D_{21}|^2 = \mu_z^2 \frac{k^2}{J(J+1)}, \tag{1.47}$$

where

$$|\langle J, k| \mu^{\text{oblate}} |J, k\rangle|^2 = \mu_z^2 \frac{k^2}{J(J+1)}, \tag{1.48}$$

and

$$|\langle J,k|\,\mu^{\text{oblate}}\,|J-1,k\rangle\,|^2 = \mu_z^2\frac{J^2-k^2}{J(2J+1)} \tag{1.49}$$

for tunneling transitions between the same rotational states and emission transitions between J rotational states, respectively. The constant μ_z is the electric-dipole moment of the molecule along its non-zero molecule-fixed axis (Demtröder, 2005; Tielens, 2005). Because linear molecules only have transitions between the J rotational levels, the transition probabilities are derived by setting $k = 0$. The fractional terms in Equations (1.48) and (1.49) are called the line strengths S and represent the strength of the interaction between electric-dipole moment and the perturbing radiation field (Mangum and Shirley, 2015).

The Einstein A coefficient for radiative emission A_{21} is defined in terms of the expectation value of the electric dipole moment, $|D_{21}|^2$, as

$$A_{21} = \frac{64\pi^4\nu^3}{3hc^3}|D_{21}|^2, \tag{1.50}$$

where ν is the frequency of emitted radiation. The probability for spontaneous emission scales with the strength of electric-dipole of the molecule, hence only molecule with non-zero electric-dipoles undergo rotational transitions (Mangum and Shirley, 2015).

1.4.4 Radiative Transfer

Previously, only collisional excitation (C_{12}) and de-excitation (C_{21}) of molecules with radiative de-excitation (A_{21}) was considered. The relative population of the upper- and lower-states as scaled by the importance of collisions is given in Equation (1.38). Now we want to fold back in the radiative contributions to the formation and intensity of a spectral line. The contribution to the relative population of energy levels by spontaneous and stimulated emission only, is given by

$$n_1 B_{12}\int_0^\infty J_\nu\ \phi(\nu)\ \mathrm{d}\nu = n_2 A_{21} + n_2 B_{21}\int_0^\infty J_\nu\ \phi(\nu)\ \mathrm{d}\nu \tag{1.51}$$

where $\Phi(\nu)$ is the line profile function. Now, inserting Equation (1.38) with $\frac{n_{\rm crit}}{n_{\rm H_2}} \rightarrow 0$ into the above equation gives

$$B_{12} \int_0^\infty J_\nu \ \phi(\nu) \ \mathrm{d}\nu = \frac{g_2}{g_1} e^{-\frac{E_{21}}{kT}} \left(A_{21} + B_{21} \int_0^\infty J_\nu \ \phi(\nu) \ \mathrm{d}\nu \right). \tag{1.52}$$

implying that the level populations are in thermodynamic equilibrium. In thermodynamic equilibrium, the radiation field J_ν is described by

$$J_\nu = \frac{2h\nu^3}{c^3} \frac{1}{e^{\frac{E_{21}}{kT}} - 1}, \tag{1.53}$$

so that

$$\left(\frac{c^3}{2h\nu^3} A_{21} - \frac{g_1}{g_2} B_{12} \right) \left(e^{\frac{E_{21}}{kT}} - 1 \right) = \frac{g_1}{g_2} B_{12} + B_{21}, \tag{1.54}$$

taking the line profile to be normalized. By comparing terms

$$\frac{g_1 B_{12}}{g_2 B_{21}} = 1, \tag{1.55}$$

and

$$A_{21} = \frac{2h\nu^3}{c^3} B_{21}, . \tag{1.56}$$

The change in frequency specific intensity I_ν of radiation over a path length $\mathrm{d}s$ is given by

$$\frac{\mathrm{d}I_\nu}{\kappa_\nu \mathrm{d}s} = \frac{j_\nu}{\kappa_\nu} - I_\nu, \tag{1.57}$$

where j_ν is the emission coefficient and κ_ν is the absorption coefficient (Kwok, 2007; Mangum and Shirley, 2015). The emission coefficient is given in terms of the spontaneous emission coefficient as

$$j_\nu = \frac{h\nu}{4\pi} A_{21} n_2, \tag{1.58}$$

and the absorption coefficient is given in terms of the balance between the absorption and stimulated emission coefficients as

$$\kappa_\nu = \frac{h\nu}{4\pi} (n_1 B_{12} - n_2 B_{21}) \phi_\nu. \tag{1.59}$$

Inserting Equations (1.55) and (1.56) into the above equation yields

$$\kappa_\nu = \frac{c^2}{8\pi\nu^2}\frac{g_2}{g_1}n_1 A_{21}\left(1 - \frac{g_1 n_2}{g_2 n_1}\right)\phi_\nu, \tag{1.60}$$

where $E_{21} = h\nu$.

1.4.5 Measuring Column Densities

With the definition κ, we can solve $\kappa_\nu \mathrm{d}s = \mathrm{d}\tau_\nu$ for the optical depth by integrating and inserting Equation (1.50) into Equation (1.60) and Equation (1.38) rearranged for $\frac{g_2}{g_1}$ and $\frac{g_1}{g_2}$ with $\frac{n_{\mathrm{crit}}}{n_{\mathrm{H_2}}} \to 0$, as follows

$$\int \mathrm{d}\tau_\nu = \int n_2 \frac{8\pi^3\nu|D_{21}|^2}{3hc}\left(e^{\frac{E_{21}}{kT}} - 1\right)\phi_\nu \mathrm{d}s, \tag{1.61}$$

where $\mathrm{d}\tau_\nu$ encapsulates the effect of matter on the propagating radiation along its path. The energy level population n_2 is a function of the path length s because it counts the number of molecules in state 2. Integrating over the path length gives,

$$\tau_\nu = N_2 \frac{8\pi^3\nu|D_{21}|^2}{3hc}\left(e^{\frac{E_{21}}{kT}} - 1\right)\phi_\nu. \tag{1.62}$$

The frequency specific optical depth τ_ν is integrated over the spectral line variable ν' to obtain the total optical depth τ, as follows

$$N_2 = \frac{3hc}{8\pi^3\nu|D_{21}|^2}\left(e^{\frac{E_{21}}{kT}} - 1\right)^{-1}\int_0^\infty \tau_{\nu'}\mathrm{d}\nu'. \tag{1.63}$$

where ν is the frequency difference between level 2 and 1, as defined by $E_{21} = h\nu$. Setting $n_i = n_2$ in Equation (1.40) with $\frac{n_{\mathrm{crit}}}{n_{\mathrm{H_2}}} \to 0$ gives

$$\frac{n_2}{n_0} = \frac{g_2}{g_0}e^{-\frac{E_2}{kT}}, \tag{1.64}$$

where E_2 is the energy of the upper energy level. Solving the above equation for $\frac{n_0}{g_0}$ gives

$$\frac{n_0}{g_0} = \frac{n_2}{g_2}e^{\frac{E_2}{kT}}. \tag{1.65}$$

Inserting the above equation into Equation (1.41) allows for the total number density to be compared to the number density of energy level 2, as follows

$$N_{\rm tot} = \frac{n_2}{g_2} e^{\frac{E_2}{kT}} Q_{\rm rot}, \tag{1.66}$$

where the sum is given by rotational partition function $Q_{\rm rot}$. Now, the total number of molecules along pathlength s is calculated by inserting the above equation into Equation (1.63) for N_2, as follows

$$N_{\rm tot} = \frac{3hc}{8\pi^3 \nu |D_{21}|^2} \frac{Q_{\rm rot}}{g_2} e^{\frac{E_2}{kT_{\rm ex}}} \left(e^{\frac{E_{21}}{kT_{\rm ex}}} - 1 \right)^{-1} \int_0^\infty \tau_{\nu'} {\rm d}\nu', \tag{1.67}$$

where collisional excitation dominates so the gas is at a constant excitation temperature $T_{\rm ex}$ (Kwok, 2007; Mangum and Shirley, 2015). For emission lines in the optically thin limit, the integral over the optical depth is converted to integrated intensity

$$N_{\rm tot} = \frac{3hc}{8\pi^3 \nu \mu_z^2 S} \frac{Q_{\rm rot}}{g_J g_k g_I} e^{\frac{E_2}{kT_{\rm ex}}} \left(e^{\frac{E_{21}}{kT_{\rm ex}}} - 1 \right)^{-1} \int \frac{T_{\rm R}}{J_\nu(T_{\rm ex}) - J_\nu(T_{\rm bg})} {\rm d}\nu, \tag{1.68}$$

where the dipole moment is given by $|D_{21}|^2 = \mu_z^2 S$ in Equations (1.48) and (1.49), $J_\nu(T)$ is given by Equation (1.53), and $T_{\rm bg}$ is the background temperature. Converting to an integral over velocity, finally gives

$$N_{\rm tot} = \frac{3h}{8\pi^3 \mu_z^2 S} \frac{Q_{\rm rot}}{g_J g_k g_I} e^{\frac{E_2}{kT_{\rm ex}}} \left(e^{\frac{E_{21}}{kT_{\rm ex}}} - 1 \right)^{-1} \int \frac{T_{\rm R}}{(_\nu(T_{\rm ex}) - J_\nu(T_{\rm bg})} {\rm d}v. \tag{1.69}$$

Equation (1.69) describes the number of particles of a certain type along a column of gas of unit area, called the column density. As described above, it is built upon the quantum mechanical structure and symmetry of the molecule in question and the impact the environment on the statistical energy distribution of the molecules. Understanding how the environment of the cloud influences the distribution of energy among a molecule's energy levels allows for the number of molecules to be calculated from its emission lines.

1.4.6 Gas Conditions From Ammonia

The $J = k$ inversion transitions of NH_3 span a small range of frequencies and a large range of equivalent temperatures. The inversion transitions can often be detected

within the same observing frequency band, allowing for a diverse range of gas conditions to be probed during one observation. The NH_3 $J = k = 1$ and 2 inversion transitions probe gas with $T < 50$ K (Ho and Townes, 1983). The intensity of the observed inversion transitions are dependent on the population of the rotational energy levels, interaction with the external radiation field, collisional excitation with H_2, and absorption with the surrounding gas. In this thesis, the derived kinetic temperature of the NH_3 gas will be used as a proxy for the excitation temperature of the RCCs. Observing multiple spectral lines for a molecular species allows for the temperatures describing the rotational energy level populations $T_{\rm ex}$ and the kinetic temperature of the gas $T_{\rm kin}$ to be defined. Assuming the RCCs are in thermodynamic equilibrium with the same H_2 molecules as NH_3, $T_{\rm kin}$ for NH_3 can be used as a proxy for $T_{\rm ex}$ of the RCCs.

1.5 Radio Astronomy

Spectral line emission is observed with radio telescopes. Unlike optical telescopes, which use mirrors and lenses to collect and focus incoming light, radio telescopes use parabolic dish antennas and wave guides. Internally, a collected radio signal is amplified, frequency shifted, and spread out by a series of electronics. The final product is a radiation temperature spectrum in frequency or velocity space.

1.5.1 Telescope Optics

Single dish radio telescopes, like the GBT, are composed of a parabolic dish antenna. A telescope antenna can be analyzed as either a receiving or transmitting dipole according to the reciprocity theorem. If the antenna is assumed to be able to receive and transmit with no resistive losses, the only restriction on whether we can use a dipole antenna as a receiver and transmitter is the preferred direction of the intervening medium between the source and the receiver. For the GAS DR1 observations, we assume no significant impact of the intervening material or magnetic field on the

preferred direction of transmission through the cloud and so transmission and receiving has no preferred direction (Friesen et al., 2017). The reciprocity theorem states that the voltage U_1 induced by the source with current I_2 (labelled 2) on the antenna (labelled 1) is given by

$$U_1 I_2 = U_2 I_1. \tag{1.70}$$

The reciprocity theorem describes how the antenna can be treated as a transmitting beam coupled to the source being observed (Wilson et al., 2000).

The shape of the power pattern of a radio antenna is given by $P(\theta, \phi)$. The solid angle over which the power pattern $P_{\rm n}(\theta, \phi)$ is given by

$$\Omega_{\rm MB} = \iint_{\rm mainlobe} P_{\rm n}(\theta, \phi) {\rm d}\Omega, \tag{1.71}$$

where only the main lobe of the beam is integrated over, omitting the side lobes. Given a wave intersecting the receiving antenna, only a portion of the wave is observed. The antenna measures a total power per unit bandwidth W that can be characterized by an antenna temperature $T_{\rm A}$, which relates a temperature to the power of matched resistor so that

$$T_A(\theta_0, \phi_0) = \frac{\int T_{\rm b}(\theta, \phi) P_{\rm n}(\theta - \theta_0, \phi - \phi_0) \sin\theta \;\; {\rm d}\theta {\rm d}\phi}{\int P_{\rm n}(\theta, \phi) \;\; {\rm d}\Omega}, \tag{1.72}$$

where $T_{\rm b}(\theta, \phi)$ is the measured brightness temperature (Wilson et al., 2000).

The astronomical signal coming from the source to a radio telescope is reflected off the parabolic dish antenna to a sub-reflector suspended above the main dish, and directed toward a feed horn. The feed horn is a wave guide that directs the incoming signal to the electronics for amplification and mixing.

1.5.2 Amplification

The feed horn directs the radio signal with temperature $T_{\rm A}$ to the receiver electronics. Astronomical signals that enter the electronics of the radio telescope are noisy due

to the fundamental properties of the signal and the noise of the electronics. The minimum noise of a radio signal is given by Heisenberg's Uncertainty principle so that

$$T_{\rm rx} = \frac{h\nu}{k}, \tag{1.73}$$

which is characterized by the temperature $T_{\rm rx}$ at frequency ν. In reality, the electronics, atmosphere, and antenna also contribute to the overall noise of the signal (Wilson et al., 2000). The total noise contribution to the signal by the system $T_{\rm sys}$ is characterized by a sum of temperatures

$$T_{\rm sys} = \sum_i T_i. \tag{1.74}$$

Radio telescope electronics are designed so that $T_{\rm sys}$ is as low as possible. Because the signal also contributes to the overall noise, the system temperature describes the noise contributions by the whole system. The error on the sample of a signal is therefore given by $T_{\rm sys}$ to be

$$\Delta T = \frac{T_{\rm sys}}{\sqrt{\Delta\nu\tau}}, \tag{1.75}$$

which is dependent on the total sampling time τ and the receiver bandwidth $\Delta\nu$ (Wilson et al., 2000).

To compensate for the low power of incoming astronomical radio signals, the receiver must amplify the signal and provide gains on the order of 10^{14}. Instabilities in the gain are indistinguishable from fluctuations in $T_{\rm sys}$ and so they are related by

$$\frac{\Delta T}{T_{\rm sys}} = \frac{\Delta G}{G}. \tag{1.76}$$

Overall, the power signal measured by the receiver takes the form of

$$W = k(T_{\rm A} + T_{\rm sys})G\Delta\nu. \tag{1.77}$$

1.5.3 Heterodyne Systems

As previously discussed, high-gain amplifiers amplify the entire incoming signal, including the system and external contributions to the noise. Power leak from the output to the input is a major contribution to the noise of the system. To avoid contamination, the input signal is mixed with a local-oscillator signal that is produced by the electronics ν_L. The mixer combines the input voltage signal and the local oscillator voltage signal and relates it quadratically to the output current

$$I = \alpha U^2, \tag{1.78}$$

where α describes the power multiplier of the mixer and U is the sum of the two voltages (Wilson et al., 2000). The resultant band-passed signal is frequency shifted to an intermediate frequency band

$$\nu_{\mathrm{IF}} = \nu_S - \nu_L, \tag{1.79}$$

where ν_S is the input signal frequency.

The mixed intermediate frequency voltage signal is digitally sampled at time intervals according to the Nyquist theorem such that there are at least two samples per the highest frequency oscillation,

$$\nu_N = 2\nu_{HF}, \tag{1.80}$$

where ν_N is the Nyquist sampling frequency and ν_{HF} is the frequency of the highest frequency feature in the input signal (Wilson et al., 2000).

1.5.4 Spectrometer

The digitally sampled time series data $f(t)$ is fed into a digital Fourier spectrometer that transforms the data into the frequency domain in real time. The Fourier transform has the form

$$F(\nu) = \int_{-\infty}^{\infty} f(t) e^{-i\nu t} \ \mathrm{d}t. \tag{1.81}$$

The resultant frequency-space signal $F(\nu)$ contains the measured spectral line centered at the transition frequency if the emitting or absorbing material is stationary (Wilson et al., 2000).

1.6 The Green Bank Ammonia Survey (GAS)

This thesis utilizes NH_3, C_2S, and HC_5N K-band observations of the NGC 1333 and Orion A star forming regions detailed by Friesen et al. (2017). The NH_3 and RCC observations culminate the Green Bank Ammonia Survey (GAS) that was performed with the Green Bank Telescope and VEGAS spectrometer by co-PIs R. Friesen and J. E. Pineda. This section will detail the observational set up, including the imaging processes used to obtain GAS DR1 data dused in this thesis. As well, the resulting NH_3, C_2S, and HC_5N K-band observations will be described briefly, including major results for NGC 1333 and Orion A pertinent to this thesis.

1.6.1 The Green Bank Telescope

The Green Bank Telescope (GBT) is the world's largest fully-steerable single dish radio telescope (Prestage, 2006). The 100 m dish with unblocked aperature focuses incoming molecular emission into the K-band Focal Plane Array (KFPA) that has 7 beams with a spectral window of $18 - 27.5$ GHz. The GAS took advantage of the GBT's 85% of the celestial sphere available for observation and mapped NH_3, C_2S, and HC_5N emission in all of the closest star forming regions to Earth. At the distance to Orion A and NGC 1333 and the 23 GHz K-band, the GBT beam subtends a $0.02 - 0.03$ pc scale and resolves the Jeans length of 0.12 pc for gas at a density of $n = 10^4$ cm^{-3} and temperature of $T = 10$ K (Friesen et al., 2017).

1.6.2 The VEGAS Spectrometer

The VErsatile GBT Astronomical Spectrometer (VEGAS) spectrometer determines the spectral windows available for observation, allowing for simultaneous observa-

tion of NH_3 (1,1) (23.6944955 GHz), NH_3 (2,2) (23.7226336 GHz), C_2S $2_1 - 1_0$ (22.344030(1) GHz), and HC_5N $9 - 8$ (23.9639010 GHz) spectral lines. The VEGAS spectrometer was used in Mode 20 that split each KFPA beam into 8 spectral windows with a bandwidth of 23.44 MHz and 4096 spectral channels. The resultant spectral resolution is 5.7 kHz or $\Delta v \sim 0.07$ kms^{-1} per bin at the rest frequency of NH_3 (1,1) ($\sim$ 23.7 GHz). Due to limitations of the VEGAS spectrometer, the C_2S $2_1 - 1_0$ emission line is only observed in the central KFPA beam. As a result, the C_2S $2_1 - 1_0$ emission maps for NGC 1333 and Orion A have higher noise and a smaller foot print than the NH_3 (1,1), NH_3 (2,2), and HC_5N $9 - 8$ emission maps. Because the KFPA is set up as 7 feeds in a hexagonal pattern, the beam centres are separated by 94.88″ and require overlapping observations to ensure Nyquist sampling. Each region is scanned in $10' \times 10'$ squares along rows of R.A. separated by 13″ Dec. The coverage at the edges of the maps are variable and subject to increased rms noise (Friesen et al., 2017). Each map consists of position-position-velocity data per point and spectral line observed.

1.6.3 NH_3, C_2S, and HC_5N K-band Observations

In this thesis, the low-mass star forming region NGC 1333 and the high-mass star forming region Orion A are chosen because they span the extremes in star forming regimes. NGC 1333 is the most active star forming clump of dust and gas in the Perseus molecular cloud. NGC 1333 contains ~ 450 $M_\odot$ of molecular gas and dust in a ~ 1 pc^2 space at a distance of 299 pc (Zucker et al., 2018). Orion A is the closest high-mass star forming region to Earth and is composed of a dense, 12 pc long integral-shaped filament extending north and south. The northern portion of the integral-shaped filament is denser and narrower than the southern portion, containing $\sim 5 \times 10^3$ $M_\odot$ of gas and dust at a distance of 371 pc (Großschedl et al., 2018). The Orion A GMC is therefore home to a variety of environmental conditions, spanning very high- to low-density gas and dust (Friesen et al., 2017). Together, the environmental

conditions spanned by NGC 1333 and Orion A serve as an ideal laboratory in which to search for low-density chemistry processes, as detailed in the prior section.

The resultant K-band observations of the NH_3 (1,1) and NH_3 (2,2) spectral lines of NGC 1333 and Orion A were fit by Friesen et al. (2017) using the forward-modelling package `pyspeckit`. The fitting approach solves for the para-NH_3 (p-NH_3) column density ($N_{\mathrm{p-NH_3}}$), kinetic temperature (T_{K}), Local Standard of Rest (LSR) frame velocity (v_{LSR}), and line width (σ_v) of the NH_3 (1,1) and NH_3 (2,2) spectral lines simultaneously. The computed v_{LSR} is based on the centroid of the emission NH_3 (1,1) and the resultant map is used in the velocity-shifting procedure described below.

In general, Friesen et al. (2017) found that NH_3 (1,1) emission intensity correlates with H_2 column density. The authors also highlight the observation of faint NH_3 (1,1) emission between and around the dense structures in NGC 1333 and Orion A. NH_3 (2,2) emission is observed to follow the NH_3 (1,1) emission closely, but with lower signal-to-noise (SNR). HC_5N $9-8$ emission is observed toward a small compact region to the west of the central region in the NGC 1333 integrated intensity map, while C_2S $2_1 - 1_0$ emission is not observed. However, the presence of general diffuse C_2S $2_1 - 1_0$ emission is detected in the average spectra of the NGC 1333 region. RCC emission toward Orion A in both the integrated intensity maps and map averaged spectra is not detected. The observation of low-level NH_3 and RCC emission implies that low-density gas chemistry may be probed with spectral stacking techniques. The lack of C_2S or HC_5N emission in Orion A is of particular interest and serves as an ideal test case for extracting low-intensity emission from low-density and high-noise regions using spectral stacking.

1.7 Open Questions

A majority of chemical clock studies have been conducted as pointing surveys towards low- and high-mass cold, dense cores and clumps and protostars in MCs like the Taurus Molecular Cloud, the Pipe Nebula, Ophiuchus, Perseus, and Orion A (Suzuki

et al., 1992; Rosolowsky et al., 2008; Rathborne et al., 2008; Sakai et al., 2008; Foster et al., 2009; Hirota et al., 2009; Marka et al., 2012; Law et al., 2018). Additionally, mapping surveys have focused on clumps, cores, and star forming regions in the Taurus Molecular Cloud and Orion A (Hirahara et al., 1992; Ohashi et al., 2014; Dirienzo et al., 2015; Seo et al., 2019). This thesis serves to present observations of weak C_2S, HC_5N, and NH_3 emission across a range of density and temperatures, including the low-density edges of low-mass star forming clump NGC 1333 and the high-mass star forming MC Orion A. We present calculated RCC and NH_3 abundances as related to the local dust temperature $T_{\rm dust}$ (K) as a proxy for the radiation field strength and gas age as derived from YSO counts (Großschedl et al., 2019; Singh et al., 2022) to answer the following questions:

1. Do we observe a spatial correlation between abundances of C_2S and HC_5N, as originally observed by Suzuki et al. (1992)?

2. Do we observe a spatial anti-correlation between RCC abundances and NH_3 abundance, as also originally observed by Suzuki et al. (1992)?

3. Is the radiation field, with $T_{\rm dust}$ (K) as a proxy, correlated with RCC production, as modelled by Taniguchi et al. (2019); Kalvāns (2021)?

4. Is the radiation field, with $T_{\rm dust}$ (K) as a proxy, correlated with NH_3 production, as modelled by von Procházka and Millar (2021)?

5. Is the molecular abundance ratio NH_3/C_2S related to evolutionary stage, as first suggested by Suzuki et al. (1992)?

Before these questions are explored in Chapter 3, the methods for obtaining the molecular abundances will be described in Chapter 2.

Chapter 2

Methods

We use a spectral stacking method (sometimes also called "shuffling"; e.g., Schruba et al., 2011) in which line emission is shifted to a common velocity and added together within each region-of-interest (ROI) to improve the sensitivity to faint lines. Spectral stacking requires two components, a map of velocity priors and a spatial region over which to stack spectra. This section will discuss how we constructed the velocity prior maps, developed the spatial regions for stacking using Voronoi tesselation, stacked the spectral lines, fit the resultant stacked spectra, and calculated RCC column densities to check chemical clock relations in low-SNR regions of NGC 1333 and Orion A.

2.1 Construction of Velocity Fields

The left plots in Figures 2.1 and 2.2 show the GAS DR1 integrated intensity W (K km s^{-1}) maps for the NGC 1333 and Orion A star forming regions, respectively. The gas at every position in the NGC 1333 and Orion A NH_3 integrated intensity maps is at different line-of-sight velocities. To take advantage of the spectral stacking method in Schruba et al. (2011), we reassign the NH_3 and RCC velocity centroids according to ^{12}CO, ^{13}CO, and NH_3 emission in NGC 1333 to avoid spreading out the emission over a range of velocity bins (COMPLETE team, 2011b,a; Friesen et al., 2017; Kong et al., 2018).

We constructed the map so that the bright, extended emission of ^{12}CO creates a

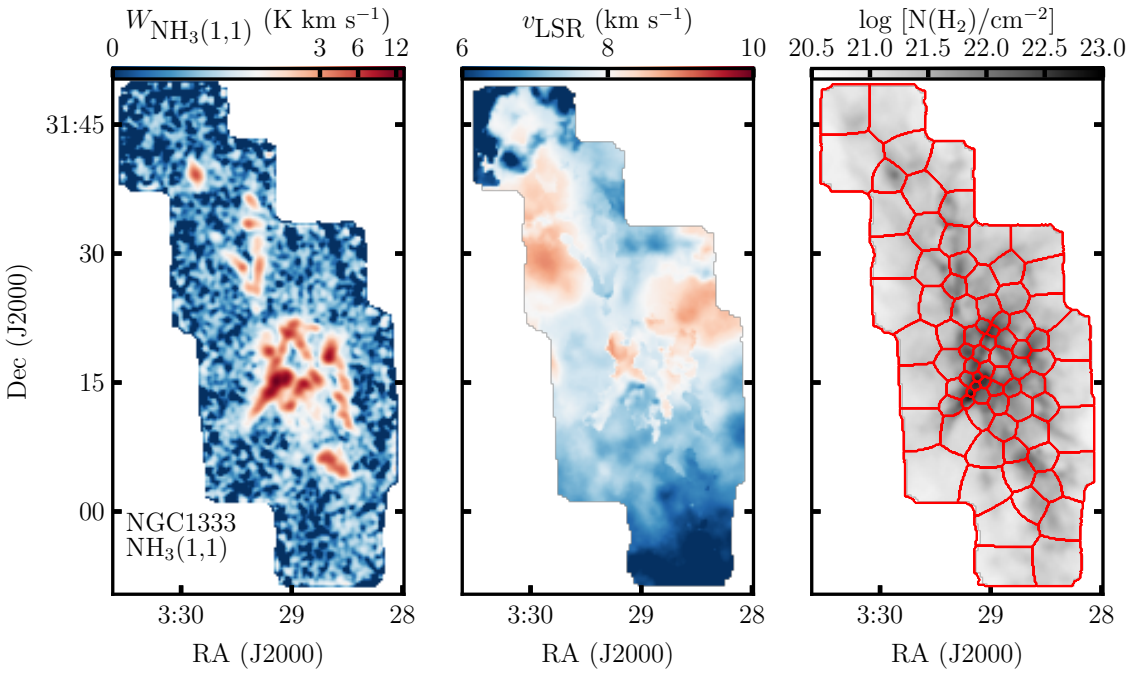

Figure 2.1: Left: Integrated intensity map for NH_3 (1,1) emission for the NGC 1333 region (Friesen et al., 2017). Middle: Centroid velocity field constructed from the hierarchical layering of ^{12}CO and ^{13}CO FCRAO emission maps, with the NH_3 (1,1) the GAS v_{LSR} map (COMPLETE team, 2011a,b; Friesen et al., 2017). Right: The H_2 column density in $\log_{10}[N(H_2)/cm^{-2}]$ derived from the Herschel submillimeter dust continuum (Singh et al., 2022). The Voronoi tesselated bin contours are overlaid in red.

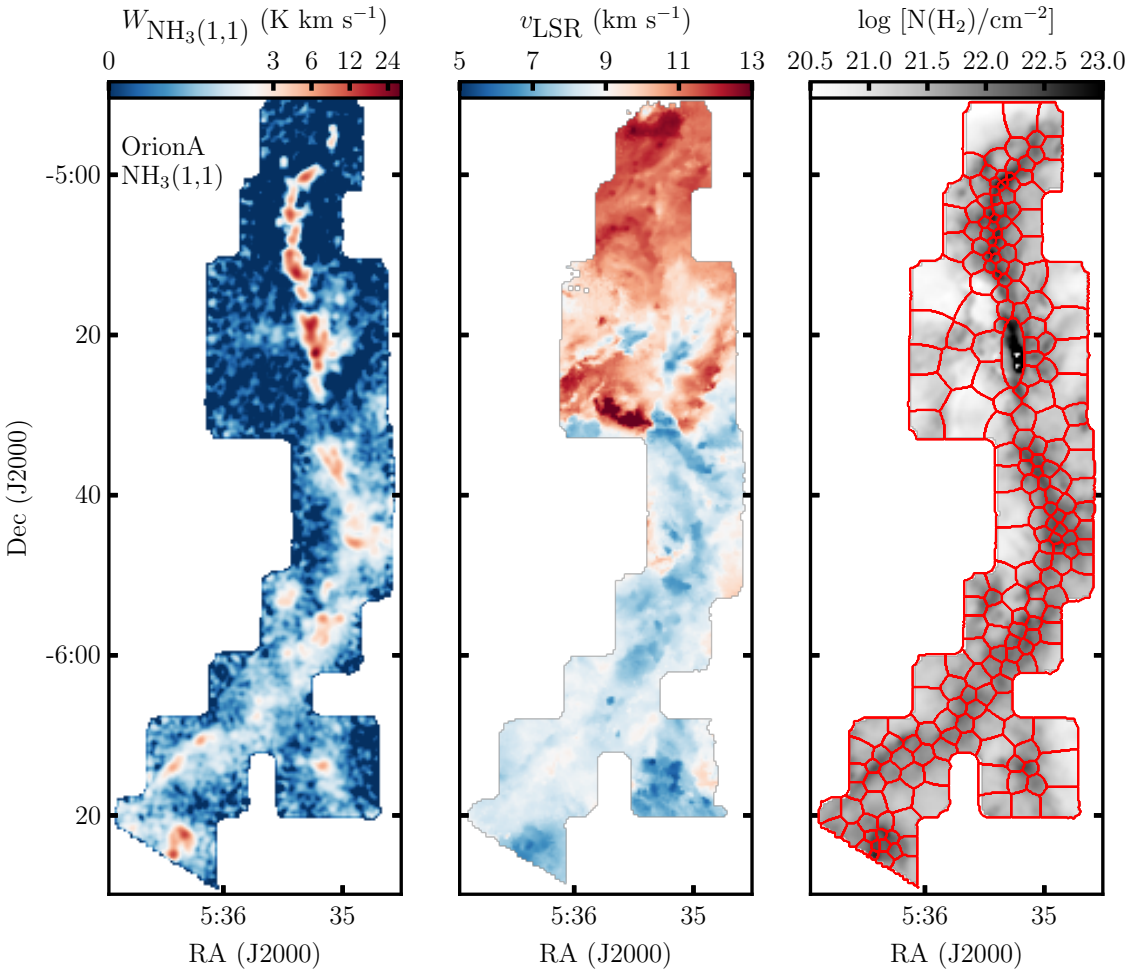

Figure 2.2: Left: Integrated intensity map for NH_3 (1,1) emission for the Orion A region (Friesen et al., 2017). Middle: Centroid velocity field constructed from the hierarchical layering of ^{12}CO and ^{13}CO CARMA-NRO emission maps, with the NH_3 (1,1) the GAS v_{LSR} map (Kong et al., 2018; Friesen et al., 2017). Right: The H_2 column density in $\log_{10}[N(H_2)/cm^{-2}]$ derived from the Herschel submillimeter dust continuum(Singh et al., 2022). The Voronoi tesselated bin contours are overlaid in red.

spatially complete base for the velocity field map. The centroid velocity of the NH_3 (1,1) and RCC emission is derived from the hierarchical layering of ^{12}CO and ^{13}CO emission maps from the FCRAO and CARMA-NRO surveys, respectively, and NH_3 v_{LSR} maps from GAS DR1 (COMPLETE team, 2011a,b; Friesen et al., 2017; Kong et al., 2018). We layered the isotopologue ^{13}CO and the NH_3 local-standard-of-rest velocity (v_{LSR}) maps consecutively on top in decreasing optical thickness. We use the resultant map to estimate the centroid velocities of NH_3 and RCC emission, as shown in the middle plots of Figures 2.1 and 2.2 for NGC 1333 and Orion A, respectively. Hierarchical layering of the velocity field guarantees that all positions in the GAS DR1 mapping region have a velocity estimate. The velocity centroids are chosen preferentially in descending order from NH_3, ^{13}CO, and ^{12}CO to take advantage of the likelihood of proxy for centroid velocity between the emission and velocity maps.

The typical rms in the NH_3 v_{LSR} maps is 0.007 km s^{-1} in NGC 1333 and 0.03 km s^{-1} in Orion A. To ensure further agreement between the CO v_{LSR} maps and the NH_3 v_{LSR} map, pixels in the NH_3 v_{LSR} map with rms error greater than 0.1 km s^{-1} were excluded. Further more, a boxed kernel convolution was performed across the hierarchical map. Pixels with greater than 0.25 km s^{-1} difference between the convolved map and the original hierarchical map were excluded from the NH_3 top-layer. Together, using error and convolution, pixels along the noisy outer edges of the NH_3 velocity map are excluded and the resulting hierarchical map is spatially smoothed. The final velocity field maps are illustrated in the middle plots of Figures 2.1 and 2.2 for NGC 1333 and Orion A, respectively

We assume that CO emission velocities are a good proxy for molecular gas velocities because bright CO emission coincides with all molecular gas emission. While this assumption may break down along lines-of-sight where there are significant opacity effects in the ^{12}CO spectra, these opaque lines-of-sight are coincident with where we have stronger ^{13}CO and NH_3 emission and hence use velocity information from these optically thinner lines.

2.2 Stacking of Spectral Lines

In addition to a velocity prior map that locates the molecular emission spectrally (Section 2.1), the spectral stacking method requires a spatial region over which to stack the molecular line emission. The spatial region is determined by binning the molecular hydrogen mass using the Voronoi binning method by Cappellari and Copin (2003) with the Weighted Voronoi Tessellation modification proposed by Diehl and Statler (2006). The original Voronoi binning method works in signal-to-noise (S/N) space to generate bins with total S/N scattered around a target S/N ratio. We modify this approach by binning to a target total mass of ~ 3 $M_\odot$ per bin for NGC 1333 and Orion A, using the Herschel molecular hydrogen dust maps generated by Singh et al. (2022) to measure mass per unit area. Binning the regions into units of constant mass aggregates the map into different ROIs that are large enough to improve the sensitivity of the maps, yet small enough to trace the variations in chemistry across the clouds. After tessellating each region, NGC 1333 has 83 bins with an average of ~ 4.5 $M_\odot$ and a standard deviation of $\sigma = 0.3$ $M_\odot$ and Orion has 227 bins with an average of ~ 5.9 $M_\odot$ with a standard deviation of $\sigma = 0.4$ $M_\odot$. We defined a single bin corresponding to the Orion KL high-mass star forming region to stabilize the Voronoi binning in the presence of steep mass gradients and missing pixel information. The bin enclosing the Orion KL has a mass of 8177 $M_\odot$. For both regions, the bins are at most 3σ from the average, with total masses of ~ 374 $M_\odot$ for NGC 1333 and ~ 9515 $M_\odot$ for Orion A. The scatter in bin mass and area is shown for the two regions in Figure 2.3.

Once the mass maps of NGC 1333 and Orion A are tessellated with mass bins, we apply Fourier stacking to obtain the average emission of each bin. Within each bin, we then shift each spectrum at every position to a common reference velocity of 0 km s^{-1} with the shift determined by the velocity maps (Section 2.1). After shifting, we averaged the spectra together to improve the S/N ratio. We carried out

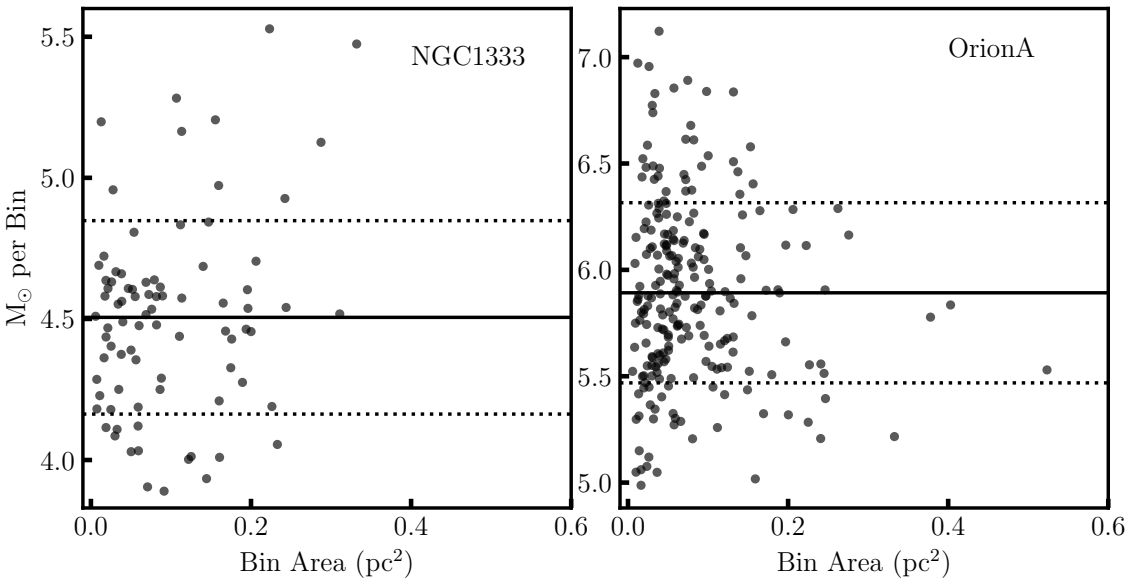

Figure 2.3: Physical bin area for NGC 1333 and Orion A in pc^2 plotted against the M$_\odot$ per bin. The solid black line is the average bin mass of ~ 4.5 M$_\odot$ and 5.9 M$_\odot$ for NGC 1333 and Orion A, respectively. The dashed lines indicate the 1σ scatter of the bin mass. The largest scatter in bin mass is $\sim 3\sigma$ from the average for both regions.

the shifting using the Fourier Shift theorem. We transform the intensity spectra, uniformly sampled in velocity space T_v, via the FFT to the frequency[1] domain: T_k (K). We then multiply the transformed spectrum by a linear phase term determined from the velocity prior maps in Figures 2.1 and 2.2. The shifted spectra in frequency-space take the form of

$$T_{k,\text{shift}} = T_k e^{-i2\pi m_k v_{k,\text{cent}}}, \tag{2.1}$$

where m_k is the frequency along the transformed spectral axis and $v_{k,\text{cent}}$ is the centroid of the emission. Performing the shifting procedure in frequency space allows a fraction-of-channel shifts that preserve the statistical properties of the spectra when inverse transformed back into velocity space. Because FFTs are inherently periodic, the Fourier shifting procedure wraps spectra so that the blueshifted and redshifted ends (and vice verse) meet. Thus, the spectra must be base lined appropriately to

[1]Here, we use "frequency" to refer to the Fourier frequency domain and not the electromagnetic wave frequency from which the velocity was determined using the Doppler shift. Formally, this Fourier frequency domain is the time domain of the received radio wave.

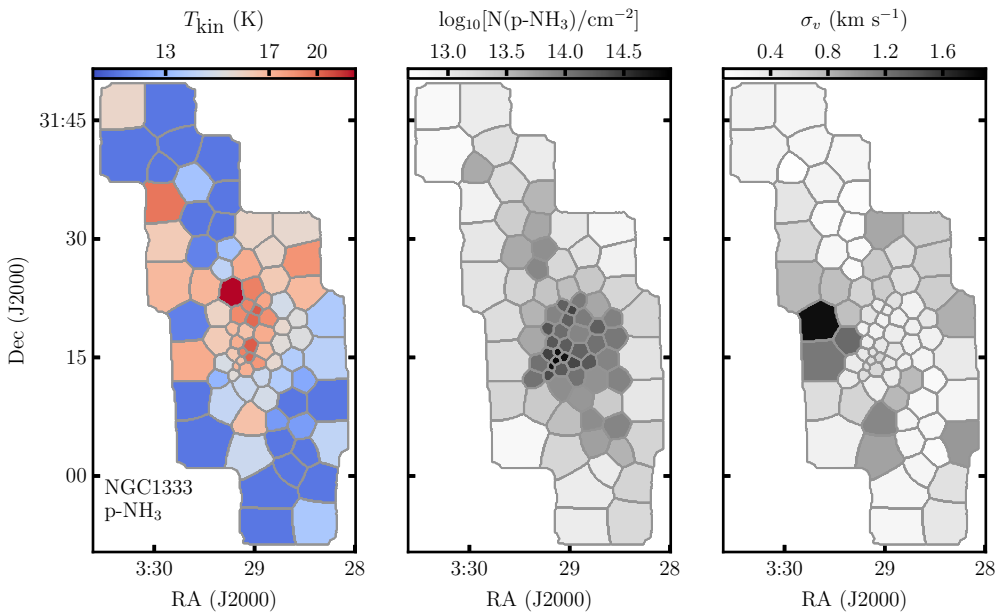

Figure 2.4: $T_{\rm kin}$, $\log_{10}$[N/cm^{-2}], and σ_v maps from NH_3 non-LTE model fits in NGC 1333 (Pettyjohn et al., 2021).

avoid jump discontinuities and corresponding edge effects in the final inverse transformed spectra.

The velocity shifted spectra are averaged together according to the mass bins shown in the right-most panel of Figures 2.1 and 2.2 for NGC 1333 and Orion A, respectively. The averaged spectra are fit with a Gaussian model for the C_2S and HC_5N emission in Section 2.3 and a non-LTE fitting method for the NH_3 (1,1) and NH_3 (2,2) emission developed by collaborators and described in Pettyjohn et al. (2021). The resultant NH_3 column densities are shown in Figure 2.6 as a function of H_2 column density for NGC 1333 (left) and Orion A (right). The histogram in Figure 2.6, with H_2 column density range of width 0.1 cm^{-2}, shows that NH_3 emission is observed across a range of H_2 column densities. The resulting spatial distribution of the computed NH_3 fit parameters, kinetic temperature $T_{\rm kin}$ (K), column density $\log_{10}$[N(p-NH_3)/cm^{-2}], and line width σ_v (km s^{-1}), are found in Figures 2.4 and 2.5 for NGC 1333 and Orion A, respectively.

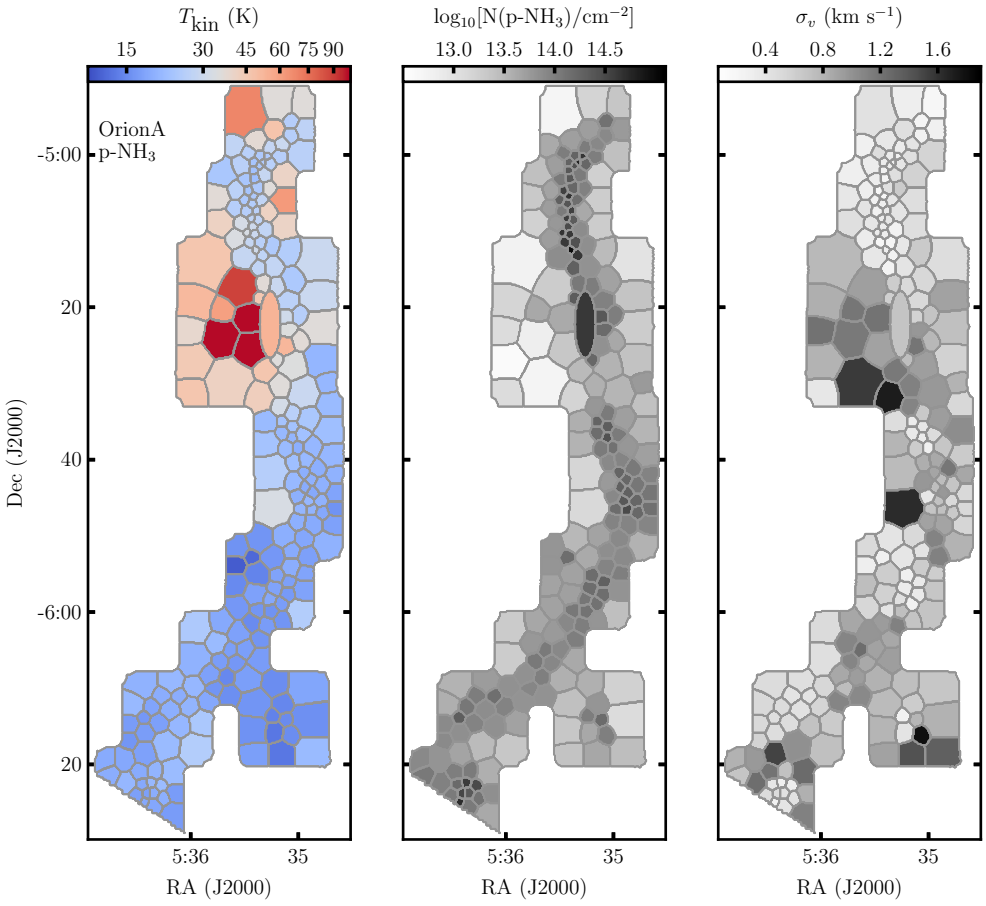

Figure 2.5: Same as Figure 2.4 but for Orion A.

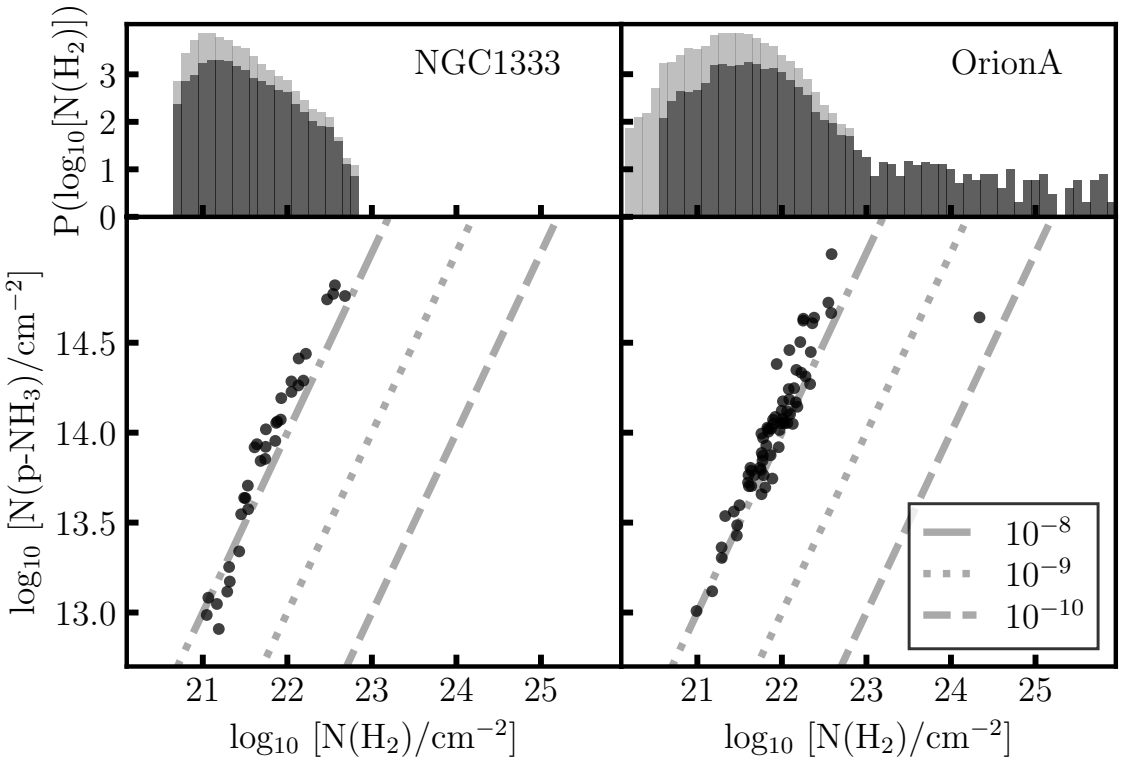

Figure 2.6: NH_3 fractional abundance per bin for NGC 1333 and Orion A. The dotted, dashed, and dash-dotted lines are lines of 10^{-9}, 10^{-10}, and 10^{-11} constant fractional abundance, respectively. The grey histogram represents the H_2 column density of all pixels in the region. The overlaid black histogram represents the pixels contributing the NH_3 detections.

2.3 Results of Spectral Line Stacking

The normalized Gaussian fits to the averaged RCC spectra were performed using `pyspeckit` with three parameters; line width σ_v (km s^{-1}), line centre v_0 (km s^{-1}), and the amplitude A (K) described by the brightness temperature T_b (K), as follows

$$T_b(v) = Ae^{-\frac{(v-v_0)^2}{2\sigma_v^2}}.$$

Although the velocity shifting procedure aligned all of the spectra along a common reference velocity of 0 km s^{-1}, the RCC emission peaked in a small range around 0 km s^{-1} and so the line centre was restricted to a range of -5 to 5 km s^{-1}. On average, the detected lines have centres at 0.01 km s^{-1} for C_2S and 0.004 km s^{-1} for HC_5N in NGC 1333. For Orion A, the detected lines have centres at -0.002 km s^{-1} for C_2S and -0.08 km s^{-1} for HC_5N. The mismatch in reference velocity to the rare species emission is due to our assumption the ^{12}CO, ^{13}CO, and NH_3 gas composing the velocity prior map directly corresponds to the same gas emitting the RCCs. The averaged spectra and corresponding RCC Gaussian fits for four of the mass bins in NGC 1333 and Orion A are shown in Figures 2.7 and 2.8, respectively. The leftmost column shows the NH_3 emission (red) with non-LTE fit (blue; discussed in Pettyjohn et al., 2021) and the right set of four columns show the RCC emission and corresponding Gaussian fits.

We used the Bayesian Information Criterion (BIC) to identify non-detections of faint RCC emission (Kass and Raftery, 1995). The BIC was computed for two models, an empty background with one parameter describing its level and a Gaussian spectral line with the three parameters described previously. The difference between the BIC for the zero-model and the Gaussian-model, called ΔBIC describe the evidence against the model with the larger BIC. ΔBIC is given by

$$\Delta\text{BIC} = \text{BIC} - \text{BIC}^*,$$

where BIC* is the model with the smaller computed BIC.

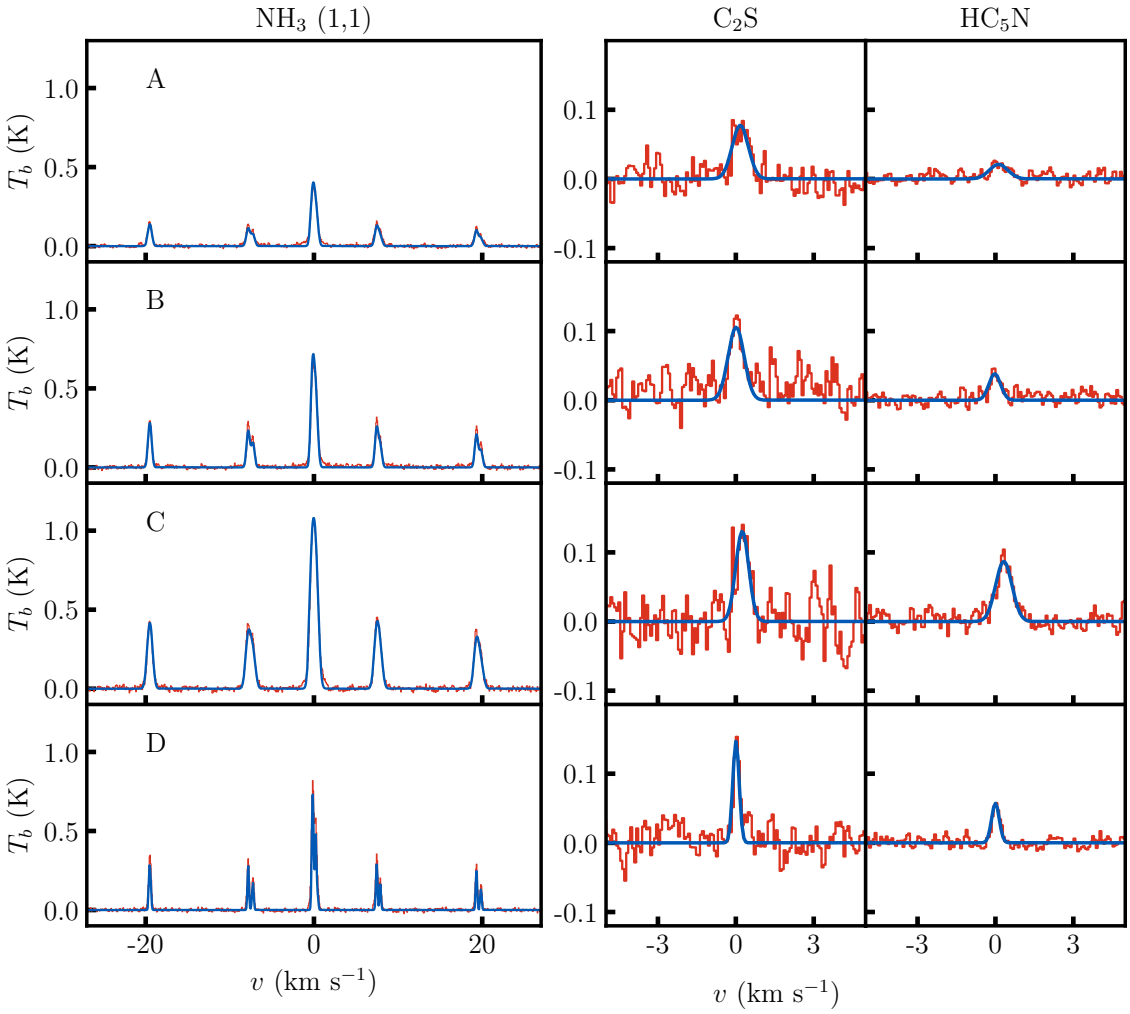

Figure 2.7: NH_3 (1,1) emission (left column) for four Voronoi bins that coincide with RCC emission in NGC 1333. Corresponding RCC emission for the four Voronoi bins are in the right plots. Each column is labelled by the corresponding emitting species and each row pertains to one Voronoi bin. The rare species C_2S and HC_5N are detected all four chosen bins.

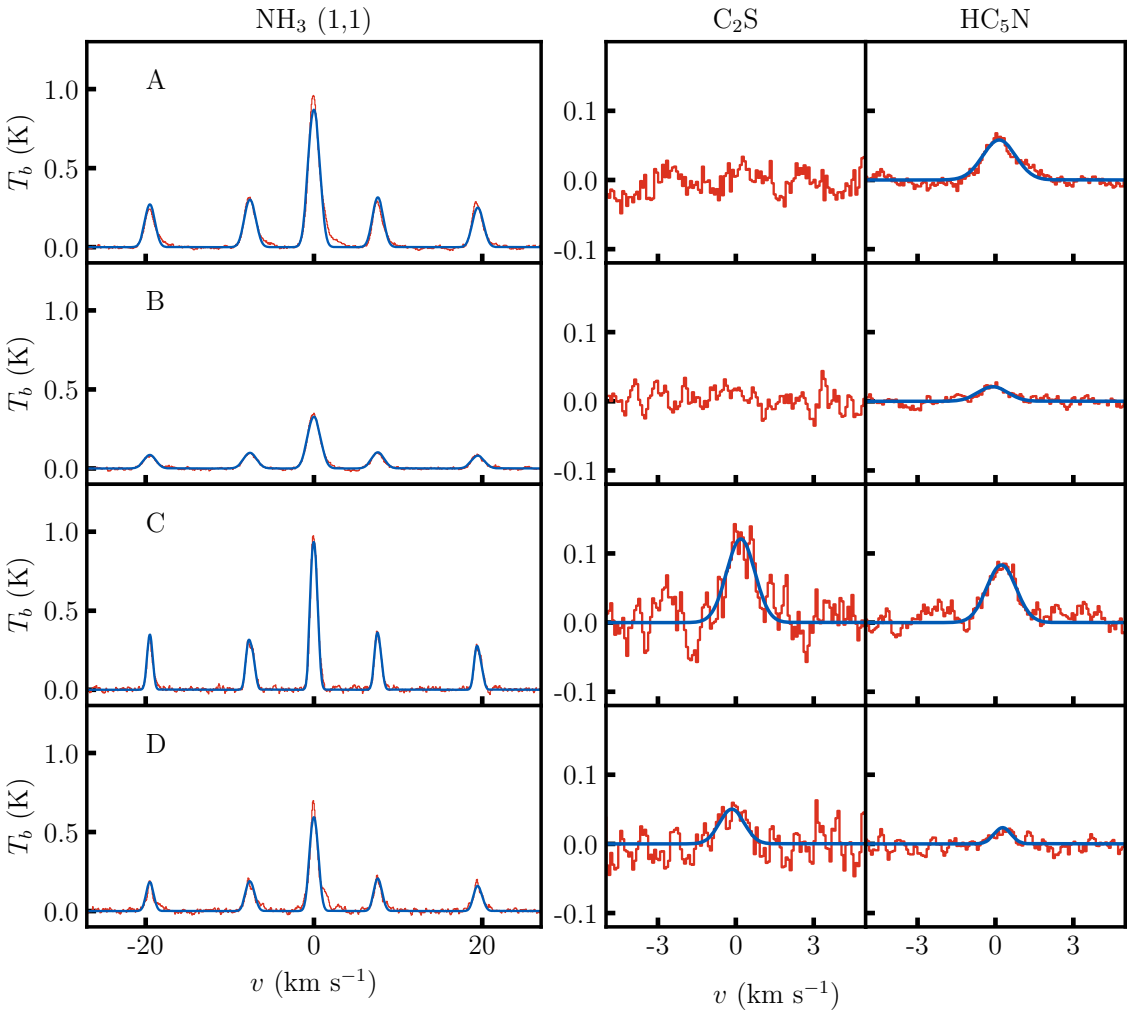

Figure 2.8: Same as Figure 2.7 but for Orion A.

A cutoff of ΔBIC = 20 for all Gaussian-models with the larger BIC than the zero-model was chosen heuristically. Gaussian-models with a ΔBIC < 20 are not considered to have enough evidence against the zero-model to be a detection for the analyses in this thesis. Additionally, we restricted the line width to be $<$0.75 km s^{-1} to eliminate fitting to baseline features rather than actual RCC emission. The ΔBIC cutoff and line width upper limit criteria result in the RCC detections contained in Tables 2.1 and 2.2 for NGC 1333 and Orion A, respectively. In general, detections with ΔBIC close to 20 should be treated with caution. The resulting spatial distribution of C_2S and HC_5N intensity in NGC 1333 and Orion A for detections is found in Figures 2.9 and 2.10, respectively.

Species		RA (hh:mm:ss)	Dec (dd:mm:ss)	ΔBIC	W (K km s^{-1})	σ_v (km s^{-1})	$N_{tot}^{thin}/10^{12}$ (cm^{-2})
C_2S		03:29:20	+31:12:15	57	0.07(2)	0.38(7)	1.8(4)
		03:29:04	+31:11:26	38	0.06(2)	0.5(1)	1.7(5)
		03:28:56	+31:12:42	31	0.04(2)	0.23(5)	1.1(3)
		03:29:05	+31:13:34	34	0.08(1)	0.41(7)	2.6(5)
		03:28:46	+31:06:57	28	0.04(2)	0.13(3)	0.9(2)
	A	03:28:43	+31:04:45	101	0.06(1)	0.31(4)	1.6(2)
		03:29:16	+31:14:01	36	0.03(1)	0.13(3)	1.0(3)
		03:29:12	+31:15:20	25	0.07(1)	0.29(5)	2.1(5)
		03:28:49	+31:14:29	107	0.14(2)	0.43(6)	4.2(7)
		03:29:03	+31:15:05	33	0.09(2)	0.6(1)	3.2(7)
		03:29:10	+31:16:58	22	0.06(2)	0.26(5)	1.9(5)
		03:28:54	+31:15:41	29	0.05(2)	0.34(7)	1.6(5)
		03:28:31	+31:12:11	48	0.08(5)	0.7(1)	2.1(5)
		03:28:19	+31:09:31	61	0.02(2)	0.13(2)	0.4(1)
	B	03:28:34	+31:06:03	116	0.084(5)	0.31(3)	2.2(3)
		03:28:29	+31:03:11	73	0.04(1)	0.11(2)	1.0(2)
		03:28:34	+31:17:34	27	0.055(8)	0.5(1)	1.6(4)

	C	03:28:42	+31:18:43	65	0.08(2)	0.25(4)	2.5(4)
		03:28:35	+31:19:54	56	0.07(2)	0.51(9)	2.1(5)
		03:28:30	+31:23:08	57	0.04(2)	0.6(1)	1.3(3)
		03:29:49	+31:24:20	27	0.01(1)	0.13(3)	0.4(1)
		03:29:19	+31:35:07	33	0.025(5)	0.3(6)	0.6(2)
		03:29:34	+31:32:43	31	0.028(7)	0.22(5)	0.7(2)
		03:29:36	+31:37:08	34	0.022(8)	0.2(5)	0.6(2)
	D	03:29:54	+31:38:59	114	0.047(8)	0.12(1)	1.2(2)
		03:29:45	+31:41:31	41	0.019(7)	0.2(4)	0.5(1)
HC_5N		03:28:46	+31:06:57	22	0.01(2)	0.17(4)	0.17(6)
	A	03:28:43	+31:04:45	58	0.02(2)	0.36(5)	0.33(7)
		03:29:11	+31:13:48	80	0.04(2)	0.28(3)	0.7(1)
		03:28:57	+31:14:20	91	0.04(1)	0.44(6)	0.7(1)
		03:28:49	+31:14:29	242	0.06(2)	0.26(2)	1.0(1)
		03:29:03	+31:15:05	75	0.04(1)	0.48(5)	0.8(1)
		03:29:07	+31:15:38	51	0.03(1)	0.27(5)	0.6(1)
		03:28:31	+31:12:11	33	0.01(1)	0.23(5)	0.21(7)
	B	03:28:34	+31:06:03	87	0.02(2)	0.23(3)	0.38(7)
	C	03:28:42	+31:18:43	394	0.08(2)	0.32(2)	1.3(1)

	03:29:30	+31:28:25	46	0.01(2)	0.27(5)	0.21(6)
	03:29:54	+31:34:35	20	0.01(2)	0.5(1)	0.27(9)
D	03:29:54	+31:38:59	158	0.02(2)	0.15(1)	0.37(5)

Table 2.1: NGC 1333 RCC bin detections, including bin locations, ΔBIC, integrated intensity W, line width σ_v, and column density $N_{\rm tot}^{\rm thin}$. The four bins in Figure 2.7 are labelled here.

Species		RA (hh:mm:ss)	Dec (dd:mm:ss)	ΔBIC	W (K km s^{-1})	σ_v (km s^{-1})	$N_{tot}^{thin}/10^{12}$ (cm^{-2})
C_2S		05:35:21	−05:18:36	38	0.09(2)	0.7(1)	6(1)
		05:35:04	−05:35:43	25	0.09(3)	0.4(9)	3(1)
		05:34:58	−05:36:43	25	0.04(1)	0.15(4)	1.4(4)
		05:35:01	−05:38:28	44	0.12(3)	0.57(9)	4.2(9)
		05:34:52	−05:38:16	33	0.07(2)	0.7(1)	2.6(7)
		05:35:02	−05:42:48	42	0.032(8)	0.35(6)	1.1(3)
		05:35:11	−05:00:05	25	0.05(1)	0.28(5)	2.2(6)
		05:34:47	−05:45:24	46	0.08(2)	0.39(7)	2.8(6)
	C	05:35:26	−05:52:49	153	0.17(2)	0.54(5)	4.6(6)
		05:35:33	−05:53:53	66	0.034(8)	0.25(4)	0.9(2)
		05:35:23	−05:55:02	28	0.03(1)	0.47(9)	1.0(3)
		05:35:16	−05:58:19	29	0.03(1)	0.19(5)	1.0(3)
	D	05:35:23	−05:59:47	22	0.06(2)	0.48(9)	1.8(4)
		05:35:15	−05:59:54	29	0.05(2)	0.28(7)	1.4(4)
		05:35:30	−06:04:58	36	0.04(1)	0.5(1)	1.3(3)
		05:36:12	−06:12:45	31	0.05(2)	0.5(1)	1.7(5)
		05:34:56	−06:14:10	21	0.009(2)	0.19(5)	0.18(7)

		05:36:26	−06:15:38	60	0.06(1)	0.46(8)	1.7(4)
		05:36:15	−06:24:24	57	0.09(2)	0.58(9)	3.0(7)
		05:36:21	−06:25:17	194	0.09(2)	0.7(1)	2.9(5)
		05:36:25	−06:24:55	23	0.1(3)	0.29(6)	3.1(9)
HC_5N		05:35:27	−05:11:27	123	0.07(1)	0.36(4)	1.8(3)
		05:35:24	−05:12:29	395	0.16(1)	0.42(2)	4.1(3)
		05:35:20	−05:13:09	47	0.04(1)	0.32(6)	0.9(2)
		05:35:22	−05:11:34	29	0.019(6)	0.14(3)	0.4(1)
		05:35:25	−05:10:23	26	0.05(1)	0.26(5)	1.2(3)
		05:35:21	−05:18:36	198	0.076(8)	0.7(5)	2.7(3)
		05:35:12	−05:17:21	96	0.027(1)	0.33(5)	0.6(1)
		05:35:07	−05:19:16	87	0.03(4)	0.6(6)	0.7(1)
	A	05:35:07	−05:21:10	455	0.103(6)	0.63(3)	2.7(1)
	B	05:34:59	−05:21:08	147	0.034(5)	0.57(5)	0.8(1)
	Orion KL	05:35:23	−05:08:28	1238	0.072(2)	0.66(1)	3.3(1)
		05:35:28	−05:07:25	20	0.019(7)	0.26(7)	0.4(2)
		05:34:59	−05:24:27	185	0.038(5)	0.48(4)	1.1(1)
		05:35:07	−05:24:58	28	0.01(4)	0.5(1)	0.4(1)
		05:35:13	−05:27:00	273	0.125(8)	0.67(3)	3.6(2)

	05:35:03	−05:27:31	153	0.0265(9)	0.45(3)	0.55(6)
	05:34:57	−05:31:18	30	0.008(2)	0.4(8)	0.15(5)
	05:35:04	−05:34:05	69	0.0327(9)	0.7(1)	0.6(1)
	05:35:21	−05:05:53	21	0.0077(9)	0.14(3)	0.29(9)
	05:35:30	−05:05:52	33	0.018(5)	0.11(2)	0.4(1)
	05:35:08	−05:36:23	23	0.01(5)	0.19(6)	0.19(7)
	05:35:34	−05:04:54	39	0.015(5)	0.27(6)	0.3(1)
	05:35:19	−05:02:27	35	0.0266(7)	0.46(7)	0.8(2)
	05:35:33	−05:51:30	24	0.029(8)	0.6(1)	0.5(1)
C	05:35:26	−05:52:49	334	0.13(1)	0.56(3)	2.1(2)
D	05:35:23	−05:59:47	41	0.021(6)	0.32(6)	0.36(9)
	05:35:33	−06:02:42	39	0.012(4)	0.29(5)	0.21(7)
	05:35:45	−06:04:05	50	0.018(1)	0.68(9)	0.45(9)
	05:36:21	−06:12:38	21	0.009(2)	0.13(4)	0.15(6)
	05:36:10	−06:21:10	140	0.043(7)	0.59(6)	0.9(1)
	05:36:17	−06:22:44	61	0.04(8)	0.31(4)	0.8(2)
	05:36:22	−06:22:20	34	0.06(1)	0.47(8)	1.1(3)
	05:36:15	−06:24:24	54	0.038(8)	0.57(8)	0.7(1)
	05:36:21	−06:25:17	120	0.05(7)	0.69(6)	0.9(1)
	05:36:25	−06:24:55	328	0.13(1)	0.39(3)	2.4(2)

	05:35:22	−05:08:37	62	0.08(2)	0.34(5)	2.3(4)

Table 2.2: Same as Table 2.1 but for Orion A.

2.4 Calculating Carbon Chain Column Densities

We calculated the column density for the RCCs based on Mangum and Shirley (2015) as described in Section 1.4.5 using the excitation temperature $T_{\rm kin}$ (K) from the NH_3 fits described in Pettyjohn et al. (2021) and shown in the right plots of Figures 2.4 and 2.5 and the molecular constants in Table 2.3. We assume the RCC molecules are in thermodynamic equilibrium with the same H_2 molecules as NH_3 and dominated by collisional excitation. Our assumptions lead to an upper bound calculation for RCC column density. Approximating that the emission is optically thin, we calculated the column densities using Equation (1.69). Converting to binned velocity-space, Equation (1.69) takes the form

$$N_{\rm tot}^{\rm thin} = \left(\frac{3h}{8\pi^3 S\mu^2}\right)\left(\frac{Q_{rot}}{g_J g_K g_I}\right)\frac{\exp\left(\frac{E_u}{kT_{kin}}\right)}{\exp\left(\frac{h\nu}{kT_{ex}}\right)-1} \times \frac{1}{J_\nu(T_{\rm kin})-J_\nu(T_{\rm bg})}\sum T_{\rm b}(v_i)\Delta v_i, \tag{2.2}$$

where $Q_{\rm rot}$ is the rotational partition function as derived for linear molecules in Equation (1.45), S is the line strength defined in Section 1.4.2 as the fractional terms in Equations (1.48) and (1.49), g_J, g_K, and g_I are the rotational and nuclear degenercies calculated and defined in Section 1.3.2, $J_\nu(T_{\rm kin})$ and $J_\nu(T_{\rm bg})$ are the radiation field defined by Equation (1.53), $T_{\rm bg}$ is the cosmic background temperature 2.73 K, $T_{\rm kin}$ is the RCC excitation temperature as derived from the NH_3 kinetic temperature in the left plot of Figures 2.4 and 2.5, Δv_i is the velocity channel width that is set to 0.08 km s^{-1} from Friesen et al. 2017, E_u is the energy for the upper level, and $T_b(v_i)$ is the measured brightness temperature in velocity-space per bin v_i. The resulting fractional abundances of C_2S and HC_5N with H_2 are shown in Figures 2.11 and 2.12 for NGC 1333 and Orion A, respectively. The histogram shows the number of pixels with H_2 column density range of width 0.1 cm^{-2} contributing to the RCC detections. In general, C_2S is found in pixels with lower column density than HC_5N.

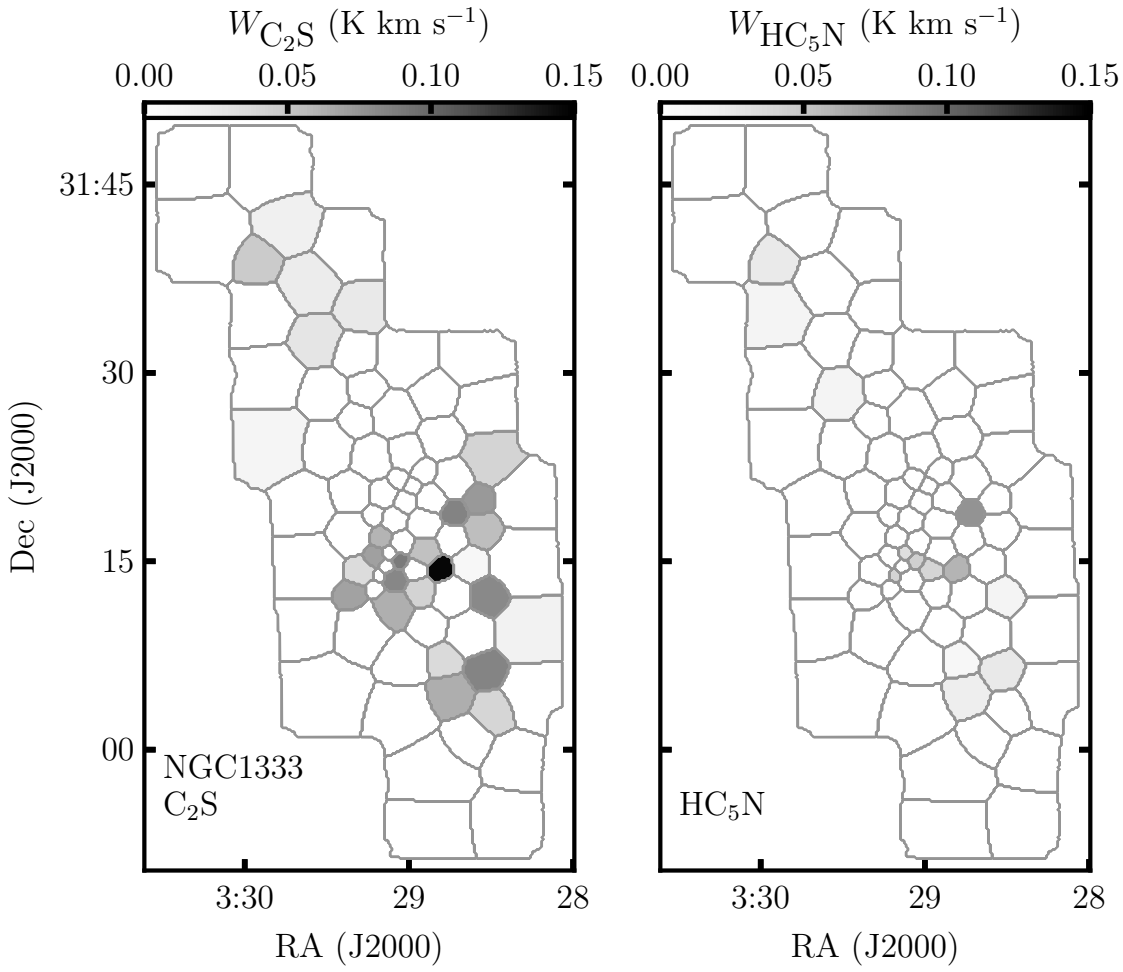

Figure 2.9: Intensity of C_2S and HC_5N emission in NGC 1333. Each bin is filled according to the detected spectral line intensity W (K km s^{-1}).

Species	Transition	ν (GHz)	E_u (cm^{-1})	S	B (GHz)	μ (debye)
C_2S	$J_N = 2_1 - 1_0$	22.344030(1)	1.11622	0.40	6.477750	2.88
HC_5N	$J = 9 - 8$	23.9639010	3.99675	0.47	1.3313327	4.33

Table 2.3: RCC molecular constants used to calculate column density. All constants are from CDMS (Müller et al., 2001, 2005).

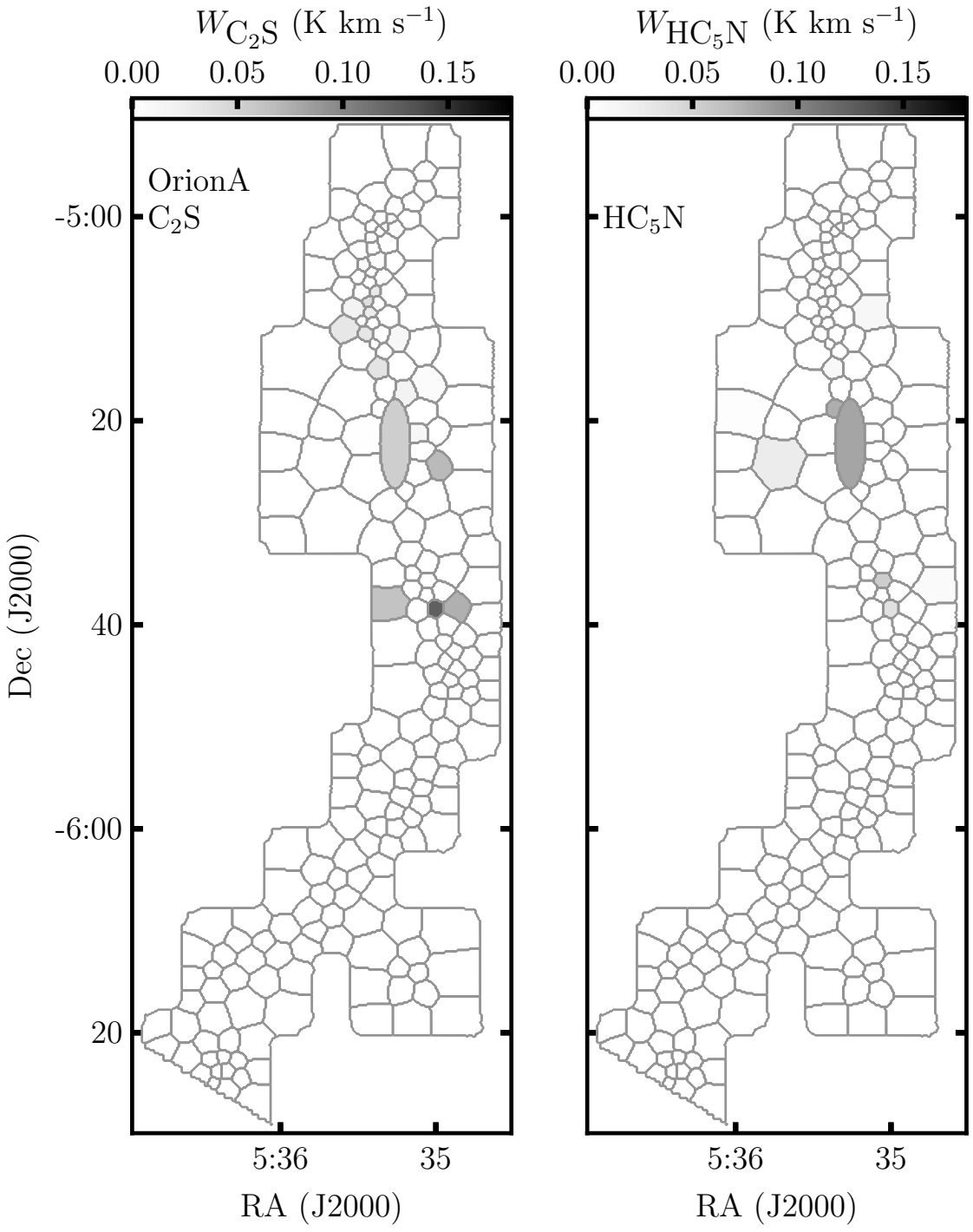

Figure 2.10: Same as Figure 2.9 but for Orion A.

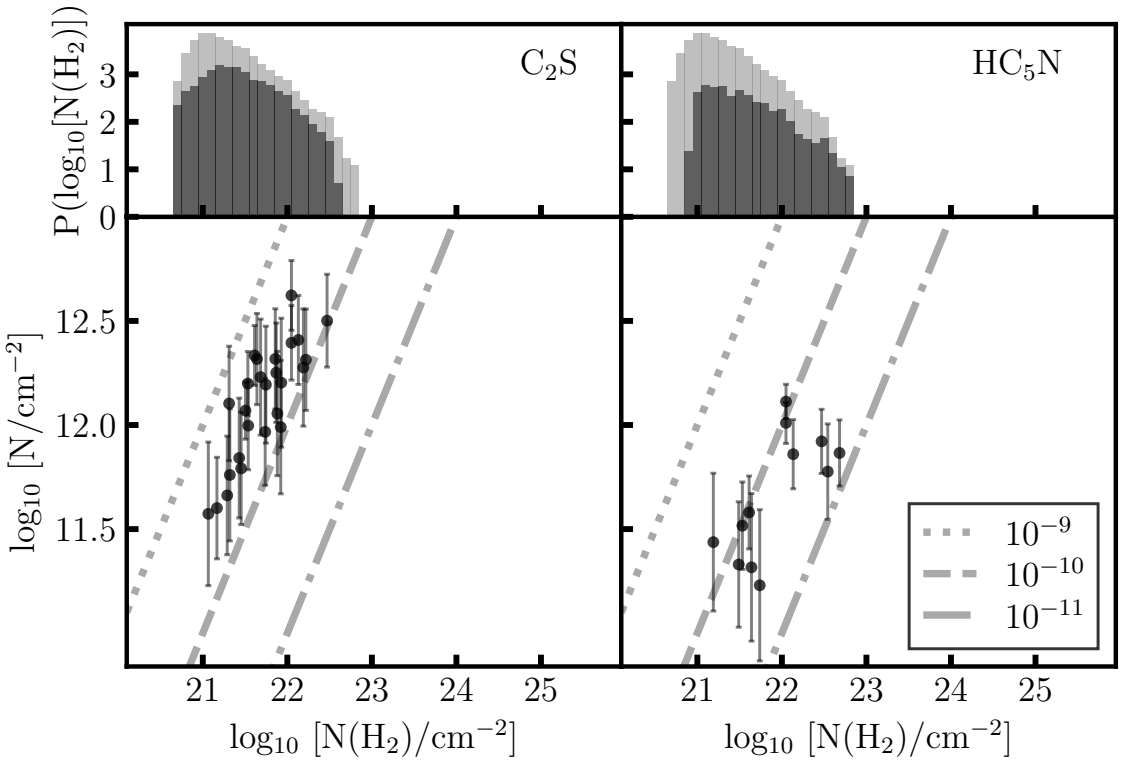

Figure 2.11: C_2S and HC_5N fractional abundance per bin for NGC 1333. The dotted, dashed, and dash-dotted lines are lines of 10^{-8}, 10^{-9}, and 10^{-10} constant fractional abundance, respectively. The grey histogram represents the H_2 column density of all pixels in the region. The overlaid red histogram represents the pixels contributing the rare-carbon chain detections.

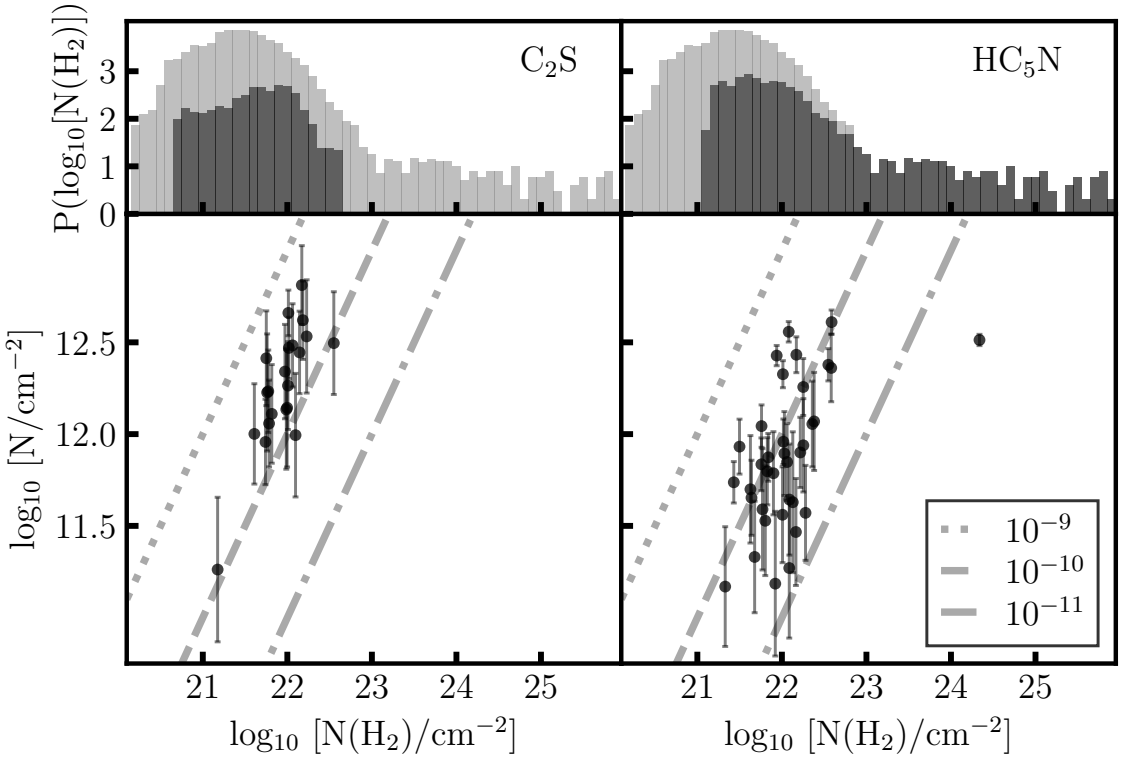

Figure 2.12: Same as Figure 2.11 but for Orion A.

Chapter 3

Abundance Variation of Dense Gas Tracers

In this chapter, we will bring together star formation, chemistry, and molecular line observations to study RCC and NH_3 chemical abundance variations across star forming regions NGC 1333 and Orion A described in Chapters 1 and 2. We will explore abundance variations with line width σ_v (km s^{-1}), column density N (cm^{-2}), dust temperature as a proxy for the radiation field $T_{\rm dust}$ (K) (shown in Figures 3.1 and 3.2; Singh et al. (2022)), and bin age as classified by YSO count from the VISION YSO catalogue (Großschedl et al., 2019). Chemical abundances are measured by the column density N (cm^{-2}) described in Section 2.4, with the corresponding line widths σ_v derived from the Gaussian fits described in Section 2.3.

To analyse RCC and NH_3 column density ratios as chemical clocks, we use the YSO catalogue from the Vienna survey in Orion (VISION) to classify the relative ages of each Voronoi tessellated ROI. Note that NGC 1333 YSO catalogues have been received, but too late to be incorporated into this thesis. NGC 1333 analysis with YSO count information will be provided in Pettyjohn et al. (2021). We created three classifications: regions devoid of YSOs, "young" regions, and "old" regions using the Class 0 through Class III (protostars with disks). According to Großschedl et al. (2019), Class 0 objects are objects in the very early stage of envelope collapse, Class I objects are protostars embedded in the still accreting envelope, Class II and

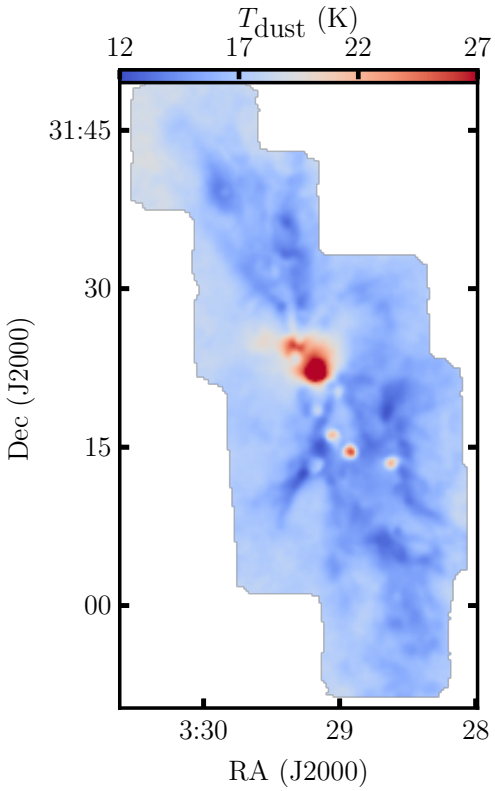

Figure 3.1: $T_{\rm dust}$ (K) map for NGC 1333 calculated in Singh et al. (2022).

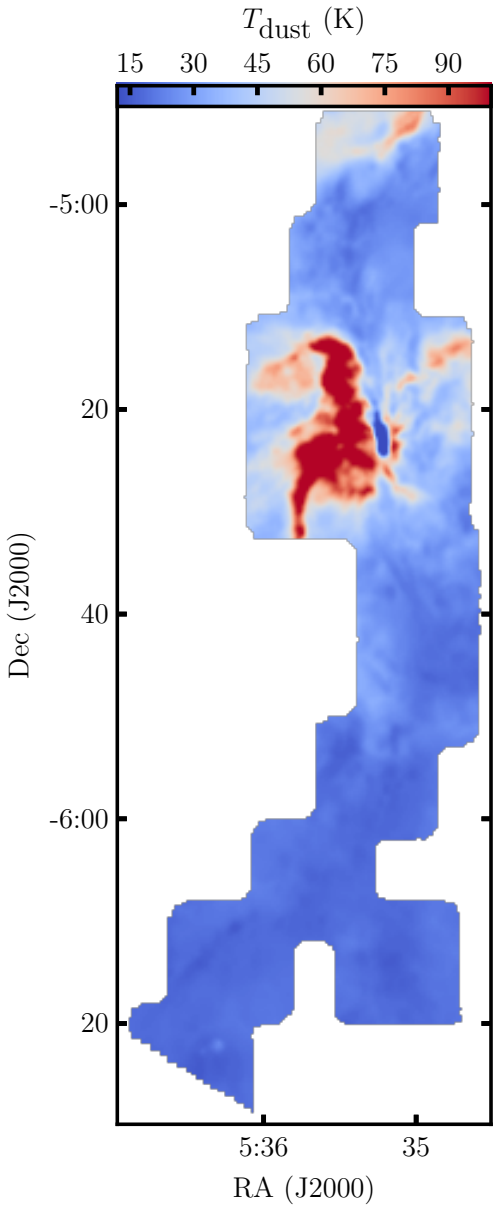

Figure 3.2: Same as Figure 3.1 but for Orion A.

III objects are pre-main-sequence stars that have emerged and become unembedded from the accreting gas, and flat spectrum sources that lie between Class I and II. Together, Orion A contains a total of 188 protostars, 185 flat spectrum sources, and 2607 pre-main-sequence stars with discs. Regions devoid of YSOs are self explanatory and contain no sources from the VISION YSOs catalogue. "Young" regions have at least one Class 0 source, implying it is still actively star forming. "Old" regions contain only Class I, Class II, Class III, and flat spectrum sources, implying at least a pre-main-sequence star has been formed. The resultant spatial distribution of the classified Voronoi tessellated ROI age classification is shown in Figure 3.3, where black regions are devoid of YSOs, red regions are "young", and blue regions are "old." For "old" regions, the YSOs may not have formed in-situ and are only seen in projection later in their lives. Thus, while we regard these regions as post-star formation because of the YSOs, they may also be pre-star formation.

In this section, we use Kendall's Tau and its corresponding p-value to measure the monotonic relationship between calculated molecular abundances and environmental properties and its statistical significance. Kendall's Tau, represented by τ, ranges from -1 to $+1$ or from perfectly negatively correlated to perfectly positively correlated. A Kendall's Tau of $\tau = 0$ implies that the data has no correlation (Kendall, 1948). For the purposes of the following discussion, a τ with $p < 0.05$ is considered statistically significant, $|\tau| \sim 0$ implies weak correlation, $|\tau| \sim 0.2$ implies moderate correlation, and $|\tau| \gtrsim 0.5$ implies strong correlation.

3.1 Line Widths

Figures 3.4 and 3.5 shows the measured line widths for C_2S and HC_5N as a function of NH_3 line widths for NGC 1333 and Orion A, respectively. NGC 1333 and Orion A have statistically significant ($p = 0.022$ and 0.002) strong correlation coefficients $\tau = 0.487$ and 0.356, respectively, between HC_5N and NH_3 line widths that imply that the gas components traced by HC_5N are likely spatially associated with the emitting

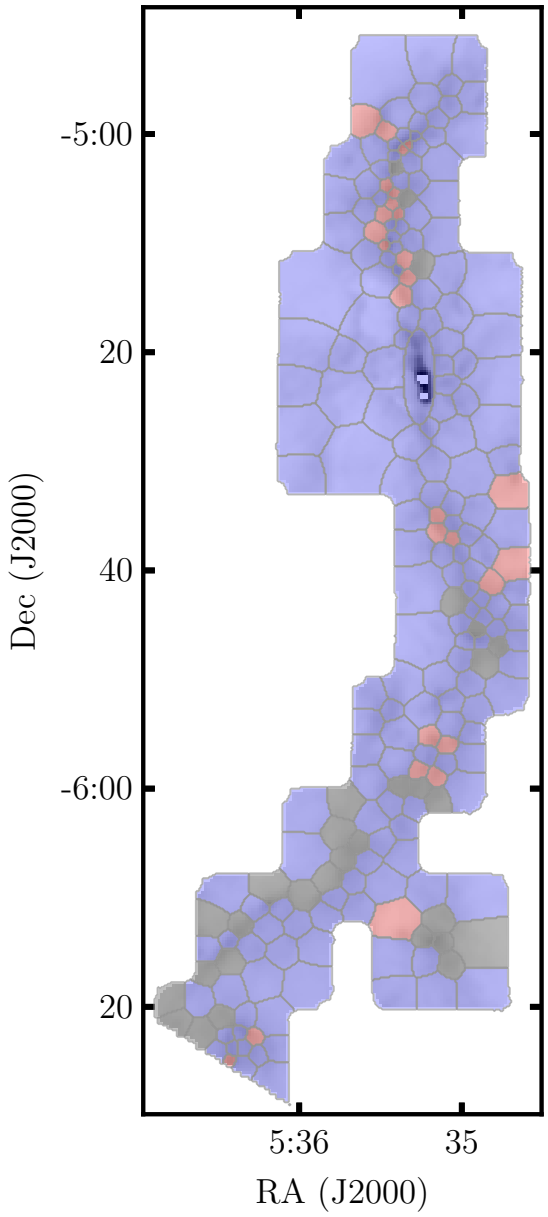

Figure 3.3: Orion A bin age classification map derived from the VISION YSO catalogue by Großschedl et al. (2019). Black: regions with no YSOs. Red: regions with at least one Class 0 YSO ("young"). Blue: regions with only protostars ("old"). The bin age classifications are overlaid on the H_2 column density map (km s^{-1}) (Singh et al., 2022).

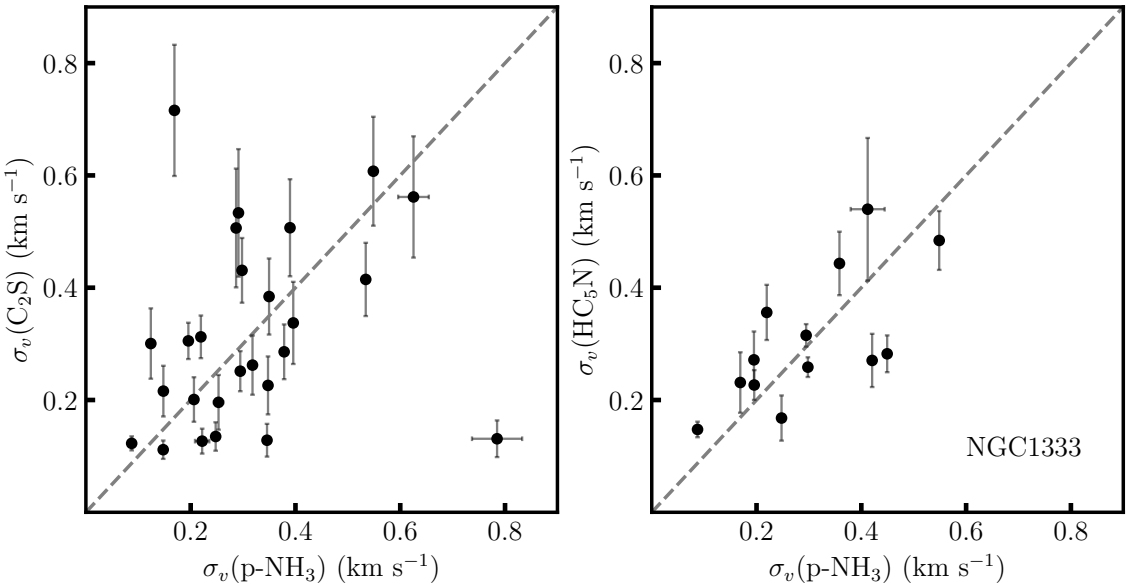

Figure 3.4: Measured C_2S and HC_5N line widths (σ_v) as a function of NH_3 line widths in km s^{-1} for NGC 1333, respectively.

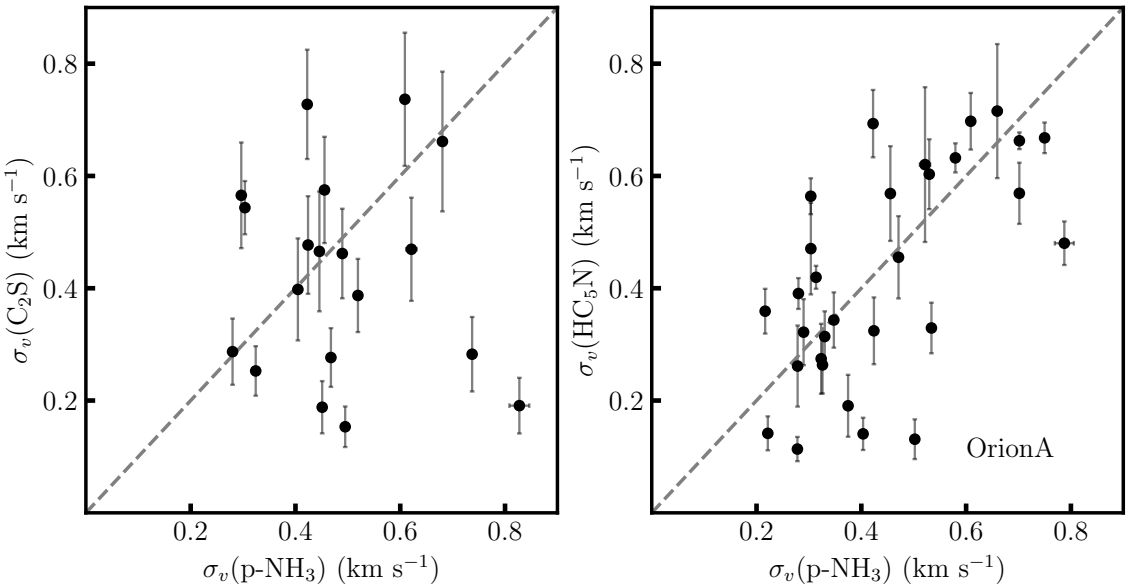

Figure 3.5: Same as Figure 3.4 but for Orion A.

NH_3 gas. The C_2S line widths show more variation with respect to NH_3 with a weaker statistically significant ($p = 0.004$) correlation coefficient of $\tau = 0.285$ in NGC 1333 and statistically insignificant ($p = 0.698$) and weak negative correlation coefficient $\tau = -0.0697$, implying that NH_3 emission may not be a good tracer for C_2S emission. Both conclusions above were also observed by Rathborne et al. (2008) for cores in the Pipe Nebula. Choudhury et al. (2020, 2021) observed broadening of NH_3 lines by multiple line components attributed to supersonic gas in L1688, possibly explaining our observation of high NH_3 line width components in both NGC 1333 and Orion A.

3.2 Rare Carbon Chains

3.2.1 HC_5N and C_2S

Figure 3.6 shows the relationship between $N(C_2S)$ and $N(HC_5N)$ in NGC 1333 and Orion A. NGC 1333 has a statistically significant ($p = 0.031$ strong positive correlation coefficient of $\tau = 0.643$ between RCC column densities. However, the strong correlation $\tau = 0.733$ in Orion A was not statistically significant $p = 0.056$ and may be attributed to the complexity of the Orion A region over that of NGC 1333. Each region has an average column density ratio of $N(C_2S)/N(HC_5N) \sim 5$ and ~ 3 for NGC 1333 and Orion A, respectively, which is similar to the ratio of ~ 2 reported by Suzuki et al. (1992). Dividing by the underlying $N(H_2)$, Figure 3.7 demonstrates the relationship between RCC abundances when the influence of density is removed. Neither NGC 1333 or Orion A demonstrate statistically significant ($p = 0.548$ and 0.056) correlation coefficients of $\tau = 0.214$ and 0.733, implying that RCC abundances are not correlated in the absence of density effects. The discordant abundance peaks between C_2S and HC_5N abundances over core evolution time due to different chemical life times in the cloud, modelled by Taniguchi et al. (2019), may lead to the lack of correlation between RCC abundances shown in Figure 3.7.

Using at the YSO data described above, the "old" and "young" regions show dif-

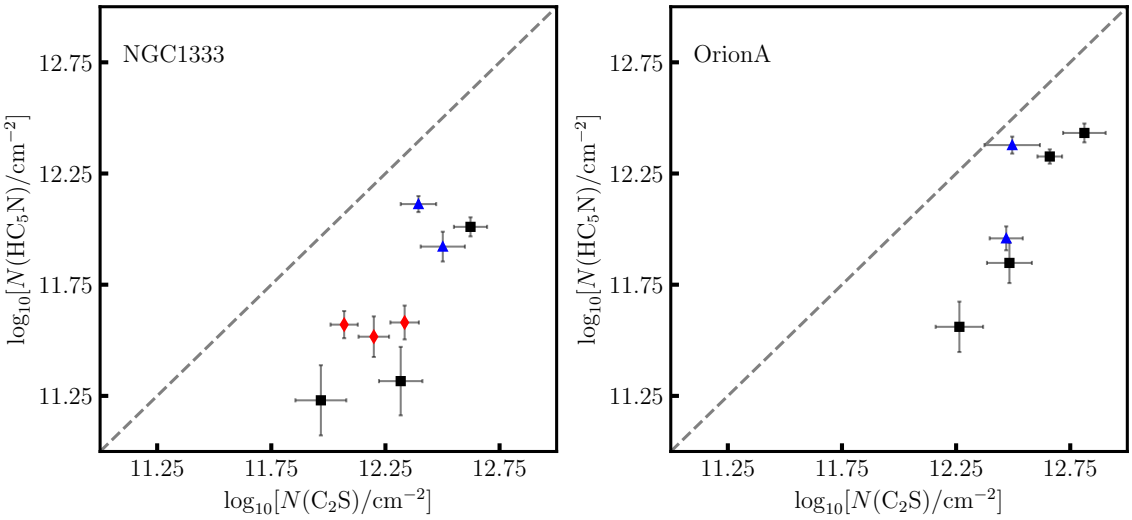

Figure 3.6: Measured $N(HC_5N)$ as a function of $N(C_2S)$ for NGC 1333 (left) and Orion A (right). Black squares are regions without YSOs ("young"). Red diamonds are regions with at least one Class 0 YSO ("young"). Blue diamonds are regions with only YSOs older than Class 0 ("old"). NGC 1333 does not have YSO information and plotted as black circles.

ferences in $N(C_2S)$ and $N(HC_5N)$. The "old" regions are on average more abundant in RCCs than the "young" regions, suggesting that RCC chemistry is enhanced near regions without active star formation. This may be a demonstration of radiation mediated Warm Carbon Chain Chemistry (WCCC) as modelled by Kalvāns (2021). NGC 1333 demonstrates similar enhancements in C_2S abundances, but with correspondingly less extreme values in $N(HC_5N)$. The difference in maximum HC_5N abundance between the two regions may suggest that sublimation into the gas-phase may be enhanced in the warmer Orion A GMC over that of the cooler NGC 1333 clump (Taniguchi et al., 2019).

3.2.2 RCCs and NH_3

Figure 3.8 shows the H_2 divided $N(C_2S)$ as a function of $N(NH_3)$ for NGC 1333 (left) and Orion A (right). Overall, NGC 1333 has larger spread in both C_2S and $N(NH_3)$ than Orion A. The "young" regions in Orion A tend be at the lower end of $N(C_2S)$, while "old" regions overlap with regions devoid of YSOs between $N(C_2S)/N(H_2) \sim$

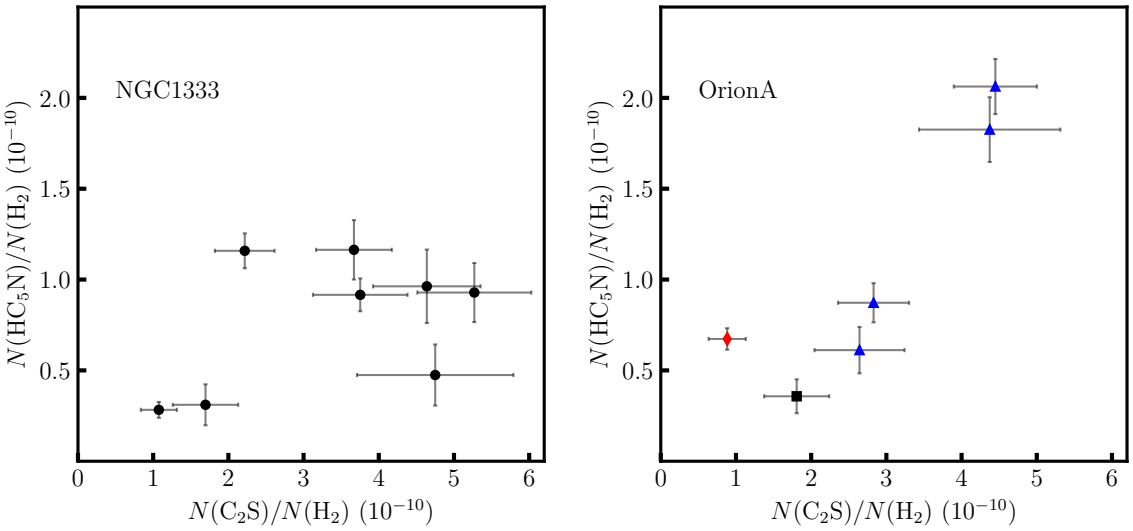

Figure 3.7: Measured HC_5N column density as a function of $N(C_2S)$ for NGC 1333 (left) and Orion A (right). H_2 is divided out of both RCCs to remove scatter due to local density effects. Symbols in the right plot are described in the caption of Figure 3.6.

$1\times10^{-10}-3\times10^{-10}$ and reach a maximum of $N(C_2S)/N(H_2) \sim 5\times10^{-10}$. The weak or lack of correlation between C_2S and NH_3, as demonstrated previously in Section 3.1, is again shown in Figure 3.8. Neither NGC 1333 or Orion A have statistically significant $p = 0.965$ and 0.455 correlation coefficients $\tau = -0.009$ and 0.124 between NH_3 and C_2S abundances, implying that C_2S and NH_3 formation processes likely do not take place under the same conditions.

Figure 3.9 shows the same relationship as Figure 3.8 but for HC_5N. For HC_5N we observe larger spread in RCC and $N(NH_3)$ in NGC 1333 than Orion A, contrary to Figure 3.8. However, this difference is likely due to the lack of HC_5N detections in NGC 1333 over that of Orion A. In NGC 1333, we observe one region with enhanced HC_5N at low $N(NH_3)$. In Orion A, we observe similar RCC column density behaviour, with "young" regions spreading out in $N(NH_3)$ at the lower end of $N(HC_5N)$ with $N(HC_5N)/N(H_2) < 1\times10^{-10}$. The "old" regions overlap with regions devoid of YSOs and "young" regions, reaching a maximum of $N(HC_5N)/N(H_2) \sim 3\times10^{-10}$. Overall, "old" regions have larger average RCC column densities than regions devoid of YSOs

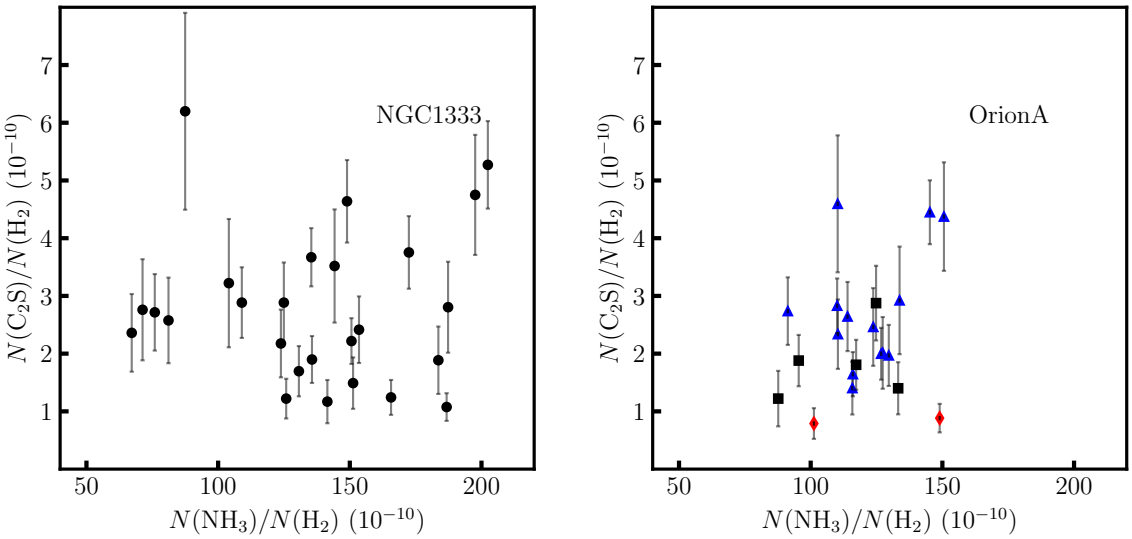

Figure 3.8: Measured $N(C_2S)$ as a function of $N(NH_3)$. Both $N(C_2S)$ and $N(NH_3)$ are scaled by $N(H_2)$. Symbols in the right plot are described in the caption of Figure 3.6.

and "young" regions. Neither NGC 1333 or Orion A have statistically significant ($p = 0.675$ and 0.134) correlation coefficients $\tau = -0.103$ and 0.175, respectively, between HC_5N and NH_3 column densities in Figure 3.9. Overall RCC abundances in both NGC 1333 and Orion A are not correlated with NH_3 abundances, suggesting different chemical environments may lead to the enhancement of RCC versus NH_3 column densities as previously suggested by Suzuki et al. (1992).

3.3 Dust Temperature

In this section, RCC and NH_3 column densities will be investigated with respect to dust temperature $T_{\rm dust}$ (K) as a proxy for the radiation field, as show in Figures 3.1 and 3.2. Figure 3.10 shows the abundance of C_2S as a function of $T_{\rm dust}$ (K) (Singh et al., 2022). In NGC 1333 and Orion A, $N(C_2S)$ is spread over a small range of dust temperatures, with an exception in Orion A. In Orion A, the "young" and "old" regions have different average $T_{\rm dust}$ values. The "young" regions have an average $T_{\rm dust}$ of $\sim$ 17 K and "old" regions have an average $T_{\rm dust}$ of $\sim$ 24 K. Regions devoid

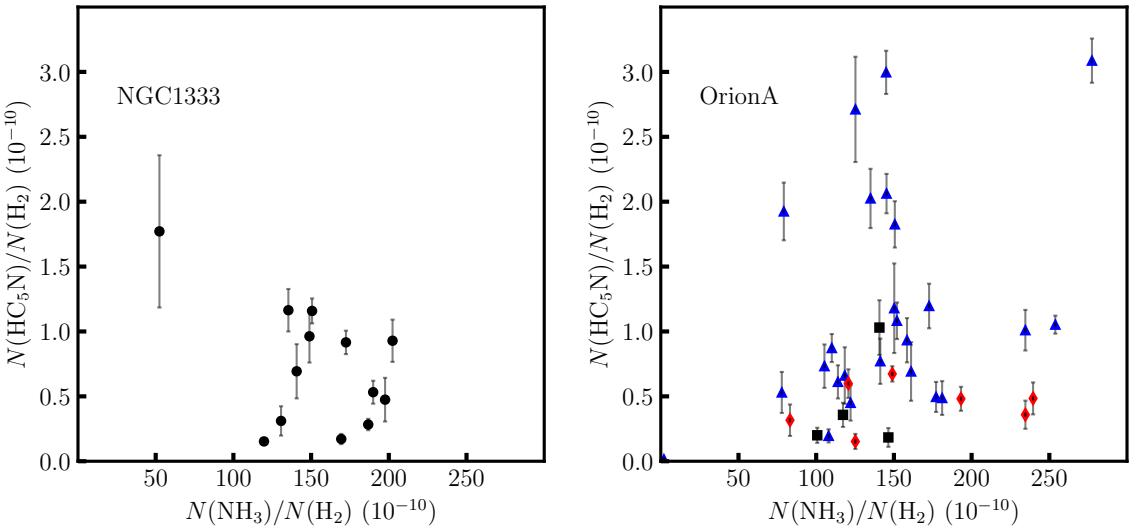

Figure 3.9: Measured $N(HC_5N)$ as a function of $N(NH_3)$. Both $N(HC_5N)$ and $N(NH_3)$ are scaled by $N(H_2)$. Symbols in the right plot are described in the caption of Figure 3.6.

of protostars have an intermediate average T_{dust} of $\sim$ 19 K. Therefore, the higher temperature conditions of "old" regions may lead to enhanced C_2S column densities. Despite the different average temperatures between the "young" and 'old" regions, neither NGC 1333 or Orion A show a statistically significant ($p = 0.570$ and 0.571) correlation between C_2S abundances and T_{dust} with correlation coefficients $\tau = 0.083$ and 0.095, respectively. Overall, the lack of correlation of $N(C_2S)$ with T_{dust} suggests that the radiation field does not measurably impact the efficiency of C_2S production.

Figure 3.11 shows the fractional abundance of HC_5N as a function of T_{dust} in NGC 1333 (left) and Orion A (right) (Singh et al., 2022). Like Figure 3.10, $N(HC_5N)$ is spread over a small range of T_{dust} for NGC 13333 and Orion A is similarly spread out over a larger range of T_{dust}. Again, the HC_5N column densities for regions devoid of YSOs, "young" regions, and "old" regions have different average dust temperatures. The "young" regions have an average T_{dust} of $\sim$ 24 K and the "old" regions have an average T_{dust} of $\sim$ 34 K, while regions devoid of YSOs have average dust temperatures smaller then both at $\sim$ 20 K. Similar to NGC 1333, the "old" regions

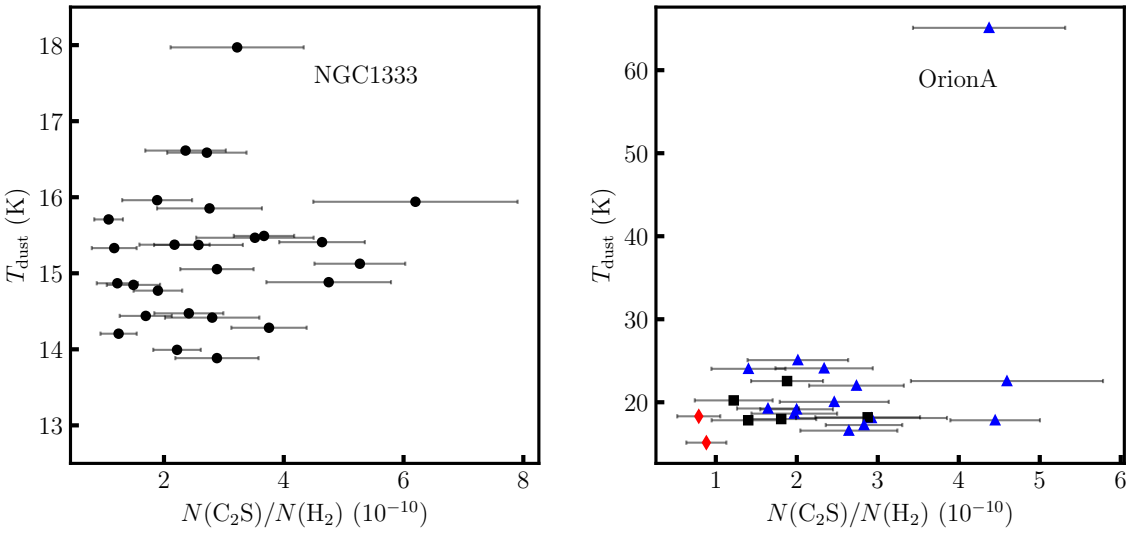

Figure 3.10: $T_{\rm dust}$ from Singh et al. (2022) as a function of $N(C_2S)/N(H_2)$. Symbols in the right plot are described in the caption of Figure 3.6.

with larger dust temperatures and a correspondingly stronger radiation field experience enhanced HC_5N column densities. On average, colder and correspondingly less irradiated regions have less HC_5N, suggesting temperature and radiation play a role in HC_5N generation. Like Figure 3.10, NGC 1333 does not show a statistically significant $p = 0.674$ correlation coefficient $\tau = 0.103$ between HC_5N abundances and $T_{\rm dust}$. However, Orion A has a statistically significant $p = 0.047$ moderate positive correlation $\tau = 0.232$ between HC_5N abundances and $T_{\rm dust}$, suggesting that radiation field strength and HC_5N production may be linked.

Like Figures 3.10 and 3.11, Figure 3.12 shows the abundance of NH_3 as a function of $T_{\rm dust}$ in NGC 1333 (left) and Orion A (middle) (Singh et al., 2022). In NGC 1333, $N(NH_3)$ is negatively correlated with $T_{\rm dust}$, with $N(NH_3)$ increasing with decreasing temperature as shown by the statistically significant ($p = 1.65 \times 10^{-9}$) correlation coefficient $\tau = -0.450$. As discussed in Section 1.2.2, the NH_3 formation rate in low temperature gas is enhanced in the gas-phase and on the surface of dust grains. The negative correlation in Figure 3.12 suggests that NH_3 formation is enhanced with decreasing radiation strength. $T_{\rm dust}$ in Orion A reaches higher temperatures than

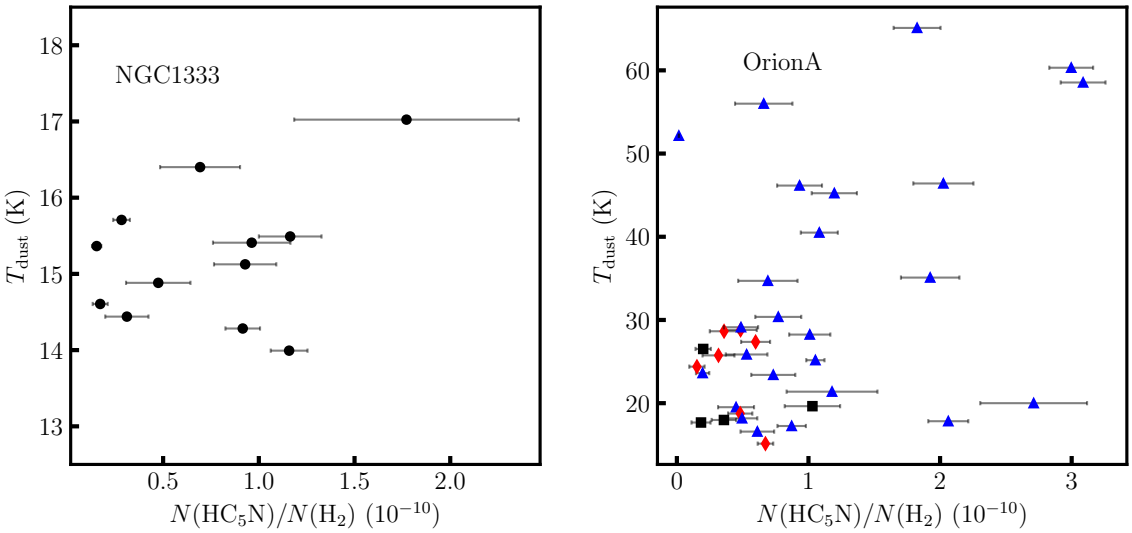

Figure 3.11: $T_{\rm dust}$ from Singh et al. (2022) as a function of $N(\rm HC_5N)/N(\rm H_2)$. Symbols in the right plot are described in the caption of Figure 3.6.

NGC 1333. The "old" regions are found across the $T_{\rm dust}$ temperature and $N(\rm HC_5N)$ ranges, while regions devoid of YSOs and "young" regions are largely found in the lower half of dust temperatures, as seen in Figure 3.11. Here, "old" regions appear at average $T_{\rm dust}$ of $\sim$ 29 K, "young" regions at $\sim$ 24, and regions devoid of YSOs at $\sim$ 20 K. A weak negative correlation between $T_{\rm dust}$ and $N(\rm NH_3)$ is observed in the right plot of Figure 3.12, as shown by the statistically significant ($p = 0.0004$) correlation coefficient $\tau = -0.156$. Overall, we observe increasing $\rm NH_3$ abundances with decreasing radiation field strength in both NGC 1333 and Orion A.

3.4 Chemical Abundance Ratios as Possible Chemical Clocks

Suzuki et al. (1992) contains the first suggestion of the $N(\rm NH_3)/N(\rm C_2S)$ abundance ratio was an indicator of evolutionary stage in star forming regions. The ratio was originally applied to star forming cores, by Suzuki et al. (1992) and subsequently by Hirota et al. (2009), Marka et al. (2012), and Ohashi et al. (2014). Hirota et al. (2009) defined a tentative cut off of $N(\rm NH_3)/N(\rm C_2S) < 10$ for carbon chain producing

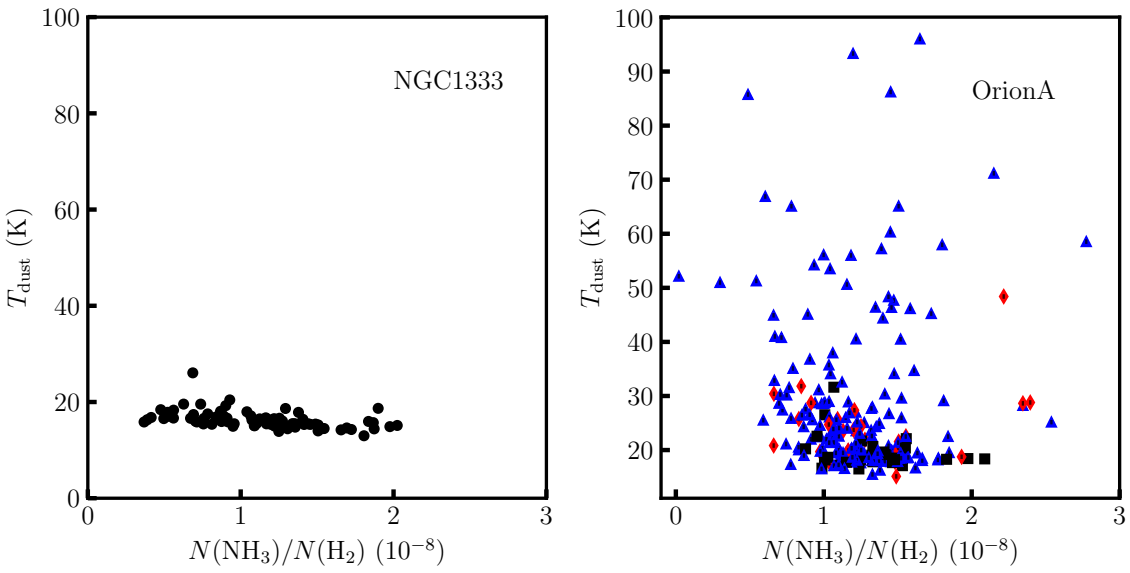

Figure 3.12: $T_{\rm dust}$ from Singh et al. (2022) as a function of $N(NH_3)$ divided by $N(H_2)$ for NGC 1333 (left) and Orion A (middle). Symbols in the right plots are described in the caption of Figure 3.6.

regions. In general, the $N(NH_3)/N(C_2S)$ ratio is expected to be enhanced during star formation due to the nature of NH_3 as a late-stage molecules. Conversely, the $N(NH_3)/N(C_2S)$ ratio is assumed to be depleted before the onset of star formation due to RCCs as early-stage molecules, as discussed in Section 1.2. However, Taniguchi et al. (2019) and Kalvāns (2021) provided models that describe the formation of RCCs around YSOs under WCCC, leading to possible enhancements of RCC column densities during star formation.

Figure 3.13 shows the relationship between the ratio $N(NH_3)/N(C_2S)$ and $N(C_2S)/N(H_2)$, as first plotted by Hirota et al. (2009) to classify carbon chain producing regions. The vertical grey-dashed line in the left and right plots associated with NGC 1333 and Orion A, respectively, mark the $N(NH_3)/N(C_2S) < 10$ limit for a region to be classified as a carbon chain producing region by Hirota et al. (2009). Neither NGC 1333 or Orion A contain any carbon chain producing regions under this classification. The lack of carbon chain producing regions in these targets was also observed by Hirota et al. (2009). Note that the apparent correlation in the data is driven at least in part

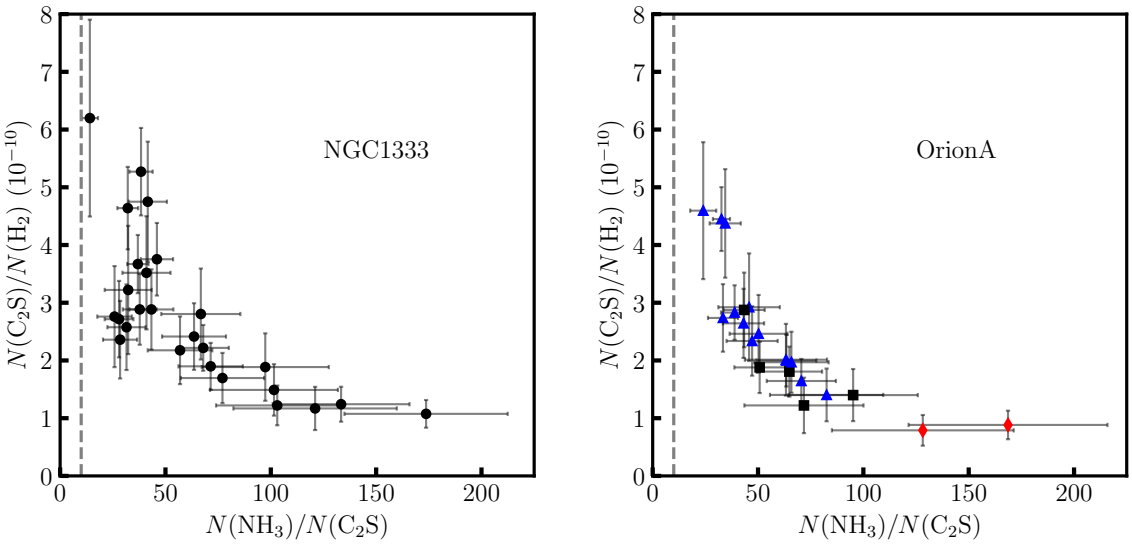

Figure 3.13: Measured $N(C_2S)$ as a function of the $N(NH_3)/N(C_2S)$ ratio. The vertical grey-dashed line represents the $N(NH_3)/N(C_2S) < 10$ boundary for carbon chain producing regions suggested by Hirota et al. (2009). Symbols in the right plot are described in the caption of Figure 3.6.

by the correlated nature of the axes and the near constant fractional abundance of NH_3, so we are mainly concerned about the behaviour of $N(NH_3)/N(C_2S)$ in Figure 3.13.

According to Figure 3.13, NH_3 is most abundant in "young" regions with embedded protostars with $N(NH_3)/N(C_2S) > 100$, while regions devoid of YSOs have $N(NH_3)/N(C_2S) < 100$, as observed by Suzuki et al. (1992) in cores. Expanding upon Suzuki et al. (1992), we include "old" regions with embedded and unembedded protostars. Many chemical models, including that of Suzuki et al. (1992) and Marka et al. (2012), suggest that the $N(NH_3)/N(C_2S)$ ratio should increase over time. However, our observed "old" regions have significant overlap with the regions devoid of YSOs, all of which have $N(NH_3)/N(C_2S) < 100$. If the YSOs classifying the regions are not associated with the gas and the region is in fact pre-star forming, our observations do not test the models suggested by Suzuki et al. (1992); Marka et al. (2012). Marka et al. (2012) also observed isolated cores at different stages star formation, including Class 0 and I sources. Similar to Marka et al. (2012) we observe

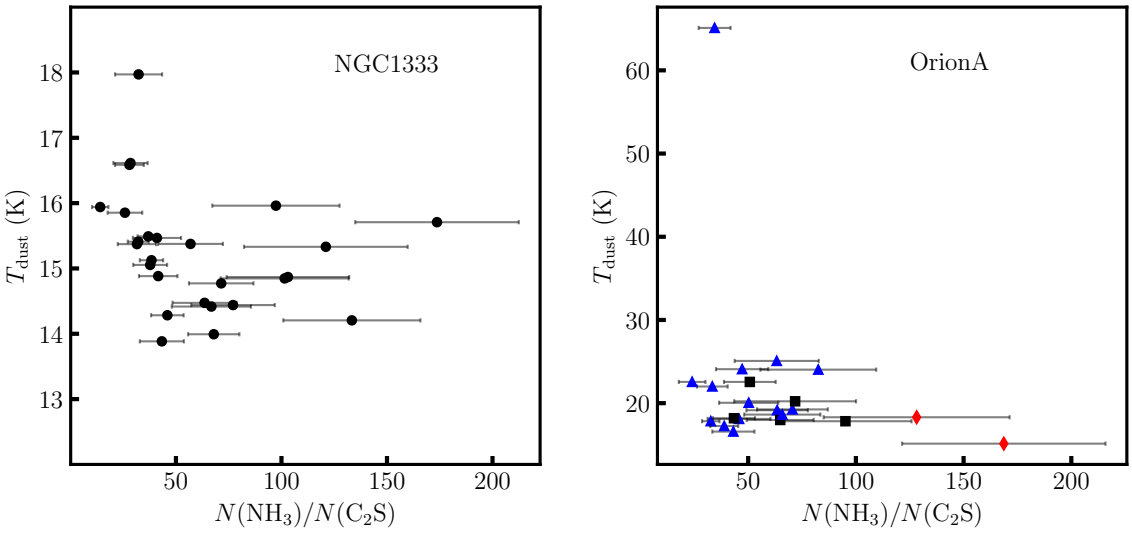

Figure 3.14: $T_{\rm dust}$ from Singh et al. (2022) as a function of the $N(NH_3)/N(C_2S)$ column density ratio for NGC 1333 (left) and Orion A (right). Symbols in the right plot are described in the caption of Figure 3.6.

regions with Class 0 sources ("young") to have $N(NH_3)/N(C_2S) > 100$ and regions with Class I YSOs (part of the "old" category) to have $N(NH_3)/N(C_2S) < 100$. Like Marka et al. (2012), we observe similar chemical compositions in the youngest and oldest gas according to YSO classification, leading to the suggestion the "old" regions may in fact be pre-star forming.

The $N(NH_3)/N(C_2S)$ ratio as a chemical clock can further be investigated according to the environmental conditions of the gas, including the $T_{\rm dust}$ as a proxy for the radiation field (Singh et al., 2022). Chemical models used in previous chemical clock studies are UV radiation shielded. Recent models by Taniguchi et al. (2019) and Kalvāns (2021) fold in irradiation in addition to WCCC and are able to better predict the increase in RCC abundances in the later stages of star formation. Figure 3.14 demonstrates that $N(NH_3)/N(C_2S)$ ratio has a negative correlation with $T_{\rm dust}$ in NGC 1333, as shown by the statistically significant ($p = 0.01$) correlation coefficient -0.354. On the other hand, the $N(NH_3)/N(C_2S)$ ratio does not have a statistically significant correlation ($p = 0.531$ and $\tau = -0.105$) with $T_{\rm dust}$ in Orion A. The $N(NH_3)/N(C_2S)$ ratio may correlated by $T_{\rm dust}$ in NGC 1333 and not Orion

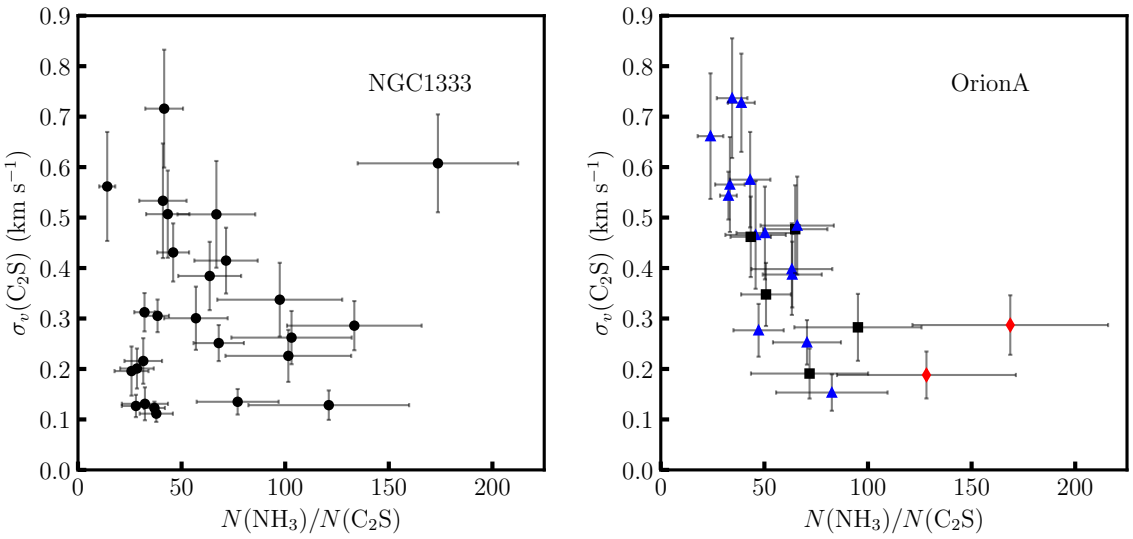

Figure 3.15: Measured $\sigma_v(C_2S)$ (km s^{-1}) as a function of the $N(NH_3)/N(C_2S)$ ratio in NGC 1333 (left) and Orion A (right). Symbols in the right plot are described in the caption of Figure 3.6.

A because NGC 1333 is a simpler region, making the impact of $T_{\rm dust}$ easier to isolate. Due to the lack of correlation between C_2S abundances and $T_{\rm dust}$ in Figure 3.10, the correlation of the ratio $N(NH_3)/N(C_2S)$ in NGC 1333 is likely as a result of the negative correlation of NH_3 abundances in Figure 3.12.

Finally, Figure 3.15 shows that $\sigma_v(C_2S)$ increases with decreasing $N(NH_3)/N(C_2S)$ in Orion A, implying that the $N(NH_3)/N(C_2S)$ ratio is deficient towards more active gas in regions devoid of YSOs and "old" regions. This is demonstrated by the statistically significant $p = 0.0001$ correlation coefficient $\tau = -0.581$. A similar phenomena is found for the $N(NH_3)/N(HC_5N)$ ratio in Figure 3.16, but with more overlap with "young" regions ($p = -5.37 \times 10^{-7}$ and $\tau = -0.584$). The negative correlation between RCC line width and the column density ratios are also observed by Ohashi et al. (2014). On the other hand, NGC 1333 does not show any obvious correlation between RCC line width and $N(NH_3)/N(C_2S)$ or $N(NH_3)/N(HC_5N)$ ratios in the left plots of Figure 3.15 ($p = 0.570$ and $\tau = 0.083$) and Figure 3.16 ($p = 0.765$ and $\tau = -0.077$).

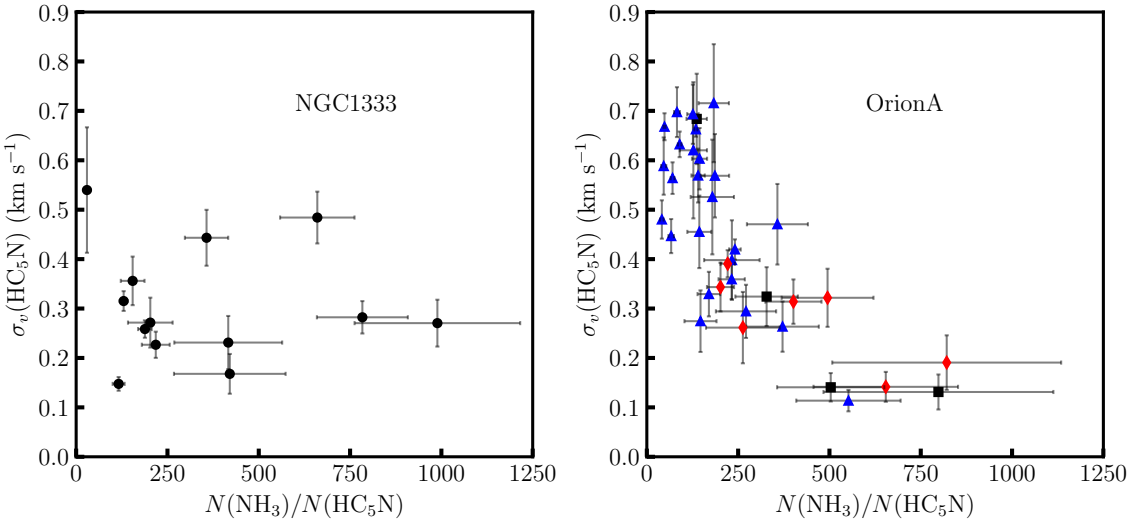

Figure 3.16: Measured $\sigma_v(HC_5N)$ (km s^{-1}) as a function of the $N(NH_3)/N(HC_5N)$ ratio in NGC 1333 (left) and Orion A (right). Symbols in the right plot are described in the caption of Figure 3.6.

Chapter 4

Conclusions and Summary

In this thesis, we calculated RCC and NH_3 fractional abundances in the low-mass star forming region NGC 1333 and the high-mass star forming region Orion A, accessing a range of densities, radiation field strengths, and region ages as defined by young stellar object counts. The star forming regions were spatially binned according to the underlying H_2 column density in regions-of-interest large enough to increase the signal-to-noise ratio and small enough to contain environmentally related gas, as described in Chapter 2. The resulting stacked RCC and NH_3 spectra from each bin and their corresponding molecular abundances were used to test the open questions in Section 1.7. Our conclusions to these questions, as discussed in Chapter 3, are as follows:

1. In Section 3.2.1, we tested whether or not RCC emission is spatially correlated by comparing their fractional abundances per bin. We found that C_2S and HC_5N molecular abundances are correlated in NGC 1333 and Orion A, confirming the original observation made by Suzuki et al. (1992).

2. In Section 3.1, we tested whether or not RCC and NH_3 emission is spatially related by comparing their line widths, as derived from the NH_3 and RCC spectra fits. In general, C_2S line widths showed larger scatter with respect to NH_3 than HC_5N. Assuming that line widths are indicator of the activity of the gas and that gas with the same line widths should be spatially related,

we confirm the lack of spatial correlation between C_2S and NH_3 observed by Suzuki et al. (1992). This conclusion is furthered by the lack of correlation in both NGC 1333 and Orion A between RCC and NH_3 abundances discussed in Section 3.2.2.

3. In Section 3.3, we tested the hypothesis modelled by Taniguchi et al. (2019); Kalvāns (2021) that RCC production is correlated with the interstellar radiation field proxied by dust temperature. For C_2S, we found that "young" regions on average had a lower dust temperature than "old" regions and regions devoid of young stellar objects in Orion A. For HC_5N we saw similar behaviour, in which the fractional abundances in "young" regions and regions devoid of young stellar objects have lower dust temperatures than "old" regions in Orion A. Overall, both C_2S and HC_5N fractional abundances are higher in the more highly irradiated regions (higher dust temperature), suggesting RCC formation may be enhanced by the presence of a radiation field.

4. In Section 3.3, we explored the scenario modelled by von Procházka and Millar (2021) that NH_3 gas-phase abundances are complicated by gas-phase synthesis and grain-gas cycling with the inclusion of a H_2 desorption by a radiation field. In NGC 1333, we found that NH_3 fractional abundances are negatively correlated in for $13 - 18$ K dust temperatures, suggesting that NH_3 synthesis is enhanced with decreasing radiation strength. This is concurrent with the understanding of NH_3 as a late stage species. In Orion A, we observe the a weak negative correlation but with more scatter at higher dust temperatures. Therefore, we confirm that NH_3 synthesis may be more complicated than its original definition as a late-stage species, although this observation may be due to Orion A being a more complicated region.

5. In Section 3.4, we tested the NH_3/C_2S fractional abundance ratio as a chemical clock in Orion A as first suggested by Suzuki et al. (1992). We observe that

that NH_3/C_2S is enhanced in "young" regions and deficient in "old" regions and regions devoid of young stellar objects, adding evidence supporting the chemical clock suggested by Suzuki et al. (1992).

Overall, we were able to test a variety of chemical abundance hypotheses across a range of star forming environments using the GAS (Friesen et al., 2017). In future work, we will extend our analysis to include the remaining star forming regions in GAS, including star forming clumps in the Taurus and Ophiuchus MCs. In addition, this analysis will be performed on the KFPA Examinations of Young STellar Object Natal Environments (KEYSTONE) survey that include more molecular tracers, like methanol (CH_3OH) and H_2O, in addition to the molecules investigated here (Keown et al., 2019). Young Stellar Object analysis will be performed using the Spitzer Extended Solar Neighborhood Archive (SESNA) to classify the regions in NGC 1333 and Orion A (Gutermuth et al., 2022). This will extend the chemical clock analyses to the low-mass star forming region NGC 1333, giving a fuller picture to the viability of the NH_3/C_2S chemical clock across a range of star forming conditions. The NGC 1333 and Orion A analyses will appear in Pettyjohn et al. (2021).

BIBLIOGRAPHY

R. K. Friesen, J. E. Pineda, co-PIs, E. Rosolowsky, F. Alves, A. Chacón-Tanarro, H. How-Huan Chen, M. Chun-Yuan Chen, J. Di Francesco, J. Keown, H. Kirk, A. Punanova, Y. Seo, Y. Shirley, A. Ginsburg, C. Hall, S. S. R. Offner, A. Singh, H. G. Arce, P. Caselli, A. A. Goodman, P. G. Martin, C. Matzner, P. C. Myers, E. Redaelli, and GAS Collaboration, "The green bank ammonia survey: First results of NH_3 mapping of the gould belt," *ApJ*, vol. 843, no. 1, p. 63, Jul. 2017.

H. Suzuki, S. Yamamoto, M. Ohishi, N. Kaifu, S.-I. Ishikawa, Y. Hirahara, and S. Takano, "A survey of CCS, HC_3N, HC_5N, and NH_3 toward dark cloud cores and their production chemistry," *ApJ*, vol. 392, p. 551, Jun. 1992.

M. Pettyjohn *et al.*, "Abundance Variation of Dense Gas Tracers in the Gould Belt," 2021, in prep.

M. Cappellari and Y. Copin, "Adaptive spatial binning of integral-field spectroscopic data using Voronoi tessellations," *MNRAS*, vol. 342, no. 2, pp. 345–354, 06 2003.

A. Ginsburg and J. Mirocha, "PySpecKit: Python Spectroscopic Toolkit," p. ascl:1109.001, Sep. 2011.

J. G. Mangum and Y. L. Shirley, "How to Calculate Molecular Column Density," *PASP*, vol. 127, no. 949, p. 266, Mar. 2015.

H. S. P. Müller, S. Thorwirth, D. A. Roth, and G. Winnewisser, "The Cologne Database for Molecular Spectroscopy, CDMS," *A&A*, vol. 370, pp. L49–L52, Apr. 2001.

H. S. P. Müller, F. Schlöder, J. Stutzki, and G. Winnewisser, "The Cologne Database for Molecular Spectroscopy, CDMS: a useful tool for astronomers and spectroscopists," *J. Mol. Struct.*, vol. 742, no. 1-3, pp. 215–227, May 2005.

COMPLETE team, "FCRAO Perseus 12CO cubes and map," 2011.

——, "FCRAO Perseus 13CO cubes and map," 2011.

A. Singh *et al.*, "Herschel H2 Column Density Maps," 2022, in prep.

S. Kong, H. G. Arce, J. R. Feddersen, J. M. Carpenter, F. Nakamura, Y. Shimajiri, A. Isella, V. Ossenkopf-Okada, A. I. Sargent, Á. Sánchez-Monge, S. T. Suri, J. Kauffmann, T. Pillai, J. E. Pineda, J. Koda, J. Bally, D. C. Lis, P. Padoan, R. Klessen, S. Mairs, A. Goodman, P. Goldsmith, P. McGehee, P. Schilke, P. J. Teuben, M. J. Maureira, C. Hara, A. Ginsburg, B. Burkhart, R. J. Smith, A. Schmiedeke, J. L. Pineda, S. Ishii, K. Sasaki, R. Kawabe, Y. Urasawa, S. Oyamada, and Y. Tanabe, "The CARMA-NRO Orion Survey," *ApJS*, vol. 236, no. 2, p. 25, Jun. 2018.

J. E. Großschedl, J. Alves, P. S. Teixeira, H. Bouy, J. Forbrich, C. J. Lada, S. Meingast, Á. Hacar, J. Ascenso, C. Ackerl, B. Hasenberger, R. Köhler, K. Kubiak, I. Larreina, L. Linhardt, M. Lombardi, and T. Möller, "Vision - vienna survey in orion. iii. young stellar objects in orion a," *A&A*, vol. 622, p. A149, Feb. 2019.

T. Hirota, M. Ohishi, and S. Yamamoto, "A search for carbon-chain-rich cores in dark clouds," *ApJ*, vol. 699, no. 1, pp. 585–602, Jul. 2009.

P. Swings and L. Rosenfeld, "Considerations Regarding Interstellar Molecules," *ApJ*, vol. 86, pp. 483–486, Nov. 1937.

J. Dunham, T., "Interstellar Neutral Potassium and Neutral Calcium," *PASP*, vol. 49, no. 287, pp. 26–28, Feb. 1937.

A. McKellar, "Evidence for the Molecular Origin of Some Hitherto Unidentified Interstellar Lines," *PASP*, vol. 52, no. 307, p. 187, Jun. 1940.

E. A. Bergin and M. Tafalla, "Cold Dark Clouds: The Initial Conditions for Star Formation," *ARA&A*, vol. 45, no. 1, pp. 339–396, Sep. 2007.

M. Chevance, J. M. D. Kruijssen, E. Vazquez-Semadeni, F. Nakamura, R. Klessen, J. Ballesteros-Paredes, S.-i. Inutsuka, A. Adamo, and P. Hennebelle, "The Molecular Cloud Lifecycle," *Space Sci. Rev.*, vol. 216, no. 4, p. 50, Apr. 2020.

P. Girichidis, S. S. R. Offner, A. G. Kritsuk, R. S. Klessen, P. Hennebelle, J. M. D. Kruijssen, M. G. H. Krause, S. C. O. Glover, and M. Padovani, "Physical Processes in Star Formation," *Space Sci. Rev.*, vol. 216, no. 4, p. 68, Jun. 2020.

J. Ballesteros-Paredes, P. André, P. Hennebelle, R. S. Klessen, J. M. D. Kruijssen, M. Chevance, F. Nakamura, A. Adamo, and E. Vázquez-Semadeni, "From Diffuse Gas to Dense Molecular Cloud Cores," *Space Sci. Rev.*, vol. 216, no. 5, p. 76, Jun. 2020.

R. C. Kennicutt and N. J. Evans, "Star Formation in the Milky Way and Nearby Galaxies," *ARA&A*, vol. 50, pp. 531–608, Sep. 2012.

K. I. Öberg and E. A. Bergin, "Astrochemistry and compositions of planetary systems," *Phys. Rep.*, vol. 893, pp. 1–48, Jan. 2021.

E. F. van Dishoeck and G. A. Blake, "Chemical Evolution of Star-Forming Regions," *ARA&A*, vol. 36, pp. 317–368, Jan. 1998.

N. Sakai, T. Sakai, T. Hirota, and S. Yamamoto, "Abundant carbon-chain molecules toward the low-mass protostar iras 04368+2557 in l1527," *ApJ*, vol. 672, no. 1, pp. 371–381, Jan. 2008.

B. T. Draine, *Physics of the Interstellar and Intergalactic Medium.* NJ: Princeton University Press, 2011.

V. Wakelam, E. Bron, S. Cazaux, F. Dulieu, C. Gry, P. Guillard, E. Habart, L. Hornekær, S. Morisset, G. Nyman, V. Pirronello, S. D. Price, V. Valdivia, G. Vidali, and N. Watanabe, "H_2 formation on interstellar dust grains: The viewpoints of theory, experiments, models and observations," *Mol. Astrophys.*, vol. 9, pp. 1–36, Dec. 2017.

S. Kwok, *Physics and Chemistry of the Interstellar Medium.* USA: University Science Books, 2007.

G. B. I. Scott, C. G. Freeman, and M. J. McEwan, "The interstellar synthesis of ammonia," *MNRAS*, vol. 290, no. 4, pp. 636–638, Oct. 1997.

S. Rednyk, Š. Roučka, A. Kovalenko, T. D. Tran, P. Dohnal, R. Plašil, and J. Glosík, "Reaction of NH^+, $NH_2{}^+$, and $NH_3{}^+$ ions with H_2 at low temperatures. The pathway to ammonia production in the interstellar medium," *A&A*, vol. 625, p. A74, May 2019.

J. C. Laas and P. Caselli, "Modeling sulfur depletion in interstellar clouds," *A&A*, vol. 624, p. A108, Apr. 2019.

K. Taniguchi, H. Ozeki, M. Saito, N. Sakai, F. Nakamura, S. Kameno, S. Takano, and S. Yamamoto, "Implication of Formation Mechanisms of HC_5N in TMC-1 as Studied by ^{13}C Isotopic Fractionation," *ApJ*, vol. 817, no. 2, p. 147, Feb. 2016.

A. M. Burkhardt, E. Herbst, S. V. Kalenskii, M. C. McCarthy, A. J. Remijan, and B. A. McGuire, "Detection of HC_5N and HC_7N Isotopologues in TMC-1 with the Green Bank Telescope," *MNRAS*, vol. 474, no. 4, pp. 5068–5075, Mar. 2018.

K. Taniguchi, E. Herbst, P. Caselli, A. Paulive, D. M. Maffucci, and M. Saito, "Cyanopolyyne chemistry around massive young stellar objects," *ApJ*, vol. 881, no. 1, p. 57, Aug. 2019.

A. G. G. M. Tielens, *The Physics and Chemistry of the Interstellar Medium.* NY: Cambridge University Press, 2005.

A. C. A. Boogert, P. A. Gerakines, and D. C. B. Whittet, "Observations of the icy universe." *ARA&A*, vol. 53, pp. 541–581, Aug. 2015.

P. Ehrenfreund and S. B. Charnley, "Organic Molecules in the Interstellar Medium, Comets, and Meteorites: A Voyage from Dark Clouds to the Early Earth," *ARA&A*, vol. 38, pp. 427–483, Jan. 2000.

Y. Hirahara, H. Suzuki, S. Yamamoto, K. Kawaguchi, N. Kaifu, M. Ohishi, S. Takano, S.-I. Ishikawa, and A. Masuda, "Mapping Observations of Sulfur-containing Carbon-Chain Molecules in Taurus Molecular Cloud 1 (TMC-1)," *ApJ*, vol. 394, p. 539, Aug. 1992.

J. M. Rathborne, C. J. Lada, A. A. Muench, J. F. Alves, and M. Lombardi, "The nature of the dense core population in the pipe nebula: A survey of NH_3, CCS, and HC_5N molecular line emission," *ApJS*, vol. 174, no. 2, pp. 396–425, Feb. 2008.

J. B. Foster, E. W. Rosolowsky, J. Kauffmann, J. E. Pineda, M. A. Borkin, P. Caselli, P. C. Myers, and A. A. Goodman, "Dense cores in perseus: The influence of stellar content and cluster environment," *ApJ*, vol. 696, no. 1, pp. 298–319, May 2009.

S. Ohashi, K. Tatematsu, M. Choi, M. Kang, T. Umemoto, J.-E. Lee, T. Hirota, S. Yamamoto, and N. Mizuno, "Chemical variation in molecular cloud cores in the orion a cloud. iii," *PASJ*, vol. 66, no. 6, 12 2014, 119.

C. Marka, K. Schreyer, R. Launhardt, D. A. Semenov, and T. Henning, "Tracing the evolutionary stage of bok globules: Ccs and nh3," *A&A*, vol. 537, p. A4, 2012.

T. Suzuki, M. Ohishi, and T. Hirota, "Distribution of CCS and HC_3N in L1147, an Early Phase Dark Cloud," *ApJ*, vol. 788, no. 2, p. 108, Jun. 2014.

Y. M. Seo, L. Majumdar, P. F. Goldsmith, Y. L. Shirley, K. Willacy, D. Ward-Thompson, R. Friesen, D. Frayer, S. E. Church, D. Chung, K. Cleary, N. Cunningham, K. Devaraj, D. Egan, T. Gaier, R. Gawande, J. O. Gundersen, A. I. Harris, P. Kangaslahti, A. C. S. Readhead, L. Samoska, M. Sieth, M. Stennes, P. Voll, and S. White, "An ammonia spectral map of the l1495-b218 filaments in the taurus molecular cloud. ii. CCS and HC_7N chemistry and three modes of star formation in the filaments," *ApJ*, vol. 871, no. 2, p. 134, Feb. 2019.

N. Sakai and S. Yamamoto, "Warm Carbon-Chain Chemistry," *Chem. Rev.*, vol. 113, no. 12, pp. 8981–9015, Dec. 2013.

S. Spezzano, L. Bizzocchi, P. Caselli, J. Harju, and S. Brünken, "Chemical differentiation in a prestellar core traces non-uniform illumination," *A&A*, vol. 592, p. L11, Aug. 2016.

J. Kalvāns, "The connection between warm carbon-chain chemistry and interstellar irradiation of star-forming cores," *ApJ*, vol. 910, no. 1, p. 54, Mar. 2021.

A. A. von Procházka and T. J. Millar, "Species cycling and the enhancement of ammonia in prestellar cores," *MNRAS*, vol. 501, no. 1, pp. 1228–1242, Feb. 2021.

W. Demtröder, *Molecular Physics: Theoretical Principles and Experimental Methods*. Weinheim: WILEY-VCH Verlag GmbH & Co. KGaA, 2005.

P. F. Bernath, *Spectra of Atoms and Molecules*. NY: Oxford University Press, 2016.

P. T. P. Ho and C. H. Townes, "Interstellar ammonia," *ARA&A*, vol. 21, pp. 239–270, Jan. 1983.

S. Wang, Z. Ren, D. Li, J. Kauffmann, Q. Zhang, and H. Shi, "Hyperfine group ratio: a recipe for deriving kinetic temperature from the ammonia inversion lines," *MNRAS*, vol. 499, no. 3, pp. 4432–4444, Dec. 2020.

G. B. Rybicki and A. P. Lightman, *Radiative Processes in Astrophysics*. Wienheim: WILEY-VCH Verlag GmbH & Co. KGaA, 2004.

T. L. Wilson, K. Rohlfs, and S. Hüttemeister, *Tools of Radio Astronomy*, 3rd ed. Germany: Springer, 2000.

R. M. Prestage, "The Green Bank Telescope," in *Society of Photo-Optical Instrumentation Engineers (SPIE) Conference Series*, ser. Society of Photo-Optical Instrumentation Engineers (SPIE) Conference Series, L. M. Stepp, Ed., vol. 6267, Jun. 2006, p. 626712.

C. Zucker, E. F. Schlafly, J. S. Speagle, G. M. Green, S. K. N. Portillo, D. P. Finkbeiner, and A. A. Goodman, "Mapping Distances across the Perseus Molecular Cloud Using CO Observations, Stellar Photometry, and Gaia DR2 Parallax Measurements," *ApJ*, vol. 869, no. 1, p. 83, Dec. 2018.

J. E. Großschedl, J. Alves, S. Meingast, C. Ackerl, J. Ascenso, H. Bouy, A. Burkert, J. Forbrich, V. Fürnkranz, A. Goodman, Á. Hacar, G. Herbst-Kiss, C. J. Lada, I. Larreina, K. Leschinski, M. Lombardi, A. Moitinho, D. Mortimer, and E. Zari, "3D shape of Orion A from Gaia DR2," *A&A*, vol. 619, p. A106, Nov. 2018.

E. W. Rosolowsky, J. E. Pineda, J. B. Foster, M. A. Borkin, J. Kauffmann, P. Caselli, P. C. Myers, and A. A. Goodman, "An Ammonia Spectral Atlas of Dense Cores in Perseus," *ApJS*, vol. 175, no. 2, pp. 509–521, Apr. 2008.

C. J. Law, K. I. Öberg, J. B. Bergner, and D. Graninger, "Carbon chain molecules toward embedded low-mass protostars," *ApJ*, vol. 863, no. 1, p. 88, Aug. 2018.

W. J. Dirienzo, C. Brogan, R. Indebetouw, C. J. Chandler, R. K. Friesen, and K. E. Devine, "Physical conditions of the earliest phases of massive star formation: Single-dish and interferometric observations of ammonia and CCS in infrared dark clouds," *AJ*, vol. 150, no. 5, p. 159, Nov. 2015.

A. Schruba, A. K. Leroy, F. Walter, F. Bigiel, E. Brinks, W. J. G. de Blok, G. Dumas, C. Kramer, E. Rosolowsky, K. Sand strom, K. Schuster, A. Usero, A. Weiss, and H. Wiesemeyer, "A Molecular Star Formation Law in the Atomic-gas-dominated Regime in Nearby Galaxies," *AJ*, vol. 142, no. 2, p. 37, Aug 2011.

S. Diehl and T. S. Statler, "Adaptive binning of X-ray data with weighted Voronoi tessellations," *MNRAS*, vol. 368, no. 2, pp. 497–510, May 2006.

R. E. Kass and A. E. Raftery, "Bayes factors," *J. Am. Stat. Assoc*, vol. 90, no. 430, pp. 773–795, 1995.

M. G. Kendall, "Rank correlation methods," 1948.

S. Choudhury, J. E. Pineda, P. Caselli, A. Ginsburg, S. S. R. Offner, E. Rosolowsky, R. K. Friesen, F. O. Alves, A. Chacón-Tanarro, A. Punanova, E. Redaelli, H. Kirk, P. C. Myers, P. G. Martin, Y. Shirley, M. Chun-Yuan Chen, A. A. Goodman, and J. Di Francesco, "Ubiquitous NH_3 supersonic component in L1688 coherent cores," *A&A*, vol. 640, p. L6, Aug. 2020.

S. Choudhury, J. E. Pineda, P. Caselli, S. S. R. Offner, E. Rosolowsky, R. K. Friesen, E. Redaelli, A. Chacón-Tanarro, Y. Shirley, A. Punanova, and H. Kirk, "Transition from coherent cores to surrounding cloud in L1688," *A&A*, vol. 648, p. A114, Apr. 2021.

J. Keown, J. Di Francesco, E. Rosolowsky, A. Singh, C. Figura, H. Kirk, L. D. Anderson, M. C.-Y. Chen, D. Elia, R. Friesen, A. Ginsburg, A. Marston, S. Pezzuto, E. Schisano, S. Bontemps, P. Caselli, H.-L. Liu, S. Longmore, F. Motte, P. C. Myers, S. S. R. Offner, P. Sanhueza, N. Schneider, I. Stephens, J. Urquhart, and KEYSTONE Collaboration, "KFPA Examinations of Young STellar Object Natal Environments (KEYSTONE): Hierarchical Ammonia Structures in Galactic Giant Molecular Clouds," *ApJ*, vol. 884, no. 1, p. 4, Oct. 2019.

R. Gutermuth, M. Dunham, and S. Offner, "Revisiting the Protostellar Phase Lifetime with SESNA, the Spitzer Extended Solar Neighborhood Archive," 2022, in prep.